Acoustic Metamaterials: Air Permeable Super Sound Attenuators and Acoustic Metalenses

by

Fuxi Zhang

A dissertation submitted to the Graduate Faculty of
Auburn University
in partial fulfillment of the
requirements for the Degree of
Doctor of Philosophy

Auburn, Alabama
August 3, 2019

Keywords: acoustics, metamaterials, metalenses

Approved by

George T. Flowers, Chair, Professor of Mechanical Engineering
Edmon Perkins, Co-Chair, Assistant Professor of Mechanical Engineering
Robert N. Dean, McWane Endowed Professor of Electrical and Computer Engineering
Dan Marghitu, Professor of Mechanical Engineering
John Y. Hung, University Reader, Professor of Electrical and Computer Engineering

Abstract

In recent decades, acoustic metamaterials have become more practical for diverse applications of sound manipulation, rather than academic curiosities and theoretical derivations. This kind of artificial material demonstrates revolutionary functionalities beyond the limitations of natural material properties, such as efficiently attenuating sound without high density and bulky size, transmitting sound in a highly concentrated and magnified manner, etc. Owing to these fantastic merits, acoustic metamaterials exhibit the feasibilities to present solutions that conventional materials do not possess. For instance, a large number of MEMS sensors and actuators are notably susceptible to the resonance caused by high power acoustic noise, but the accumulated heat emitted from those devices causes functional failures and physical damages as well. In this case, conventional packaging materials are inadequate to solve both problems at the same time. As another example, ultra compact structures typically only dissipate or diffuse acoustic energy. In this dissertation, two super sound attenuators and two innovative acoustic metalenses are proposed by taking advantage of 3D printing techniques. These metamaterials were designed as solutions to these two problems, respectively.

For the first sound attenuator, a micro scale open-through dual expansion chamber (ODEC) package employs both acoustic resonance and thermo-acoustic effects to achieve high and continuous attenuations from 2000 to 8200 Hz. Corresponding experiments with 18 configurations of the ODECs and related control group samples (non-ODEC) were conducted to validate the theoretical predictions with respect to transmission loss (TL). The geometric effect of the TL is also investigated with respect to chamber length and radius. The ODECs perform in the manner of low-pass filters, and their corresponding highest transmissions range from 28.87 to 44.51 dB at 8100 Hz.

For the second sound attenuator, an air permeable labyrinth element (LE) acoustic metamaterial exhibits low transmission, low reflection, and high absorption. This is theoretically expected from the complex open through structure at a deep sub-wavelength scale to provide

low sound transmissions under 500 Hz, which is air permeable and insusceptible to circumambient changes. Experimental results and simulations meet the expectations of high absorption, a substantial near unity absorption from 223 to 327 Hz, and experimentally exhibit impedance matching in this broad low-frequency range.

For the first metalens, a flat Fresnel lens was designed and tested. This lens demonstrated outstanding sound beams from 8120 to 8270 Hz, and the longest beam could reach as far as 65 cm at 8219 Hz with 15 cm width of the beam.

For the second metalens, a perforated sinusoidal channel array with sub-wavelength distances was designed and tested. Enhanced directional far-field sound transmission over a large frequency range was realized through using this compact metalens. Numerical simulations and experimental tests demonstrated a pronounced diffraction-limited sound beam from 7390 to 7600 Hz, which reached as far as 57.6 cm at 7551 Hz with a width of 9 cm.

The conceptual and experimental work of these four compact air permeable sound metamaterials demonstrate the outstanding performance of sound absorption and transmissive sound focusing with wide frequency bands, which show the potential abilities for sound manipulations in heavy industry, aerospace, pharmacy, medicine, ocean applications, etc.

Acknowledgments

I would like to express my sincere thanks and deep appreciation to my advisor, Dr. George T. Flowers, and co-advisor, Dr. Edmon Perkins, for their guidance in the completion of my research work. Their wise suggestions, generous supports, and encouragement contributed immensely to my study and lit my path towards the palace of science.

I also would like to thank my committee professors, Dr. Robert N. Dean, Dr. Jeffrey C. Suhling, and Dr. Dan Marghitu for their academic instructions and assistance. Special thanks are given to my friends and lab mates, especially Mr. Zekun Wang, Ms. Qiuyan Jin, and Ms. Rui Ji. Without their constant supports and friendships, this "journey" would have been much more difficult to accomplish.

Finally, I would like to express my gratefulness to my parents, Mr. Zengke Zhang and Mrs. Aixiang Zhang, and my dear wife, Mrs. Wei Xing, whose love, care, and support have been invaluable for the completion of this degree.

Table of Contents

List of Figures

List of Tables

Chapter 1

Introduction and Literature Review

Sound is a type of compression wave that propagates in continuous media and transports pressure, particle velocity, and etc. along its path. Since people have appreciated the charms of natural sound, humanity has never stopped the pace of pursuing the ways to manipulate sound: from generating it to controlling it to analyzing it.

With about one century's efforts of researchers' dedicated efforts, researchers can now manipulate the characteristics of sound for designated performances. Two of the most popular topics are how to achieve maximum sound attenuation and how to concentrate sound in a desired manner. Rather than building up the mass and size of conventional materials to control the propagation of sound, in recent decades a new concept subverts the traditional cognition of material, named metamaterials, which can accomplish the same goal with much less density and a smaller size. As its name suggests, metamaterials are types of artificial super materials or fascinating structures to have properties that exceed known bounds of nature. For acoustic metamaterials (AMs), the basic principle is primarily accomplished through the effective bulk modulus, B_{eff}, and mass density, ρ_{eff}, which are analogues of the permittivity and permeability in the field of electromagnetism. The goal of AMs is to control the effective impedance, Z_{eff}, and refractive index, *N*, or the acoustic velocity, *C*, and phase, θ [1, 2].

In 1968, Veselago theoretically predicted a kind of medium embodying both negative permittivity and permeability for electromagnetic wave propagation. This is the first time that the concept of metamatierials is proposed [3]. Thirty one years later, researchers physically realized the negative permeability and permittivity by artificial structures [4], and a few years later the negative refractive index was achieved experimentally as well [5]. As a kind

of transverse wave, its electric field, magnetic field, and propagation direction of electromagnetic wave are orthogonal with each other. However, there are some other characteristics in common with longitudinal waves, such as wave vector, impedance, phase speed, especially the expressions of their "mass continuity" and "dynamical equilibrium" in isotropic fluid media [6, 7, 8, 9, 10, 11, 12, 13]. A close analogue between electromagnetic and acoustic waves can be easily made, as listed in Table 1.1. Therefore, it is possible as well to tailor the structures that manipulates desirable effective density and modulus of sound waves, and similar approaches from electromagnetic metamaterials can be used to build acoustic metamaterials. With different combinations of acoustic metamaterial parameters, enormous applications can be achieved far beyond imagination, such as super sound attenuators, acoustic lenses, and acoustic cloaks.

Acoustics	Electromagnetism	Analogy
$\partial P/\partial x = -i\omega\rho_x u_x$	$\partial E_z/\partial x = -i\omega\mu_y H_y$	
$\partial P/\partial y = -i\omega\rho_y u_y$	$\partial E_z/\partial y = i\omega\mu_x H_x$	
$\partial u_x/\partial x + \partial u_y/\partial y = -i\omega P/B$	$\partial H_y/\partial x - \partial H_x/\partial y = -i\omega\epsilon_z E_z$	
Acoustic pressure, P	Electric field, E_z	$-E_z \leftrightarrow P$
Particle velocity, u_x u_y	Magnetic field, H_x H_y	$H_y \leftrightarrow -u_x$ $H_x \leftrightarrow u_y$
Dynamic density, ρ_x ρ_y	Permeability, μ_x μ_y	$\rho_x \leftrightarrow \mu_y$ $\rho_y \leftrightarrow \mu_x$
Dynamic bulk modulus, B	Permittivity, ϵ_z	$\epsilon_z \leftrightarrow 1/B$

Table 1.1: Analogy between acoustic and electromagnetic variables

A thin-film based acoustic metamaterial decorated with a rigid mass in the center was proposed for high absorptions for airborne sound. By adjusting the resonance frequencies, the

flapping motion of this airtight structure was designed to dissipate sound energy, and reached almost unity absorption at designated frequencies from 100 to 1000 Hz [14]. The authors discussed the effective density and bulk modulus and found negativity for the design described above [15, 16]. Later, the same team replicated the same approach with three different setups and assembled them together, announcing the unity absorption at multiple frequencies at the same time [17]. Other researchers developed a kind of airtight membrane-sectioned pipe system with near zero refractive index and zero mass density at the structural resonant frequency of the membrane, which exhibited significant sound squeezing inside the pipeline [18]. Besides absorption by structural resonances of solid substances, the acoustic resonance constructed by fluid media is also feasible to counteract sound propagation. Instead of airtight membrane-sectioned pipe system, pipes with a Helmholtz resonator array validated high absorptions due to artificial bulk modulus as well [19]. A type of perforated plate backed with a coiled air chamber is improved from a Helmholtz resonator and achieved near unity absorption at the acoustic resonant frequency [20]. The combination of hollow tubes with perforated holes on the side and split hollow spheres achieved high absorption due to negativity of mass density and modulus, which is also another variant of Helmholtz resonance [21, 65]. To the purpose of sound attenuation for compact applications, such as electronic devices, the size and heat dissipation characteristcs both matter. Researchers have proposed a type of perforated Helmholtz resonator array in micro-size to protect specific compact MEMS devices. With this sound shield, the sound power was tremendously attenuated at the designated single frequency and meanwhile ensured the air ventilation to prevent overheating of the MEMS devices under protection [23, 24, 25, 26, 27].

Modern industry, from daily electronic products to heavy equipment, largely relies on sophisticated and precise devices to ensure their functionalities. Most workbenches are stable and friendly, but some other working conditions are subjected to many environmental factors that can cause problems and malfunctions due to extremely harsh environments. Acoustic noise, as one source of harsh environments, has been studied in various fields and is an important concern for electronic packaging due to its sometime detrimental effects on electronic systems. Delicate micro-machined sensors and actuators, utilizing extremely small sub-structures,

are particularly susceptible to high power acoustic noise induced structural resonances. Dean, Flowers, *et al*. have experimentally shown that, without a proper acoustic shield, unreliable performance of some certain types of MEMS gyroscopes was observed, at sound levels from 120 to 140 dB near their corresponding resonant frequencies [28]. The susceptibility and degraded performance caused by sound are very similar to the one due to mechanical shock and vibrations at the same frequency range [29]. Besides acoustic noise, the accumulated heat generated by the devices themselves is a very common threat to their performance and durability as well. For the concern of the packaging assembly, coefficients of thermal expansion of the die material mismatch the coefficient of the substrate material at different temperatures, which will usually produce more expansion difference at higher temperature [30, 31]. Hence, the internal stresses of the packaging due to thermal variations primarily lead to mechanical failures, especially cracks and disconnections of solder joints that connect the silicon die and the ceramic substrate [32]. A difficult problem, the traditional packaging materials such as epoxy and ceramic cannot efficiently attenuate high power acoustic noise at designated frequencies. But conventional sound proofing materials tend to be bulky in size or heavy in mass to achieve premium performances of absorption or reflection, which are not qualified for heat dissipation or the size/weight requirements of packaging. Therefore, the challenging tasks researchers face are to develop innovative materials that meet requirements for both perfect sound attenuation and good heat dissipation at the same time.

According to the literature above, the mainstream of sound attenuation approaches targets single frequency solutions. “Bulky in size” and “airtight” are the common outline characteristics of those component. A compact, passive acoustic metamaterial for low sound transmission over a broad low-frequency range, which meanwhile is air permeable and insusceptible to circumambient changes, remains a fundamental practical challenge and is still an open research question.

Since the sound wave can be deteriorated or attenuated, it is also possible to be directed or enhanced by manipulating the effective parameters of sound in an opposite way. Cummer and Schurig have theoretically demonstrated the possibility of acoustic cloaking with anisotropic

materials, which can smoothly direct the acoustic waves around an obstacle without reflections [33]. A kind of cylindrical acoustic metamaterial cloak was practically realized for underwater ultrasound in broadband [34]. Transmissive sound focusing is also a popular topic. Based on the Huygens-Fresnel principle and by means of elaborately spaced sub-structures, enhanced sound transmissions in the downstream have been accomplished by in-phase distribution [35, 36, 37, 38, 39, 40, 41, 42]. Near-field point-focusing was also achieved at designated frequencies with limited diffraction. A type of coiling-up channel array adjusted the sound propagating phases in the downstream to mimic the gradient refractive index like optical lenses, which achieved high transmission for a single point at one specific frequency [43]. A planar lens consisting of the circular ring array experimentally realized multipoint focus for under water ultrasound, due to phase variations with respect to geometry variations [44]. The metalens derived from Snell's law, properly arrayed labyrinthine units manifested strong sound focusing and energy confinement [45]. By engineering the phase, metamaterials could also construct effective medium at single frequency that implemented local sound fucosing without dispersion [46]. A point focusing lens based on improved Fabry-Pérot resonances provided extraodinary transmission. With the variation in geometric parameters, the transmission peak was able to be adjusted [47]. The control of phase and amplitude modulation is also feasible by acoustic metamaterials. A horn-like coiling structure enabled the modification of sound radiation to a double hump pattern, and it had a high potential to modify the radiation pattern by featuring the structural spacing [48]. These outstanding lenses above have some properties in common: enhanced sound transmission at a very short distance, point focusing, and working at a specific single frequency. Although not simple, it is necessary to look forward to new creations that can break through those established facts, such as expecting innovative acoustic lenses for long distance beamforming within a broad frequency band.

In this dissertation, the central theme is to propose the designs of acoustic metamaterials for potential applications for airborne sound attenuation and directional sound beams with a wide frequency band. Meanwhile the layouts are expected to be compact, air permeable, and lightweight. The organization of this dissertation contains six chapters. These chapters are organized as follows:

Chapter 1 is the Introduction and Literature Review, which briefly introduces the applications of acoustic metamaterials and motivations of the research work.

Chapter 2 proposes a design of micro-scale open-through dual expansion chamber (ODEC) package by employing planar wave propagation in stationary air and the thermo-acoustic effect to achieve high and continuous attenuation in a wide frequency range. Analytical models are derived based on transmission line theory and coupled with thermo-acoustic boundary conditions. Corresponding experiments with several configurations of the ODECs and related control group samples (without ODEC) are conducted to validate the theoretical predictions with respect to transmission loss (TL). The geometric effect of the TL is also investigated with respect to chamber length and radius. Significant sound pressure drops are observed above 4 kHz, and reach the highest TLs at 8 kHz.

Chapter 3 demonstrates the study of an air permeable labyrinth element (LE) acoustic metamaterial enabling wideband isolation for low-frequency sound. Low transmission, low reflection, and high absorption are expected from the complex open through structure at deep sub-wavelength scale. The one dimensional analogue lumped circuit model is developed to predict the response characteristics, and the thermo-acoustic effect is coupled into the circuit components. Experimental results and simulations meet the expectations of high absorption and low transmission over the testing band, and experimentally exhibit impedance matching in a broad low-frequency range. The near unity absorption is from 223 to 327 Hz, which is a relatively low frequency range.

In Chapter 4, a flat Fresnel acoustic lens is demonstrated with the outstanding directional transmission over a long distance. The consecutive channels are spaced with designated distances to ensure the directional transmission over a wide frequency band. This approach is evaluated with numerical simulations and experimental tests. The experiments, conducted in an anechoic area, produced a noticeable diffraction-limited sound beam. The sound pressure distribution is concentrated along the central axial direction, in a frequency range from 8120 to 8270 Hz. The sound beam can reach as far as 65 cm at 8219 Hz, and the width of the beam is focused within 15 cm. This 3D printed lens with curved internal channels is an attractive candidate for directional sound projection.

Chapter 5 exhibits a kind of sinusoidal sub-channel approach for sound beamforming. This metasurface lens (i.e., metalens) is composed of perforated sinusoidal channels evenly arrayed with sub-wavelength distances. Enhanced directional far-field sound transmission over a large frequency range is realized through using this compact metalens. Numerical simulations and experimental tests demonstrates a pronounced diffraction-limited sound beam from 7390 to 7600 Hz, which reaches as far as 57.6 cm at 7551 Hz with a width of 9 cm. This metalens is a feasible candidate for directional sound projection and sound energy harvesting.

Chapter 6 presents the concluding remakrs. It briefly summarizes the motivation, methods, and results of the ODEC attenuator, the LE attenuator, the acoustic Fresnel lens, and the sinusoidal sub-channel lens. It offers potential applications for each approaches.

Chapter 2

Micro Scale Open-through Dual Expansion Chamber for Sound Attenuation

2.1 Introduction

Harsh environments are a major cause of the malfunction of compact electronic devices. Micro-scale MEMS gyroscopes, utilizing extremely small proof masses, are notably susceptible to the resonance caused by incident high power acoustic noise. Dean, *et al*. showed that MEMS gyroscopes have unreliable performance when the acoustic noise levels approach 120 to 140 dB near the resonant frequency range of the sample devices [28, 29]. The thermal effect is also as a major cause of deterioration in electronic devices [30, 32]. It is quite challenging to design a packaging structure to achieve good acoustic attenuation and good thermal characteristics for the protacted device at the same time [23, 49]. To meet such specifications, an open-through rigid substructure is considered as one possible strategy.

Considerable work has been performed in the specific area of acoustic attenuation. Yunker and Flowers offered one approach by applying micro scale Helmholtz resonator arrays to a silicon-based acoustic metamaterial, which achieved a notch filter with an attenuation of 18 dB at 14.5 kHz [23]. Soobramaney proposed an airtight approach of isolating porous pads with an average 65% acoustic absorption at around 15 kHz over a wide band [49]. Selamet's derivation showed that a single expansion chamber system (in decimeter scale) produced a transmission loss with a repeating dome-dip pattern within a frequency range from 0 to 6 kHz [50, 51, 52] Gerges *et al*, Munjal *et al* , and Kanade obtained similar conclusions to those of Selamet [53, 54, 55].

However, there is considerable need for attenuation over a continousely broad band, instead of periodic dome-dip attenuation patterns, to adequately protect specific MEMS devices for which the resonant frequency may be quite different than that of the nominal design. In addition, the isolation package and inner structure is required to be in very small scale and a through-hole structure for convection is desired. With regard to the small dimensions, Munjal, Antao *et al*, Friend *et al*, and Karlsen *et al* provided studies of the thermoacoustic effect at rigid boundaries (or walls) causing additional transmission losses [11, 56, 57, 58] Inspired by these works, this current study proposes a further extension of a micro scale open-through dual expansion chamber (ODEC) package by employing planar wave propagation in stationary air and the thermo-acoustic effect to achieve high and continuous attenuations in a wide frequency range. Corresponding experiments with several configurations of the ODECs and related control group samples (without ODEC) were conducted to validate the theoretical predictions with respect to transmission loss (TL). The geometric effect of the TL is also investigated with respect to chamber length and radius.

2.2 Theoretical Derivation

The concentric configuration of a single element ODEC for plane wave propagation is illustrated in Figs. 2.1, and 2.2. It consists of three circular tubes with radius, R_t, and length, L_t, and two circular chambers with radius, R_c, and length, L_c.

As illustrated in Fig. 2.1, the areas in orange color represent the solid rigid structures, and the white color area represents the fluid medium, air. The incident plane wave at the entrance of the ODEC element can be described by the acoustic pressure $p_i = A_i + B_i$ and the volume velocity $v_i = 1/Y_x$, $A_i - B_i = u_i \rho_0 S$, where u_i is the particle velocity associated with p_i governed by the wave equation in Eq. 2.1.

$$\frac{\partial^2 p}{\partial x^2} = \frac{1}{c^2} \frac{\partial^2 p}{\partial t^2}. \tag{2.1}$$

The parameters ρ_0 and S represent the density of air at 20 ^{o}C and the cross-section area of tube or chamber. The acoustic pressure and volume velocity of the downstream ($x > 0$) can be expressed as follows:

$$p_x = A_i e^{-jk\tilde{L}_t} + B_i e^{-jk\tilde{L}_t} = (A_i + B_i)\cos k\tilde{L}_t - j(A_i - B_i)\sin k\tilde{L} = p_i \cos k\tilde{L}_t - jY_x v_i \sin k\tilde{L} \tag{2.2}$$

$$v_x = \frac{A_i e^{-jk\tilde{L}_t} - B_i e^{-jk\tilde{L}_t}}{Y_x} = \frac{(A_i - B_i)}{Y_x \cos k\tilde{L}_t} - \frac{j(A_i + B_i)}{Y_x \sin k\tilde{L}} = v_i \cos k\tilde{L}_t - j\frac{p_i}{Y_x}\sin k\tilde{L} \tag{2.3}$$

$$\tilde{L}_t = \Delta L + L_t \tag{2.4}$$

$k = \omega/c$ refers to the wave number with respect to the wavelength λ. Parameter $Y_x = c/S$ represents the characteristic impedance of a cross section of S at the distance x. L_t and $\Delta L = 8R/3\pi$ refer to the tube length and the corresponding length correction shown in Eq. 2.4.

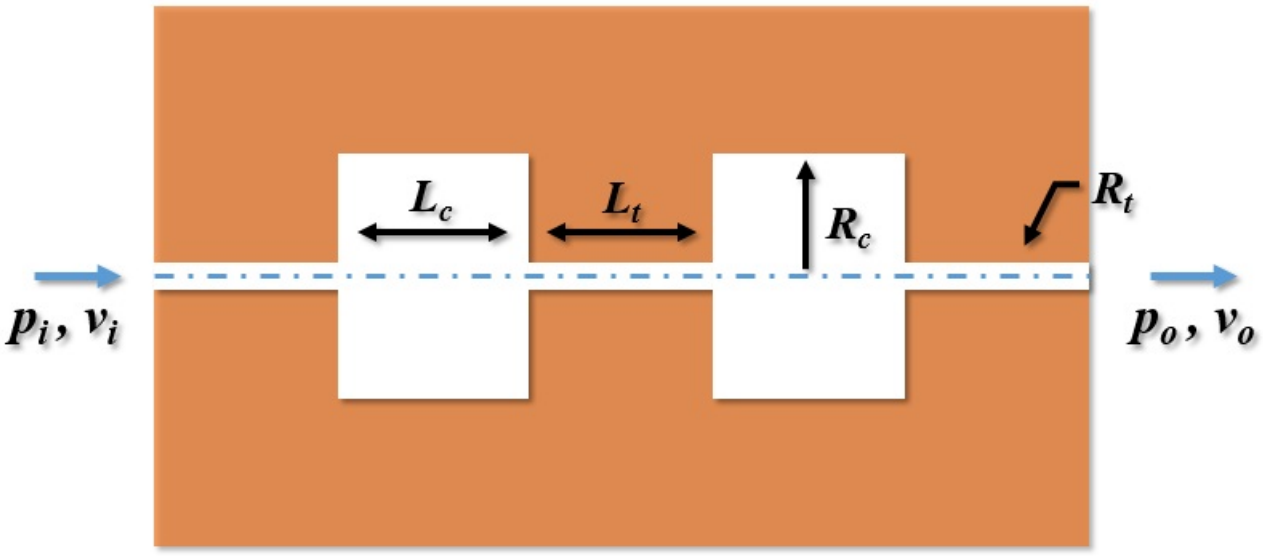

Figure 2.1: Cross section view in 2-D and configuration of the ODEC element. Orange color indicates solid walls.

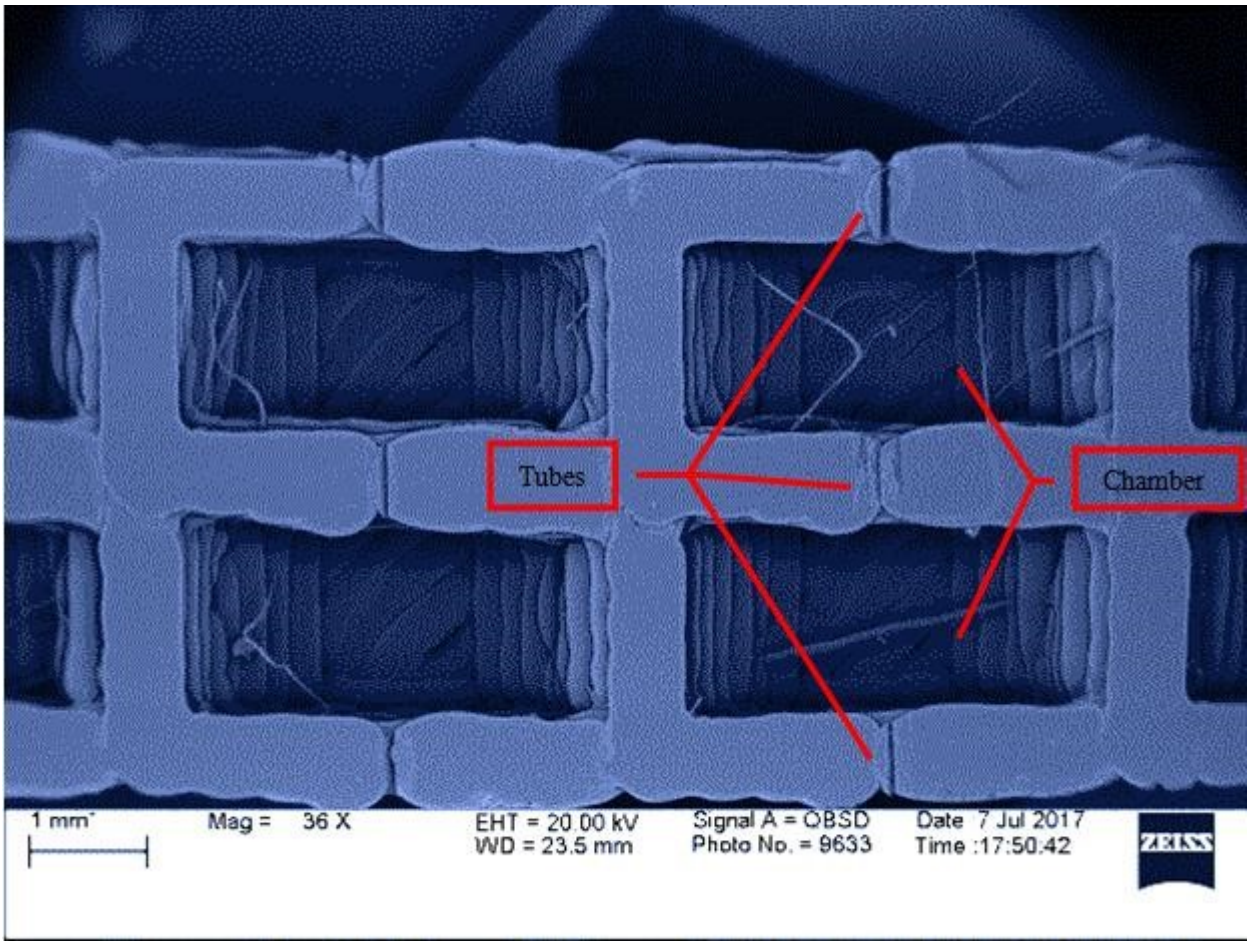

Figure 2.2: Magnified cross section picture of the ODEC array. The ODEC samples are originally in white color. After the SEM scanning, the magnified photos are in grayscale. To felicitate the vision, this picture is rendered to blue color.

By applying Eqs. 2.2 to 2.4, the correlation between the acoustic pressure and volume velocity via the inlet and downstream ($x > 0$) can be expressed in the following transfer matrix equation:

$$\begin{bmatrix} p_i \\ v_i \end{bmatrix} = \begin{bmatrix} \cos k\tilde{L}_t & jY_x \sin k\tilde{L} \\ j/Y_x \sin k\tilde{L} & k\tilde{L}_t \end{bmatrix} \begin{bmatrix} p_x \\ v_x \end{bmatrix} \tag{2.5}$$

By repeating Eq. 2.5 and employing the length of chamber L_c, it can easily get the correlation between the inlet and the outlet as follows:

$$\begin{bmatrix} p_i \\ \\ v_i \end{bmatrix} = \prod_{0}^{x} \begin{bmatrix} \\ M \\ \\ \end{bmatrix} \begin{bmatrix} T_{11} & T_{12} \\ \\ T_{21} & T_{22} \end{bmatrix} \begin{bmatrix} p_o \\ \\ v_o \end{bmatrix} \tag{2.6}$$

where $[M]$ refers to the transfer matrix in Eq. 2.5. The T_{mn} for the specific position along the propagation direction is detailed in **Appendix A**.

Due to the micro-scale of the ODEC structure (under the radial distance threshold: $1.25 \times \delta_v = 1.25 \times \sqrt{\frac{2\mu}{\rho_0 \omega^2}}$, and $\delta + v$ known as the acoustic boundary layer thickness), the particle velocity u_x decreases from the maximum in the center to zero at the rigid wall by the viscous force $f = \mu S(\partial u_x)/\partial r$, and consequently causes additional absorption. Here $\mu = v_k \rho$ is the coefficient of dynamic viscosity of the medium. v_k and ρ represent the kinematic viscosity and ambient density of air, respectively. μ is a function of temperature but independent of frequency. To realize the viscous absorption in the system, the characteristic impedance Y_x can be expressed as a function correlated with μ [59, 60]:

$$Y_x = \frac{p_i}{v_i} = \pm \frac{v_i}{\pi R^2} [1 - \frac{1}{R}(\frac{\mu_e}{2\rho\omega})^{\frac{1}{2}} + \frac{j}{R}(\frac{\mu_e}{2\rho\omega})^{\frac{1}{2}}] \tag{2.7}$$

where R is the radius of each section (such as the tube radii R_t and chamber radii R_c), and the minimum R is set to 45 μm to allow Y_x to be physically meaningful. μ_e is the effective coefficient of viscothermal friction as described in Eq. 2.8.

$$\mu_e = \mu[1 + (\gamma^{\frac{1}{2}} - \frac{1}{\gamma^{\frac{1}{2}}})(\frac{\kappa}{\mu C_p})^{\frac{1}{2}}]^2 \tag{2.8}$$

where $\gamma = C_p/C_v$ is the heat capacity ratio. The parameter κ is the thermal conductivity. C_p is the heat capacity at constant pressure. C_v is the specific heat in a constant volume process. The air properties used in this analysis are listed in Table 2.1.

Table 2.1: The air properties at constant temperature [61].

$T[^oC]$	$\rho[kg/m^3]$	$v_k[\times 10^{-6}m^2/s]$	P_r	$K[W/(mK)]$	$c[m/s]$	γ
20	1.205	15.11	0.713	0.0257	343.28	1.401

Considering the magnitude of the plane wave acoustic pressure at both open ends of the ODEC structure, and assuming there is no reflection at the outlet, which results in $p_o = A_o$ and $p_i = 2A_i - Y_x v_i$. This magnitude can be expressed in terms of elements in the transfer matrix $[T]$:

$$A_i = \frac{p_i + Y_x v_i}{2} = [T_{11}A_o + T12\frac{A_o}{Y_o} + \frac{T_{21}A_o + T22\frac{A_o}{Y_o}}{2}] \tag{2.9}$$

Consequently, the TL can be determined as:

$$TL = 20\log_{10} \mid \frac{A_i}{A_o} \mid = 20\log_{10}[(\frac{Y_o}{Y_x})^{\frac{1}{2}} \mid \frac{1}{2}(T_{11} + \frac{T_{12}}{Y_o} + Y_x T_{21} + \frac{Y_x}{Y_o}T_{22})] \tag{2.10}$$

Reorganizing Eq. 2.10 by substituting Eqs. 2.6, 2.7, and 2.8 into it, the terms T_{mn} become a quintic function of sines multiplying Y_x (real for $m = n$ and imaginary for $m \neq n$). Therefore, the absolute value in Eq. 2.10 increases from 0 in the manner of non-liner curve with increasing frequency ω.

2.3 Experimental Samples and Testing Setup

All samples were designed in the form of a one-side-open box with the same inner dimensions of $1'' \times 1'' \times 1''$. Wall thickness vary from 4.5 to 5 mm with 0.5 mm increment, which is

correlated with the increasing chamber length L_c. The ODEC elements array, of which the tube and chamber configurations were listed in Table 2.2, was fabricated through the walls of each ODEC group sample. The corresponding control samples were comprised of solid walls with the same thickness as the corresponding ODEC group sample. All of the ODEC group and control samples were fabricated with the same material, as illustrated in Figs. 2.3 to 2.5.

A series of experiments were conducted in the Acoustics Laboratory at Auburn University. In order to obtain the sound level measurements, an omnidirectional microphone was firmly encased by a test sample and an isolation case. The incident sound was projected perpendicularly to the side wall of the test samples with a 105 dB SPL level and frequency range from 0 to 8200 Hz. Fig. 2.5 shows a schematic diagram of the experimental setup used in the acoustic testing. Due to the minute structure of the ODEC elements, variations resulting from the sample fabrication process and test setup implementation may yield unexpected outcomes. So, a series of vibration tests were conducted as well to determine each samples' natural frequencies, which was utilized as a reference factor in analyzing the experimental results.

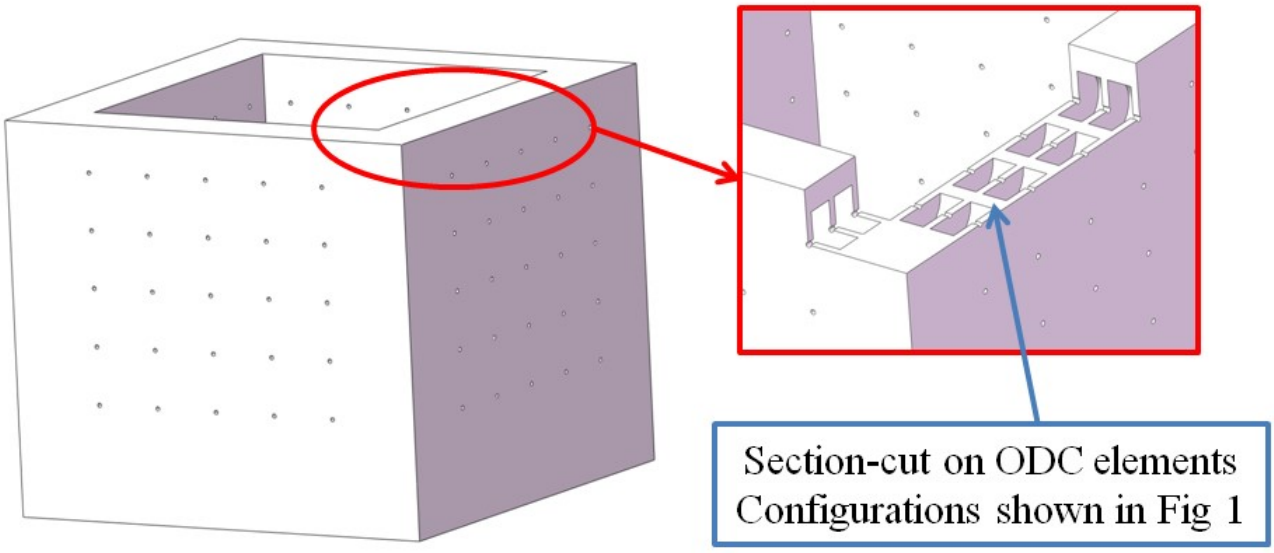

Figure 2.3: 3-D schematic of the metamaterial package design.

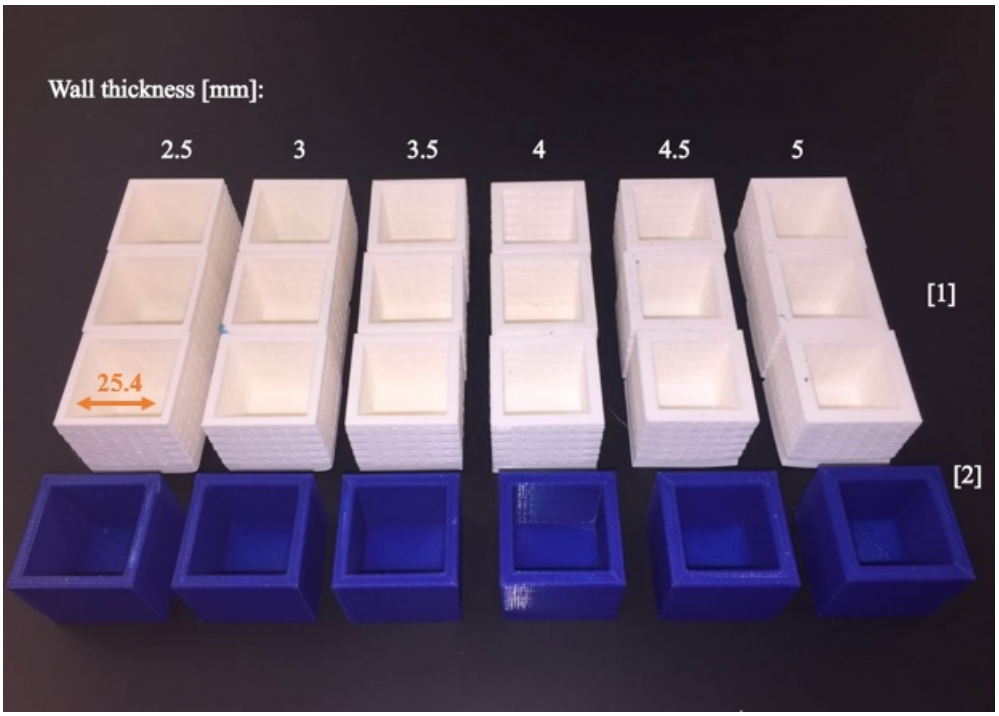

Figure 2.4: Photo of fabricated testing samples. [1]. ODEC samples, [2]. Control samples.

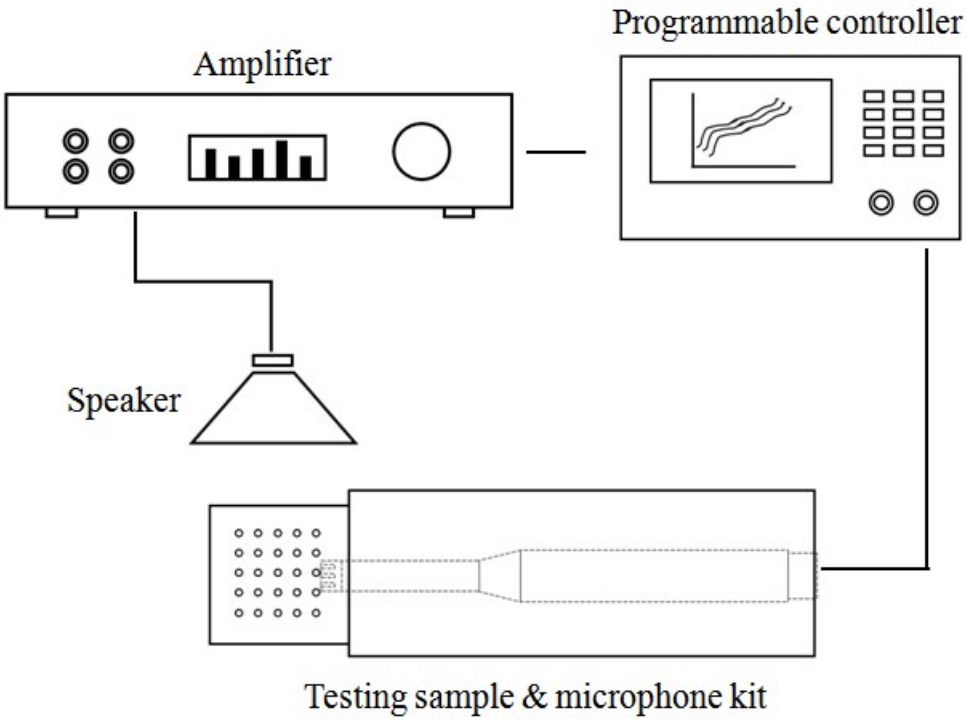

Figure 2.5: Schematic of testing equipment with customized isolation case.

2.4 Results and Discussion

The theoretical model (Eq. 2.10) was used to calculate a variety of transmission loss predictions for Group 1 and 2, illustrated in Figs. 2.6 to 2.11, which were validated by the corresponding

experiments. Figs. 2.12 to 2.17 show the experimental results of the ODEC samples and the control samples.

The predicted TL of sample 1 in Group 1 continuously increases over the frequency range 0 to 8200 Hz with some mild variations. A local maxima of 22.38 dB occurs at 2800 Hz where there is a mildly convex appearance to the curve, and a local minima of 20.25 dB occurs at 4100 Hz where there is a mildly concave appearance. The highest TL value is 45.25 dB at 8200 Hz, which is at highest frequency considered in this analysis. Similarly, convex and concave characteristics can be observed in all the prediction results for Group 1 and 2. The corresponding local maxima, minima, and highest TL values are listed in Table 2.2. As observed, the predicted behaviour of the micro-scale ODEC are in the form of a continuous low pass filter instead of the periodic dome-dip attenuation performance, which differs dramatically from the behaviour observed for chamber systems in large scales [50, 52, 53, 54].

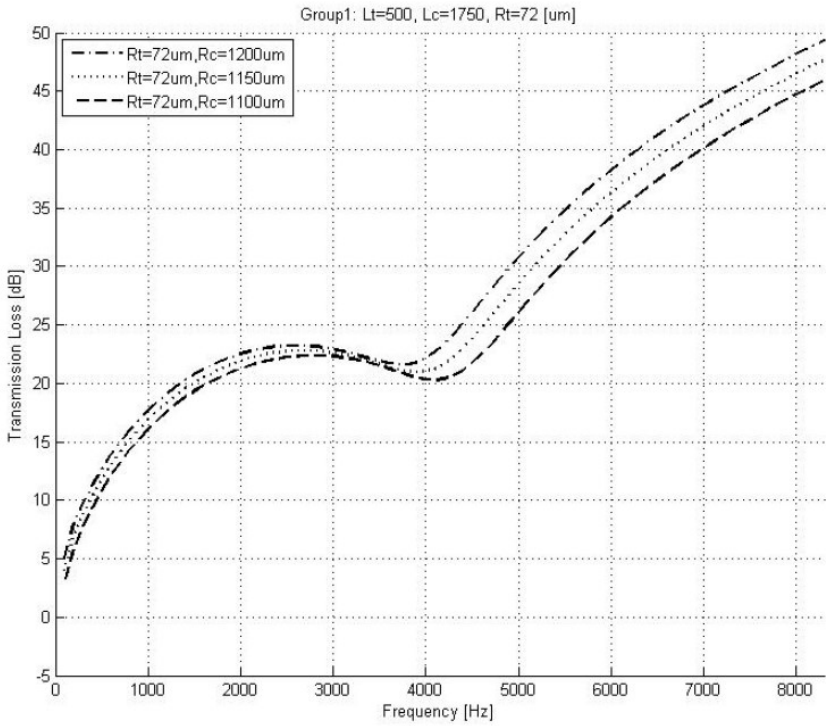

Figure 2.6: Analytical predictions. Group 1, total element length: 5 mm.

Six groups of ODEC boxes were designed, fabricated and tested to validate and compare the analytical predictions. For comparison purposes, three samples in each group share the

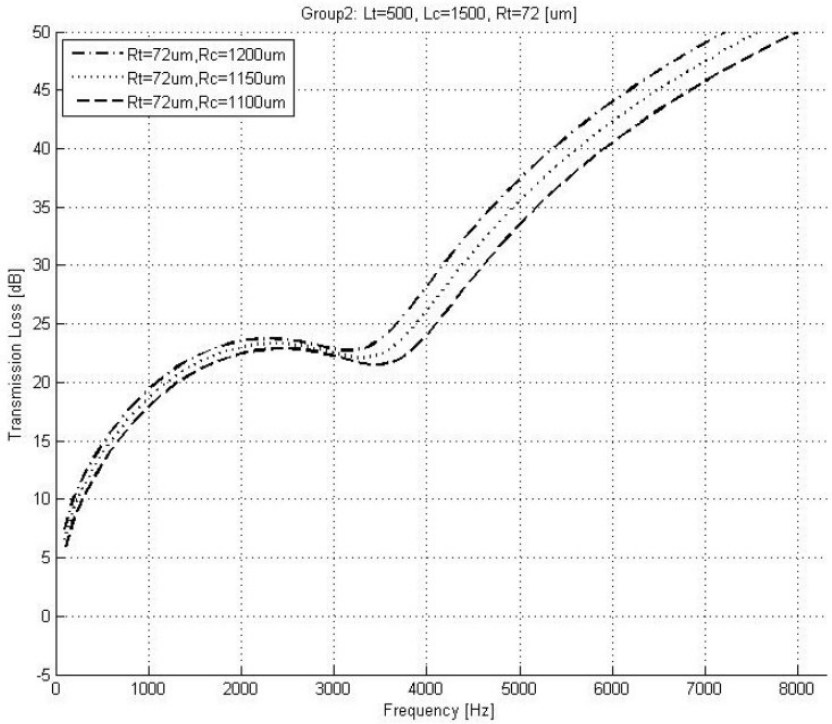

Figure 2.7: Analytical predictions. Group 2, total element length: 4.5 mm.

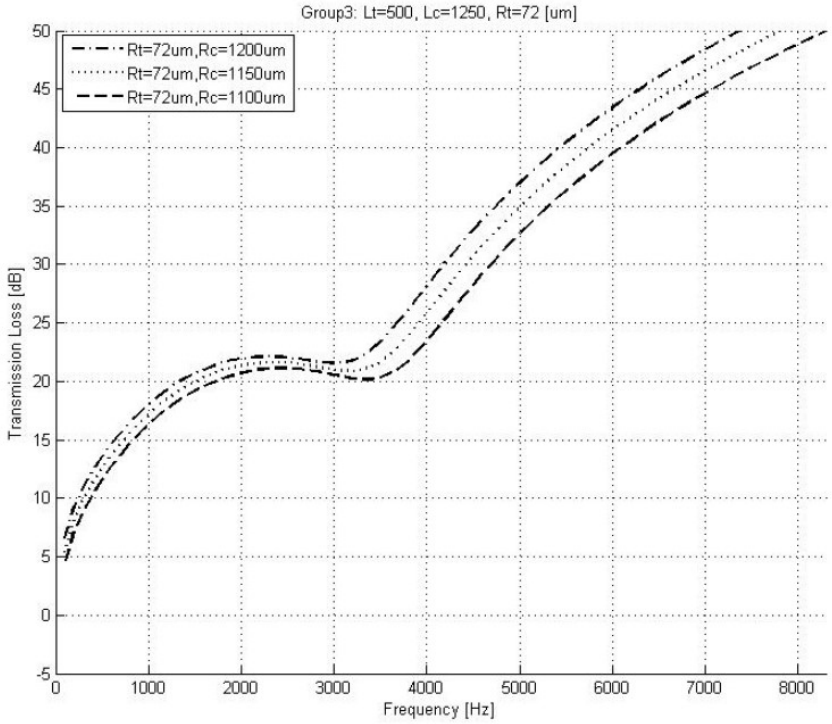

Figure 2.8: Analytical predictions. Group 3, total element length: 4 mm.

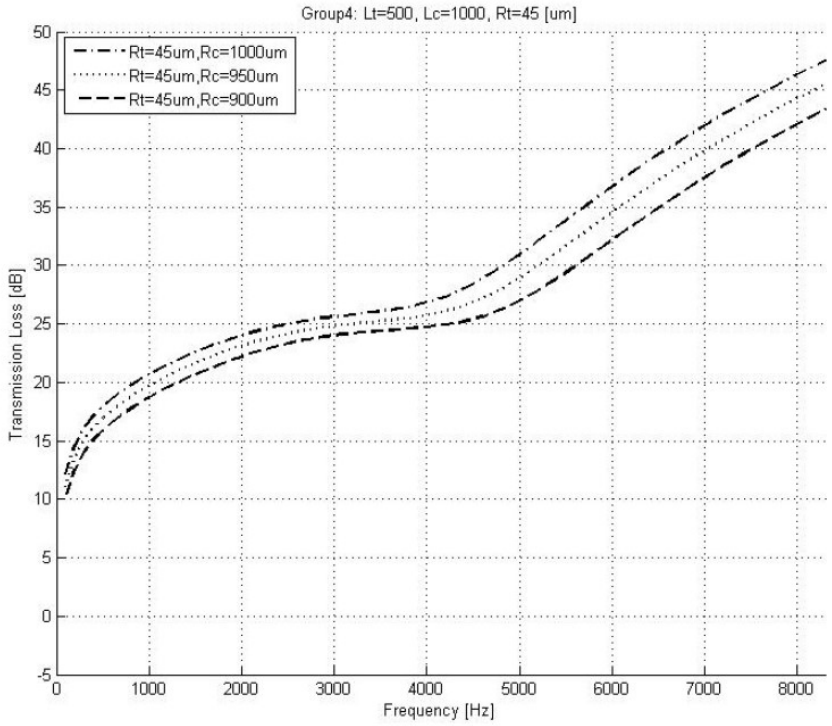

Figure 2.9: Analytical predictions. Group 4, total element length: 3.5 mm.

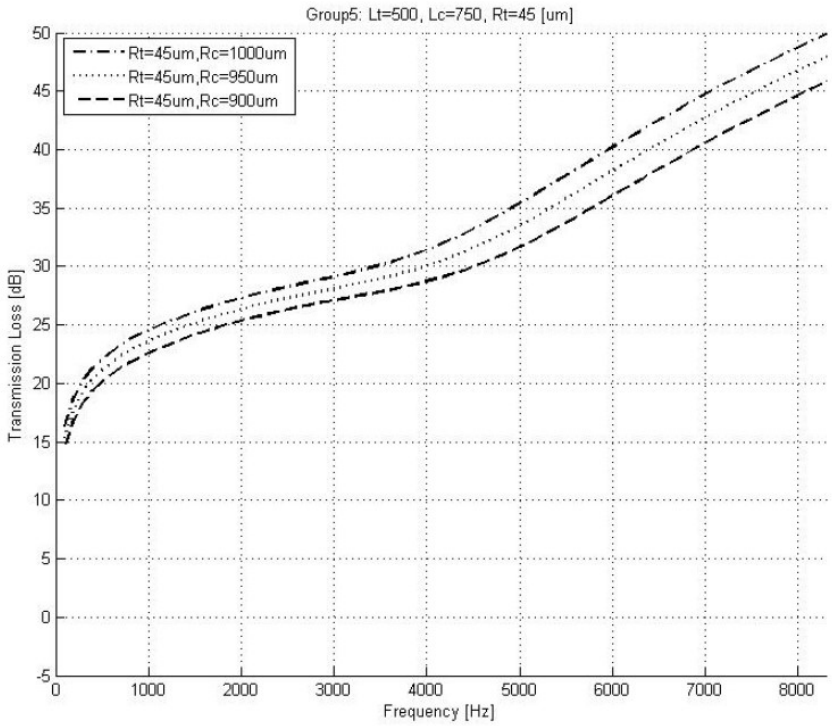

Figure 2.10: Analytical predictions. Group 4, total element length: 3 mm.

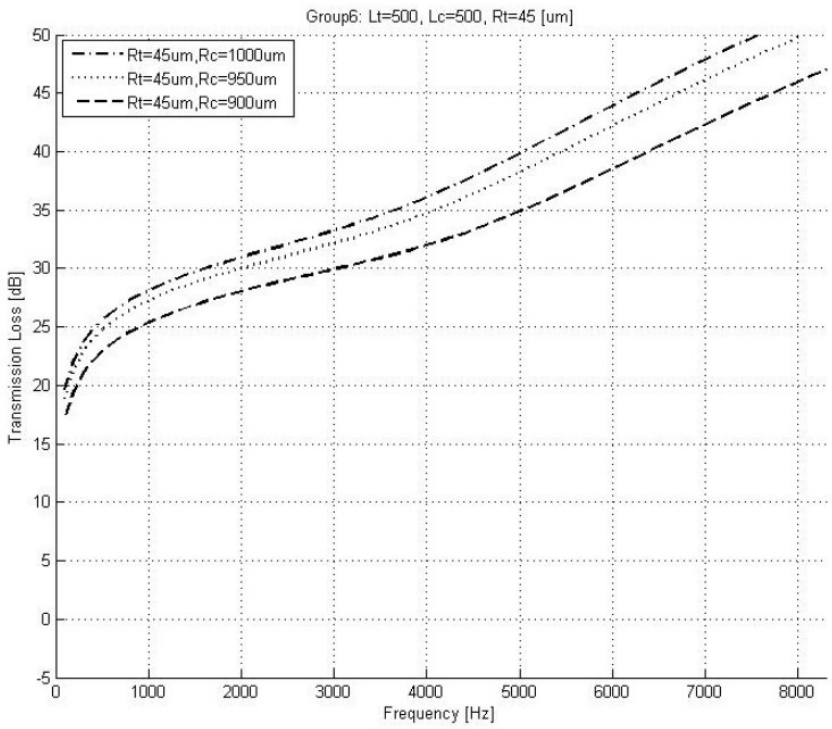

Figure 2.11: Analytical predictions. Group 4, total element length: 2.5 mm.

same total wall thickness but differ in the radii of the expansion chambers. Table 2.2 summarizes the specifics of the detailed geometric configurations and the experimental results of the ODEC metamaterial groups. The lengths of the expansion chambers are reduced by 250 μm for each group, which serves to decrease the total thickness of the walls. The chamber radii are held constant between Groups 1 to 3 and between Groups 4 to 6.

Figs. 2.12 to 2.17 experimentally show the comparison between the measured TL values of the control groups and the ODEC groups. Overall, the experimental results for all ODEC groups correlate well with their corresponding analytical predictions within the same frequency band. The experimental results for the control group samples exhibited somewhat weaker performance than the corresponding analytical predictions. The attenuation performance of the control samples is highly dependent on the material damping characteristics, which are probably not perfectly captured by the linear model assumed in the analysis. This may explain the observed differences. In contrast to the control groups, all six groups of ODEC achieve correspondingly better attenuation performance except in the frequencies below the intersection

area (E). This may be due to the level of precision in the sample fabrication, as well as modeling inaccuracies. In addition, some of the observed differences may be due to the un-modeled dynamics of the test structure. Further experiments were conducted to further evaluate these effects and are discussed in Section 2.4.1

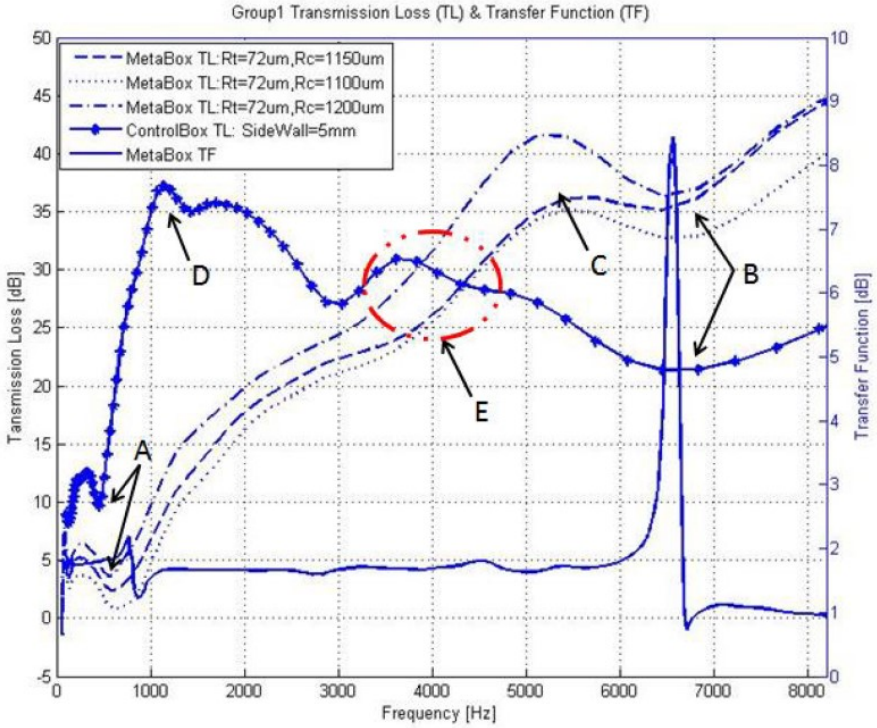

Figure 2.12: Transmission loss from 0 to 8.2 kHz, Group 1.

2.4.1 Comparison of Control Groups to ODEC Metamaterial Groups

In order to facilitate discussion of the experimentally observed behavior in Figs. 2.12 to 2.17, several key sections of the respective curves are denoted by labels, as indicated in the following descriptions. "A" denotes the first concave section of the ODEC and control samples. "B" denotes the second concave section of the ODEC and control samples. "C" denotes the largest peaked convex section of the ODEC samples. "D" denotes the largest peak of the control sample. "E" denotes the intersection region between the control and ODEC curves.

Inspection of the experimental results for the control samples of Group 1 shows a low peak in the starting frequency range (A), from 0 to 0.5 kHz at around 10 to 12 dB. The maximum TL for the Group 1 control samples (D) occurs at 1.2 kHz with an attenuation of 37.61 dB.

Table 2.2: Detailed geometry configuration and testing results of these ODEC groups.

	Sample No.	R_t [μm]	R_c [μm]	L_t [μm]	L_c [μm]	ξ	*Frequency of* 1_{st} *concave* [Hz]	*Frequency of convex* [Hz]	*Frequency of* 2_{nd} *concave* [Hz]	*TLat* 8.1 kHz [dB]
	1		1100			816.94				39.60
Group 1	2	72	1150	500	1750	892.89	640	5315	6451	44.15
	3		1200			972.22				44.51
	1		1100			700.23				36.85
Group 2	2	72	1150	500	1500	765.33	604	5412	6834	35.82
	3		1200			833.34				38.38
	1		1100			583.53				30.87
Group 3	2	72	1150	500	1250	637.78	570	5097	6481	32.09
	3		1200			694.45				33.20

	Sample No.	R_t [μm]	R_c [μm]	L_t [μm]	L_c [μm]	ξ	*Frequency of* 1_{st} *concave* [Hz]	*Frequency of convex* [Hz]	*Frequency of* 2_{nd} *concave* [Hz]	*TLat* 8.1 kHz [dB]
	1		900			800.00				28.87
Group 4	2	45	950	500	1000	891.36	570	4499	6416	32.77
	3		1000			987.66				31.05
	1		900			600.00				29.52
Group 5	2	45	950	500	750	668.52	538	4219	6100	35.27
	3		1000			740.75				32.85
	1		900			400.00				31.32
Group 6	2	45	950	500	500	445.68	508	3816	5424	37.16
	3		1000			493.83				33.98

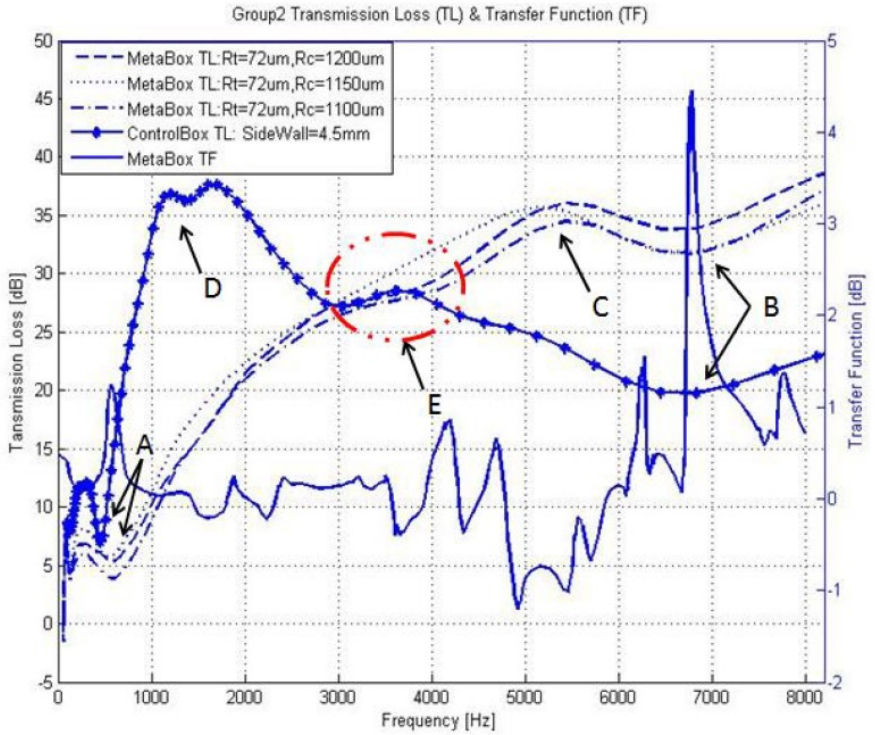

Figure 2.13: Transmission loss from 0 to 8.2 kHz, Group 2.

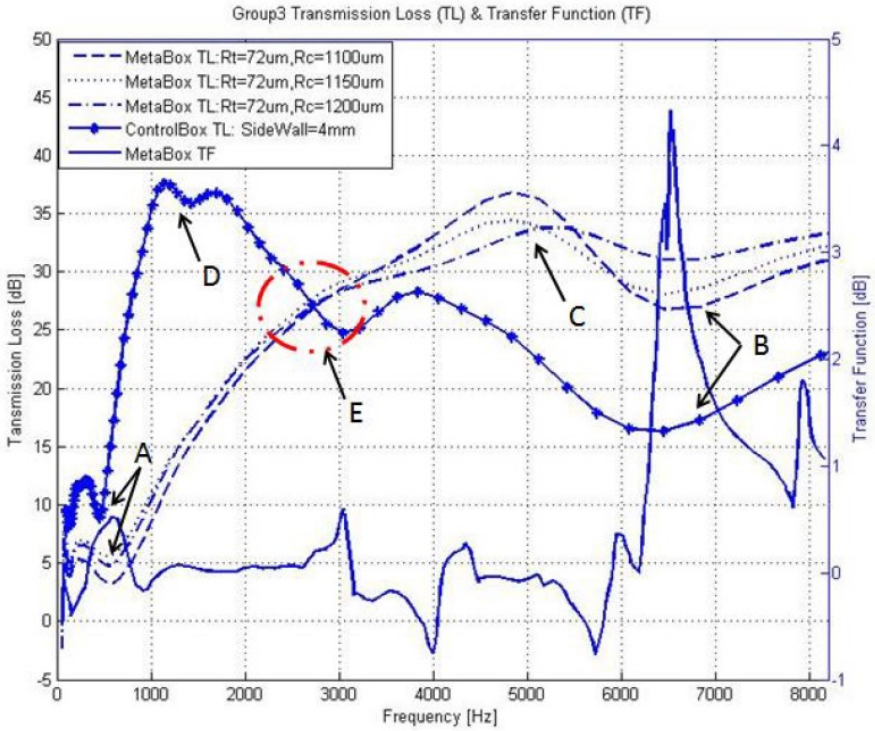

Figure 2.14: Transmission loss from 0 to 8.2 kHz, Group 3.

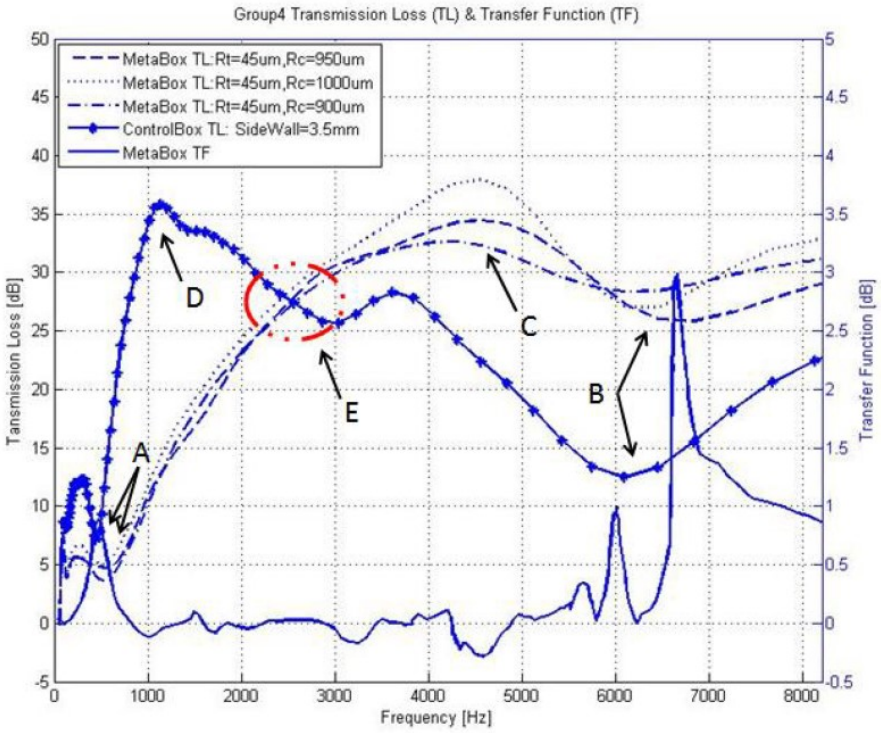

Figure 2.15: Transmission loss from 0 to 8.2 kHz, Group 4.

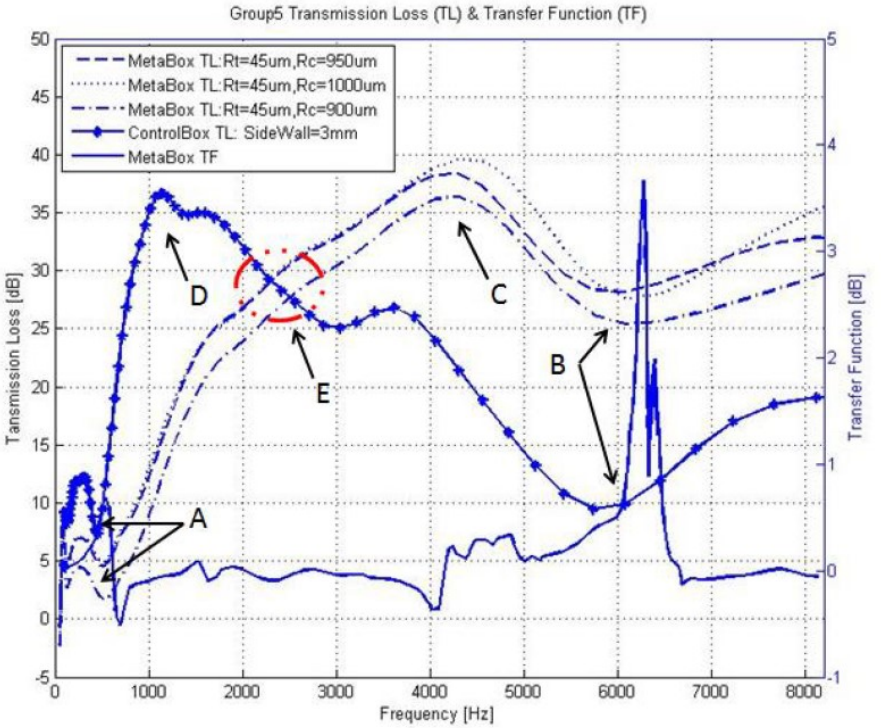

Figure 2.16: Transmission loss from 0 to 8.2 kHz, Group 5.

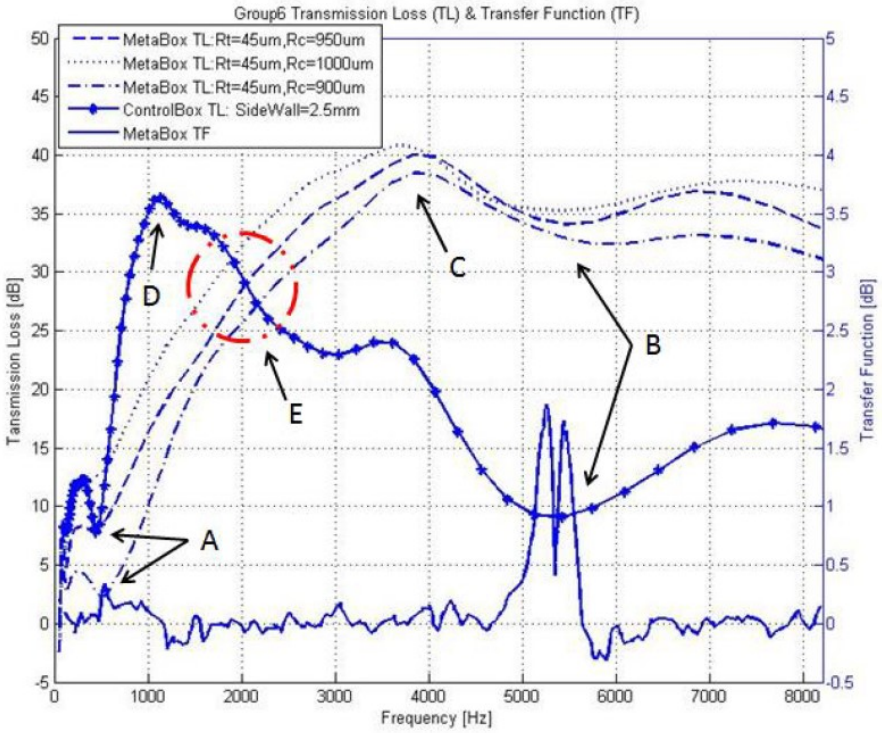

Figure 2.17: Transmission loss from 0 to 8.2 kHz, Group 6.

For frequencies above that associated with the maximum loss, the TL decreases to 21.36 dB at approximately 6.5 kHz before rising to approximately 25 dB at the end of the frequency range. Similar characteristics are observed for all five of the other control group samples, as well. After reaching the maximum attenuation level around 38 dB at about 1 kHz, the TL generally shows a sharply decreasing trend corresponding to the decreasing of wall thickness.

The experimental ODEC results largely agree with the corresponding analytical predictions over the entire frequency band. Unlike the control samples, the ODEC sample results showed similar transmission loss characteristics to those predicted by the model. However, there are several differences between the experimental results and the analytical predictions. The first low peak region (similar to that observed for the control samples but of lower amplitude) has its highest TL at about 8 dB at the center frequency range of 0.5 to 0.6 kHz and has an adjacent concave section (A) with a minimum TL around 0.7 kHz. There is a second concave section (B) which show a minimum attenuation at the center frequency range of 5.4 to 6.8 kHz. Between the two concave regions, there is a peaked convex section (C), which also

shows variation between the model prediction and the experimentally observed results. The measured TL values for frequencies above the concave sections of the curves converged to the corresponding analytical results. All the metamaterial TL values start to be higher than those of the corresponding control groups at the frequencies of intersection point (E). For Group 1 to 6, the intersection frequencies are 4.31 kHz, 3.62 kHz, 2.71 kHz, 2.42 kHz, 2.28 kHz, and 2.03 kHz, respectively. The intersection frequencies decrease with the decreasing wall thicknesses. Table 2.2 and Figs. 2.12 to 2.17 summarize the results of these experiments. The results show that ODEC boxes have significantly higher transmission losses in these higher frequency ranges rather than the corresponding control boxes. The TL differences between the ODEC and control boxes range from about 10 to 20 dB at 8.1 kHz. For the overall performance, Group 1 shows the best transmission loss over the testing frequency.

2.4.2 Effect of Geometric Configuration

Another important design consideration is the effect of wall thickness on transmission loss. Accordingly, the six sample groups were designed with wall thickness starting at 5 mm for Group 1, with a reduction of 0.5 mm in each group down to a wall thickness of to 2.5 mm for Group 6. For the control groups, it can be observed from inspection of Figs. 2.12 to 2.17 that the transmission loss decreases significantly with wall thickness at the frequencies greater than (E) point. As described in the previous section, for the purpose of consistency, the tube length L_t of the ODEC samples was held constant at 500 μm. The length of chambers L_c was set at a starting length of 1.75 mm for Group 1. L_c reduced with every 0.25 mm per group, which resulted in the sample wall thickness starting at 5 mm for Group 1 and ending at 2.5 mm for Group 6.

The volume ratios, ϕ, for each group are tabulated in Table 2.2. The inspection of the analytical and experimental results exhibit that the attenuation performance highly correlates to the volume ratio. For Groups 1 to 3, the TLs decrease in accordance with decreasing ϕ from frequency of point (A) to 8.1 kHz. A similar observation is also true for Groups 4 to 6 as well. Therefore, it appears that volume ratio is a key parameter with regard to transmission loss, with a higher volume ratio generally producing a better attenuation performance.

2.4.3 Vibration of the Metamaterial Structure

As discussed in Sections 2.4.1 and 2.4.2, there are some modest but clearly observable differences between the analytical predictions and the experimental results. These consist mainly of a convex bulge in the TL curves at moderate frequencies and concave sections that precede and follow. It is expected that these effects are related to the resonant characteristics of the gross structure of the sample boxes. In order to test this supposition, a series of vibration experiments were conducted using a vibratory shaker and a non-contacting laser displacement measurement system. The corresponding frequency responses of each group are illustrated in Figs. 2.12 to 2.17, along with the associated transmission loss behaviour.

Inspection of the resulting frequency responses shows that there are two main peaks for each group. The first peaks appear in the frequency range from 0.5 to 0.8 kHz, near point (A), with relatively small amplitudes. The second peaks, with larger amplitudes, appear in the frequency range from 5.3 to 6.8 kHz, near point (B). As shown in Table 2.3, both main resonant frequencies are almost identical to the frequencies associated with the first and second concave sections in each of the ODEC groups. Therefore, it appears that the concave sections of the TL curves (representing decreases in transmission loss) are associated with the first two resonant modes of the sample boxes configuration. Likewise, the convex bulging section (representing increases in transmission loss) are associated with the corresponding anti-resonance points between the two resonant peaks.

Table 2.3: Natural frequencies of all ODEC groups $[kHz]$.

$Natural\ Frequency$	$Group\ 1$	$Group\ 2$	$Group\ 3$	$Group\ 4$	$Group\ 5$	$Group\ 6$
f_1	0.77	0.58	0.61	0.48	0.55	0.54
f_2	6.56	6.78	6.53	6.66	6.27	5.34

2.5 Summary

A type of novel acoustic substructure consisting of a micro-scale open-through dual-expansion chamber (ODEC) element was devised with the objective of noise attenuation. By using an analytical approach which combined the Helmholtz equation and the thermoacoustic effect, an analytical model for a single element of the acoustic substructure was developed. Six groups of the ODEC and corresponding control groups were designed and fabricated. A series of experiments were conducted under the condition of a 105 dB noise incidence source in a swept sine wave from 0 to 8.2 kHz. The ODEC samples from all groups correlated well with the overall transmission loss behaviour observed from the corresponding analytical models. The ODEC groups were designed to provide improved noise attenuation in the upper-frequency range, as experimentally compared to the non-ODEC control boxes. The ratio of the chamber volume to the tube volume was observed to have a strong influence on attenuation. Higher volume ratios, ϕ, induced higher transmission loss.

Chapter 3

Compact Labyrinth Element Acoustic Metamaterials for Broadband Low-frequency Attenuation

3.1 Introduction

Acoustic noise has been studied in various fields and is an important concern for electronic packaging due to its sometime detrimental effects on electronic systems. Conventional acoustic materials tend to be bulky in size and/or heavy in mass. The challenges researchers face is to develop innovative materials that are physically compact and provide wideband attenuation. Hence, new approaches to noise suppression are of great value for a variety of mechanical and structural needs.

Other essential design requirements also need to be considered, such as attenuation characteristics and structural features. In many electronic applications, the heat from components increases the temperature inside packaging and leads to variations in air pressure inside and outside the package. This variation can lead to deterioration of the various components by overheating, while also disrupting the attenuation characteristics of the shield, such as the stop-band shifting and sound leakage as a result of mechanical failure. For instance, rubber-based or membrane-based metamaterials exhibit low transmission at resonance, and their eigenfrequencies are highly correlated with the tensile force on the membrane [14, 15, 17, 18, 62, 63]. The ambient air pressure variation induced by thermal expansion leads to out-of-plane deformation and may result in bandgap shifting or structural failure due to significant increases of tensile force. Nevertheless, some high-performance negative properties metamaterials in moderate size withstand ambient pressure variation for relative high-frequencies applications, such as a perforated plate backed with coiled chamber [20], composite stubs plate [64], Helmholtz

resonator [19, 21], hollow tube with side holes [21, 65] , damped oscillator [66], and the super reflector by using Mie resonances [67]. With the aids of sophisticated designs and sizeable peripheral equipment, active approaches are competent for designated frequencies [68, 69, 70, 71, 72].

Inspired by the ideas above, a compact, passive acoustic metamaterial for low sound transmission over a broad low-frequency range, which is air permeable and insusceptible to circumambient changes, remains a fundamental practical challenge and is still an open research question. In the current study, an air permeable labyrinth element (LE) acoustic metamaterial enabling wideband isolation for low-frequency sound is presented. Low transmission, low reflection, and high absorption are expected from the complex open through structure at deep sub-wavelength scale. Experimental results and simulations meet the expectations of high absorption and low transmission over the testing band, and experimentally exhibit impedance match in a broad low-frequency range.

3.2 Labyrinth Element and Metamaterial Structure

The metamaterial structure consists of a male component (Part A), a female component (Part B), and a rigid seal ring connection, which is illustrated in Fig. 3.1a. Both parts are composed of chambers with connected tubes. The tubes are designed with a diameter $\Phi_T = 1$ mm, length $L_T = 2$ mm, and periodicity $H = 11.3$ mm. The chambers are configured with diameters $\Phi_{C1} = 4$ mm and $\Phi_{C2} = 6$ mm for Part A and B, respectively, and length $L_C = 4$ mm and thickness of the wall $W = 1$ mm. The male chamber is cascaded concentrically with a corresponding upper tube, and the female chamber is geometrically centered between lower tubes. Two capillary air slits connect the chambers of Part A and cavity adjacent to the chambers Part B, as shown in Fig. 3.1b. $T_b = 1$ mm indicates the width of the air bushing. By capping Part A onto Part B carefully, the thickness of the slits H_s is controlled around 0.03 mm. When the openings connect to the atmosphere, the LE allows circulation and preserves the same air pressure on both sides of the material as illustrated in Fig. 3.1c. The sample was fabricated using 3-D printed thermoplastic with chopped carbon fiber. Photographs of a typical sample are shown in Fig. 3.2a and 3.2b.

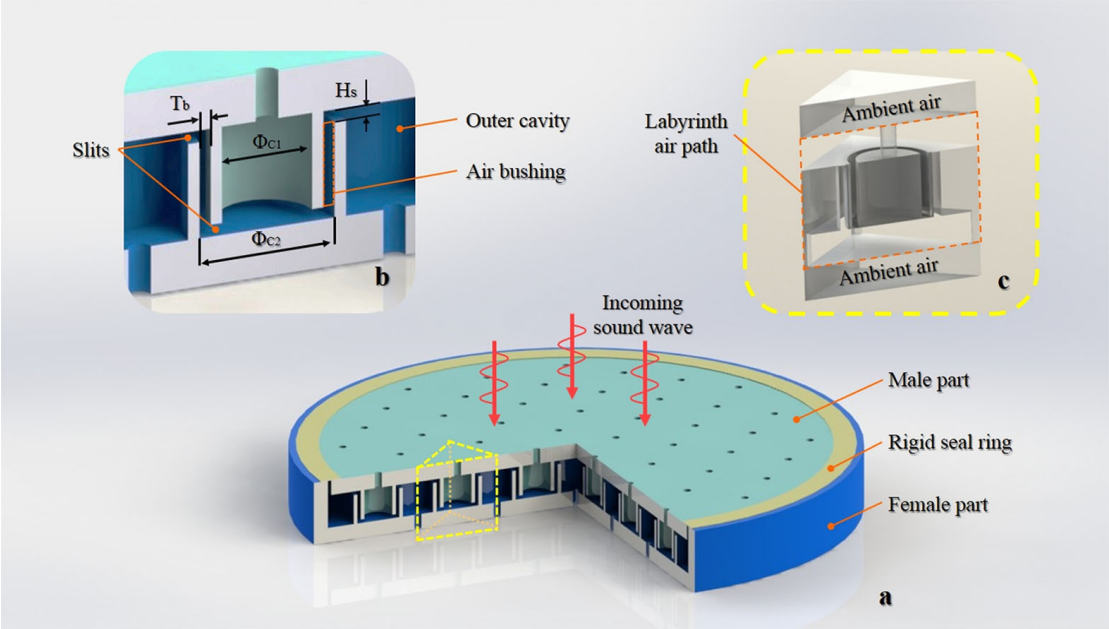

Figure 3.1: The structural configuration of the LE metamaterial. (a) The 1/4 cut-off section view of the LE shield. (b) The magnified cross-section of one single LE unit. (c) The air across the LE unit and the corresponding ambient air on both sides of the LE shield.

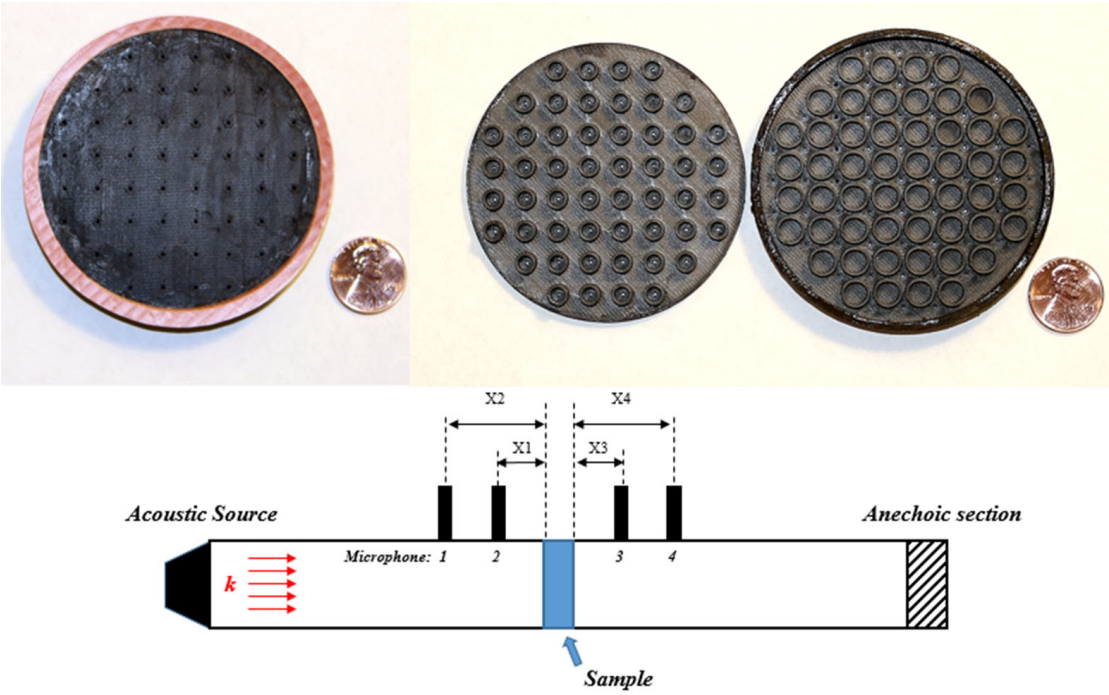

Figure 3.2: (a) Assembled testing sample. (b) Opened view of one sample. (c) Experimental setup of the acoustic impedance tube, where k denotes the incident wave vector.

The geometry of the LEs is much smaller than the acoustic wavelength ($\lambda = 680.58$ mm, at 500 Hz), hence the air filled LE units can be regarded as a homogenized medium. For the cylindrical sections at such small scales, thermoviscous effects at the walls play a significant role in acoustic dissipation effects. The thicknesses of the viscous and thermal boundary layer $\delta_\upsilon = \sqrt{\frac{\upsilon}{\pi f}}$ and $\delta_t = \sqrt{\frac{\kappa}{\pi f \rho C_p}}$ are the thresholds of applying the thermoviscous boundary layers, where υ is the kinematic viscosity of air, f is the frequency, κ is the thermal conductivity, C_p is the specific heat at constant pressure, and ρ is the density of air [73, 74, 75]. The thermoviscous layers are expected to the boundaries of the tubes, air bushings, slits sections, and a majority of the chambers and cavities. The sound attenuation is attributed primarily to the combination of intrinsic air impedance, thermoviscous losses at the walls, and acoustical resonances due to complex geometry factors. The response of a complex LE waveguide is difficult to model precisely because of reflections, air-structure interactions, and other considerations. Therefore, Therefore, the 2-D simulation of a cross-sectional model (Fig. 3.3) was in use of predicting the acoustic response. The experiments were conducted in which the LE sample was exposed to an acoustical plane wave by means of the impedance tube method, which is shown in Fig. 3.2c. The frequency response of the LE samples is shown in Fig. 3.5, with the results of the calculated absorption ($\alpha = 1 - R^2 - T^2$), reflections, and transmission [14].

3.2.1 Theoretical Modeling Approach

To gain insight into the mechanism of the metamaterial design under investigation, an equivalent circuit has been developed that models the ideal thermoviscous effects at the walls as functions of υ and f across a section of the LE unit are developed [73, 74, 75]. The impedance can be expressed in the form of $Z_i = R_i + jX_i$, where the resistance, inductance, and capacitance, and $\Xi_{v,t}e^{j\theta}$ are given by, respectively,

$$R_i = \frac{8\rho f}{\pi(\Phi_i - \Phi_i)^2} \frac{\Xi_v sin(\theta)}{(1 - \Xi_v cos(\theta))^2 + (\Xi_v sin(\theta))^2}, \tag{3.1}$$

$$\omega L_i = \frac{8\rho f}{\pi(\Phi_i - \Phi_i)^2} \frac{1 - \Xi_v cos(\theta)}{(1 - \Xi_v cos(\theta))^2 + (\Xi_v sin(\theta))^2} \tag{3.2}$$

$$\omega C_i = \frac{\pi f(\Phi_i - \Phi_i)^2}{2\rho c_i^2}(1 + (\gamma - 1)\Xi_t cos(\theta)) \tag{3.3}$$

$$\Xi_{v,t} e^{j\theta} = \frac{4\delta_(v,t)}{(\Phi_i - \Phi_i)\sqrt{-j}} \cdot \frac{J_1[\frac{\Phi_i - \Phi_i}{2\delta_{v,t}}\sqrt{-j}]}{J_0[\frac{\Phi_i - \Phi_i}{2\delta_{v,t}}\sqrt{-j}]} \tag{3.4}$$

where $\gamma = C_p/C_v$ is the effective coefficient of viscothermal friction, C_v is the specific heat in a constant volume, c_i is the phase velocity of corresponding sections, θ is the phase, and J_n is the nth order Bessel function of first kind. Φ_i denotes the inner radius of a ring, and for the cylindrical structures $\Phi_i = 0$. The impedance network of a single LE element in 1-D is composed of a combination of the sections described above, as the equivalent circuit represented in Fig. 3.4 and represented by Eq. 3.5 [75, 76, 77, 78]. The corresponding FEA simulation results of multiple elements demonstrate the acoustic pressure across the LE shield. It is important to note that the energy dissipation associated with the narrower diameter regions are more pronounced than that of larger diameter regions, in the limited length of propagation. The large pressure drops at the slits result from the dominance of thermoviscous effects in small geometries.

$$Z_{LE} = R_1 + j\omega L_1 + \cfrac{1}{j\omega C_1 + \cfrac{1}{R_2 + j\omega L_2 + \cfrac{1}{j\omega C_2 + \cfrac{1}{R_3 + j\omega L_3 + \cfrac{1}{j\omega C_3 + \cfrac{2}{R_1 + j\omega L_2} + \cfrac{4}{R_1 + j\omega L_1} + \cfrac{4}{R_1 + j\omega L_1}}}}}} \tag{3.5}$$

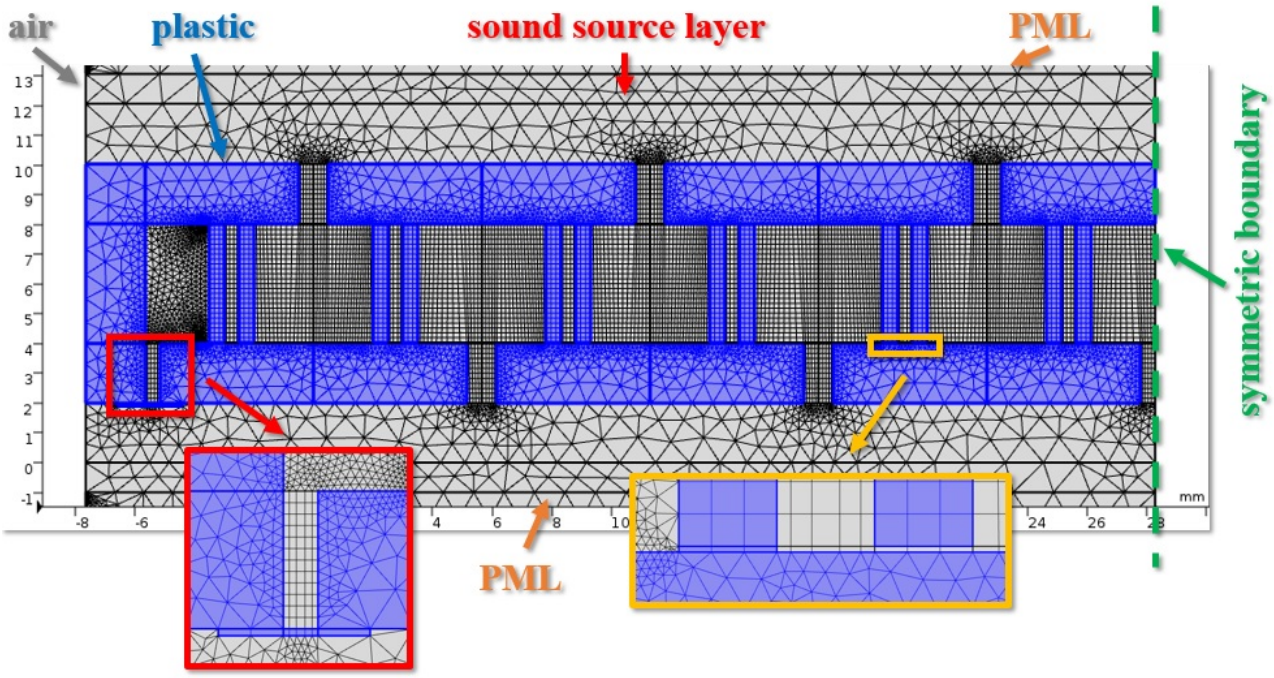

Figure 3.3: Symmetric cross-sectional model in 2-D. The highlighted blue areas refer to solid plastic, and the gray coloured areas are the medium air. A symmetric boundary is set to the right end of the model. The plan wave sound projects downward from the top of the air domain. Perfectly Matched Layers (PMLs) are applied to the top and bottom boundary to mimic anechoic fields.

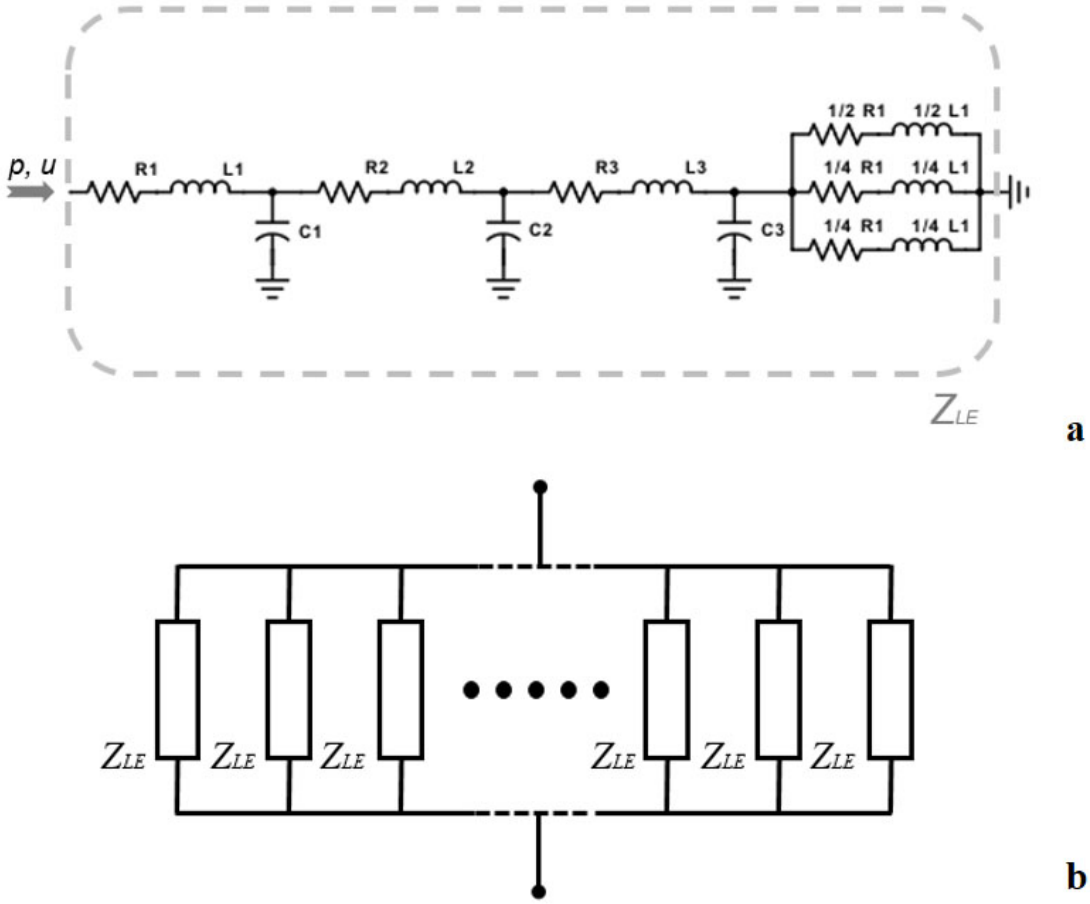

Figure 3.4: Schematic of the equivalent circuit. (a) RLC circuit of one single LE unit in 1-D. (b) Equivalent circuit of LE shield.

3.2.2 High Absorption and Low Transmission

A cross-sectional model (Fig. 3.3) was conducted by the simulation from 150 to 500 Hz with 2 Hz increment. Periodic boundaries were applied to the three cross-sectional surfaces for the purpose of duplicating the simulation domain. The Perfectly Matched Layers (PMLs) were added to both inlet and outlet to mimic the far-field condition in order to avoid unexpected reflections from the limited size of model. Simulation results of reflection, transmission and absorption are exhibited in Fig. 3.5, and selected acoustic pressure and temperature variation (energy dissipation) simulations are exhibited in Figs. 3.7 and 3.8. The reflection keeps about 0.48 from 150 to 200 Hz that indicates a very high reflection region. A deep concave of reflection appears from 250 to 350 Hz, and the reaches the lowest value $R_{Sim} = 0.118$ at 324 Hz. On

the contrary, the absorption achieves from 0.900 at 250 Hz to 0.961 at 350 Hz and the highest absorption is 0.985 at 324 Hz. The transmission in the same region reads from 0.060 to 0.076, which are highly desired for sound suppression. An exiguity of peak of transmission occurs at 386 Hz with the value of 0.138.

The analytical reflection keeps a slight low value around 0.460 up to 200 Hz. A sharp drop from 0.274 at 250 Hz, reaches deepest point 0.062 at 281 Hz, and then increase back to 0.248 at 350 Hz. The corresponding absorption reads as follows: 0.782 at 200 Hz, 0.916 at 250 Hz, and 0.927 at 350 Hz. The highest absorption locates at 277 Hz with the value of 0.987, which has 47 Hz down shifting comparing with maximum simulated absorption. The analytical transmission from 250 to 350 Hz increases from 0.088 to 0.107. A minor peak similar to the simulated transmission can be observed at 391 Hz with the value 0.178, which indicates a high possibility of acoustical anti-resonance due to the sophisticated medium models at corresponding frequencies.

The actual experimental results are more complicated rather than the ideal models above. The experimental results exhibit relatively more fluctuations in Fig. 3.5, over the testing frequency range. From 150 to 200 Hz and 450 to 500 Hz, the reflection remains comparative flat and keeps around the value of 0.431 which anticipated well by simulation results ($0.467 < R_{Sim} < 0.491$). Meanwhile, some concave areas can be seen as well. A bowl-shaped curve drops under 0.3 from 250 to 349 Hz and reaches to the value less than 0.100 from 263 to 346 Hz. At 421 Hz, the reflection dips to 0.047. In the region from 356 to 418 Hz, the reflection fluctuates tremendously with three large peaks: 0.340 at 361 Hz, 0.368 at 389 Hz, and 0.440 at 412 Hz.

Examination of the experimental result in Fig. 3.5, the transmission exhibits the value $0.057 < T_{Exp} < 0.109$ from 250 to 350 Hz, which agrees very well with corresponding simulation ($0.060 < T_{Exp} < 0.076$). However, the simulation did not predict the increased transmissions that occurred at 397 Hz with $T_{Exp} \approx 0.291$. This peak manifests a large discrepancy in both transmission value and frequency from the analytical and simulated predictions. A structural resonance (not acoustical resonance) induced tunneling effect is considered to be

one possibility to cause the bulge and it will be discussed by a vibration validation in the later text.

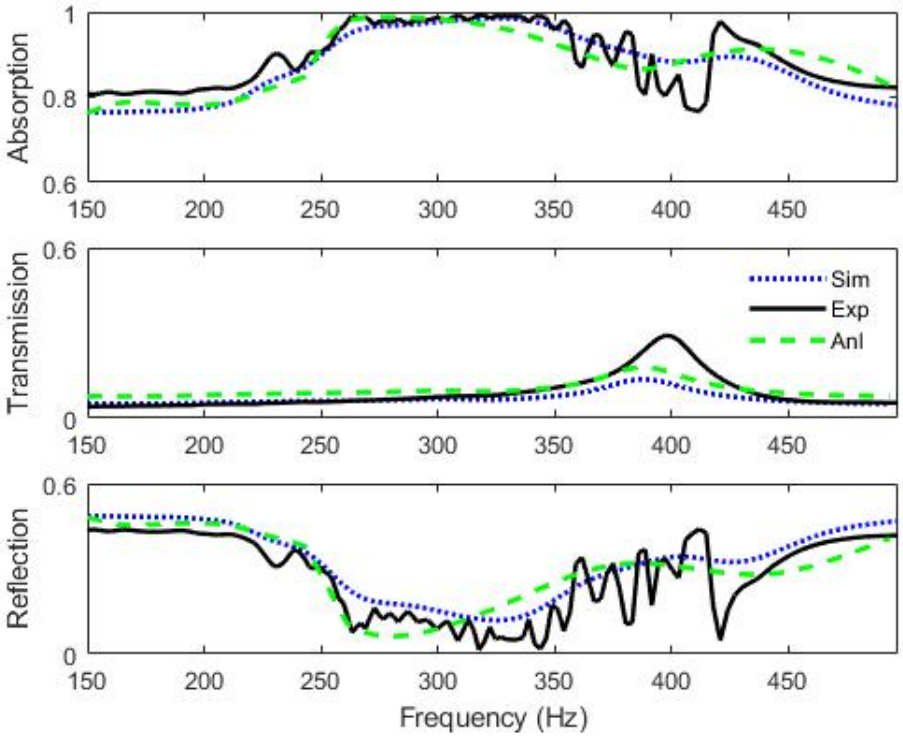

Figure 3.5: Experimental (solid line), Analytical (dashed line) and simulated (dotted line) results of absorption, transmission and reflection, plotted as functions of frequency.

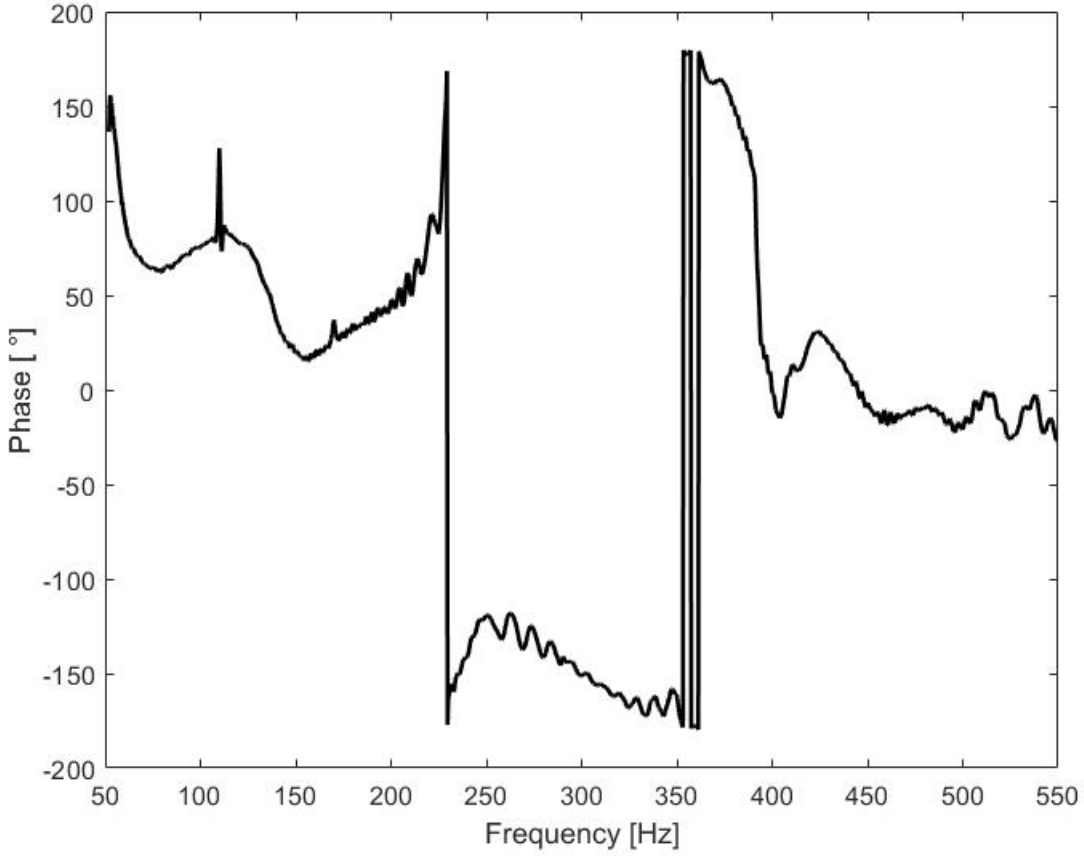

Figure 3.6: Phase of experimental reflection. The scale of measurement is limited from -180^o to 180 ^{o}. A shifted plot will be applied to the data out of limits, such as the phase from 226 Hz to 361 Hz

Relative flat absorption occurs in the range from 150 to 213 Hz with $\alpha_{Exp} \approx 0.823$. A substantial bulging appears in absorption occurs from 223 to 327 Hz with a maximum value 0.994 at 317 Hz, which is near unity ($0.90 < \alpha < 0.99$). The near unity area is coincident with the same frequency range in which the corresponding reflection is concave-up. Referring to the phase of the reflection, the phase angle of the concave-up area reaches around 280^o. Comparing with the responses nearby, there is a 180^o shifting with each other. The out-of-phase reflection and low level of transmission in range from 223 to 327 Hz suggests a broadband acoustical resonance, which results in the unity absorption. In contrast to some other designs with acoustical

resonance at single frequencies, the judicious combination of the intrinsic impedance and thermoviscous impedance is considered as the mechanism principally responsible for acoustical resonance in such wideband [14, 17, 21, 71].

3.2.3 Structural Resonance-Induced Effect

Referring to the absorption trough in the similar band, the representative peak in the transmission coefficient in Fig. 3.5 implies a possible attribution to structural resonance, which could result in high acoustic transmission. Therefore, vibration testing was performed on the LE samples, using an out-of-plane random excitation to identify the structural eigenfrequencies (See Fig. 3.13 for the experimental setup). As observed in Fig. 3.9, the fundamental frequency is located at $f_n = 386$ Hz, which is near the transmission coefficient peak at 397 Hz. Previous studies have shown that, for the evanescent waves, extreme transmissions can be achieved by the tunneling effect when one is stimulated at the vicinity of structural resonance. Consider the tunneling condition in the expression as follows [72, 79]:

$$K\Phi = q\frac{\lambda}{2}, \qquad q = 1, 2, ..., K-1. \tag{3.6}$$

Introducing the resonant wavelength $\lambda = 855$ mm and Φ_{C1} into Eq. 3.6, q is an integer value, which indicates the satisfaction of tunneling. To eliminate this high transmission at specific frequencies, the structural configuration can be modified to shift the resonant frequency.

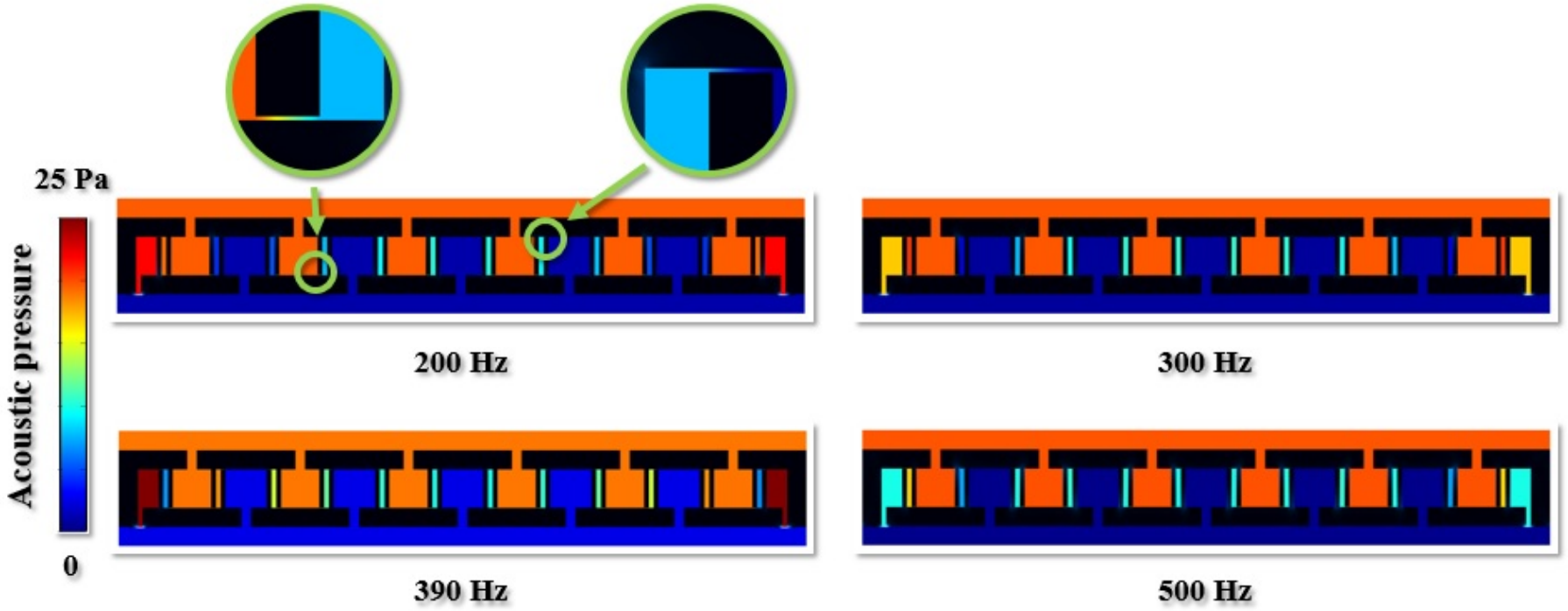

Figure 3.7: FEA frequency responses for a sound sweep from 150 to 500 Hz with 2 Hz increments. The selected results are at 200, 300, 390, and 500 Hz. The acoustic pressure across the LE shield are demonstrated. Notable sound reduction takes place through the slits and the air bushing sections. The slight reduction of sound pressure along with increasing frequency in the cavity and outgoing tubes manifests the minor decrease of the predicted transmission.

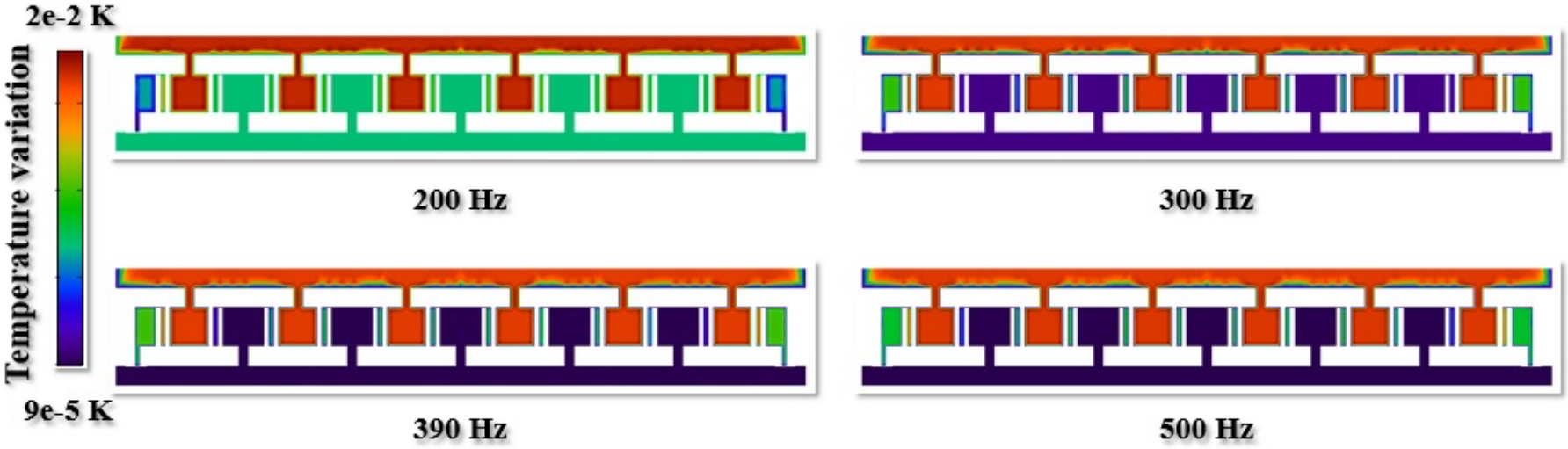

Figure 3.8: Synchronous temperature variations across the LE shield. Clearly, most energy losses occur at slits and bushing sections, as well as at the walls of the incoming tube and chamber

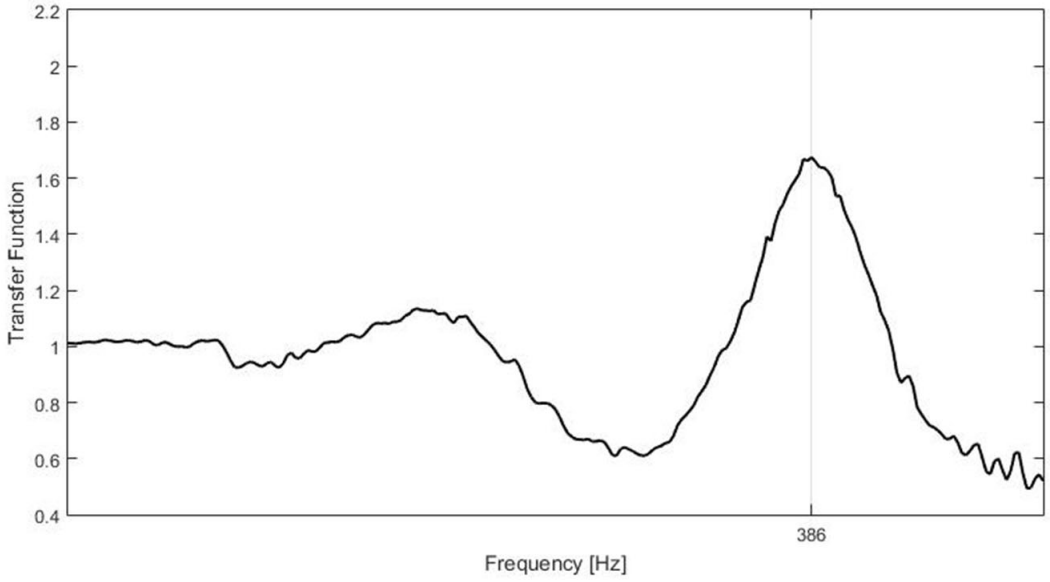

Figure 3.9: Frequency response (Transfer Function) of LE sample conducted from vibration testing. The non-contacting laser vibrometer targeted on the center of the center of the male component.

3.2.4 Realization of effective density and modulus

As discussed in the previous section, the LE metamaterial can be considered as a homogeneous material, because the LE size is much smaller than the wavelength. The effective material properties can be expressed based on an analogy with the electromagnetic theory in a homogeneous medium [21, 80]. The effective density, ρ_{eff}, and modulus, M_{eff}, can be derived from the refractive index, N, and the effective impedance, Z_{eff}, which couple to reflection, R, and transmission, T, as follows:

$$N = \frac{-i \log \Gamma}{kd}, \tag{3.7}$$

$$Z_{eff} = \frac{\Psi}{1 - 2R + R^2 - T^2}, \tag{3.8}$$

$$\rho_{eff} = n Z_{eff} \rho_0, \tag{3.9}$$

$$M_{eff}^{-1} = \frac{N}{Z_{eff}} M_0^{-1}. \tag{3.10}$$

where $\Gamma = ((1 - R^2 + T^2 + \Psi))/2T$, $\Psi = \mp\sqrt{(R^2 - T^2 - 1)^2 - 4T^2}$, k is the wave vector, and d represents the thickness of the LE shield. The Ψ is solved by selecting the root that returns a positive solution of Re(Z_{eff}/Z_0) and Z_0 is the characteristic impedance of air.

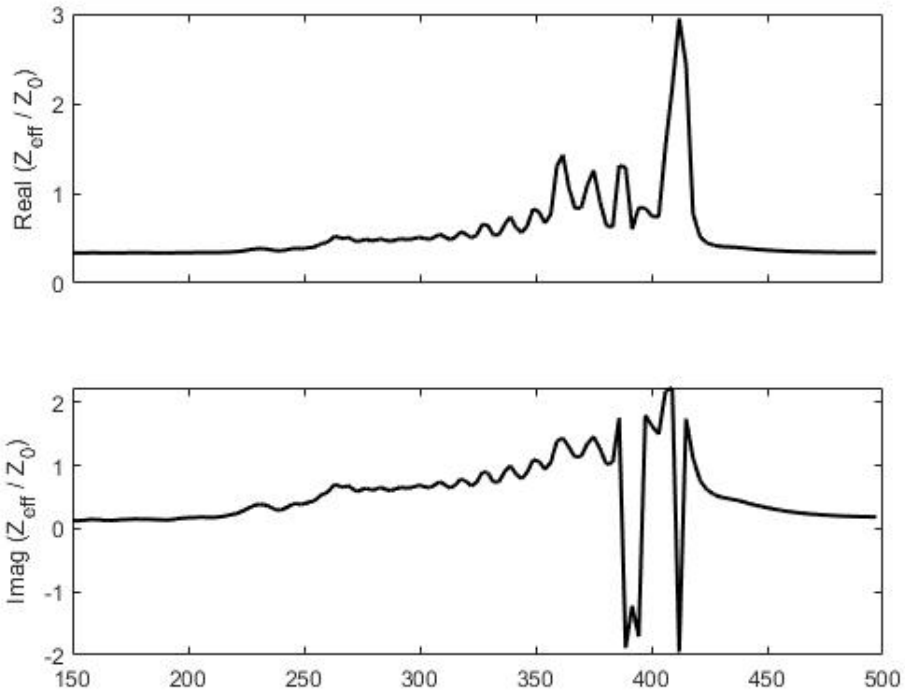

Figure 3.10: Effective impedance Z_{eff}/Z_0 derived from experimental results of LE shield.

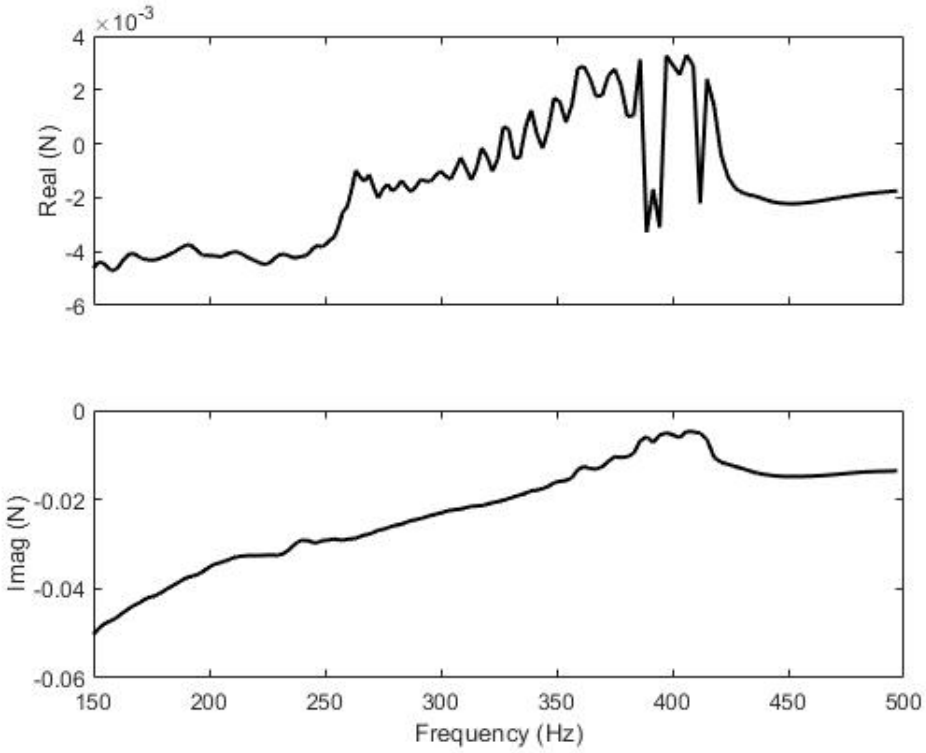

Figure 3.11: Refractive index N derived from experimental results of LE shield.

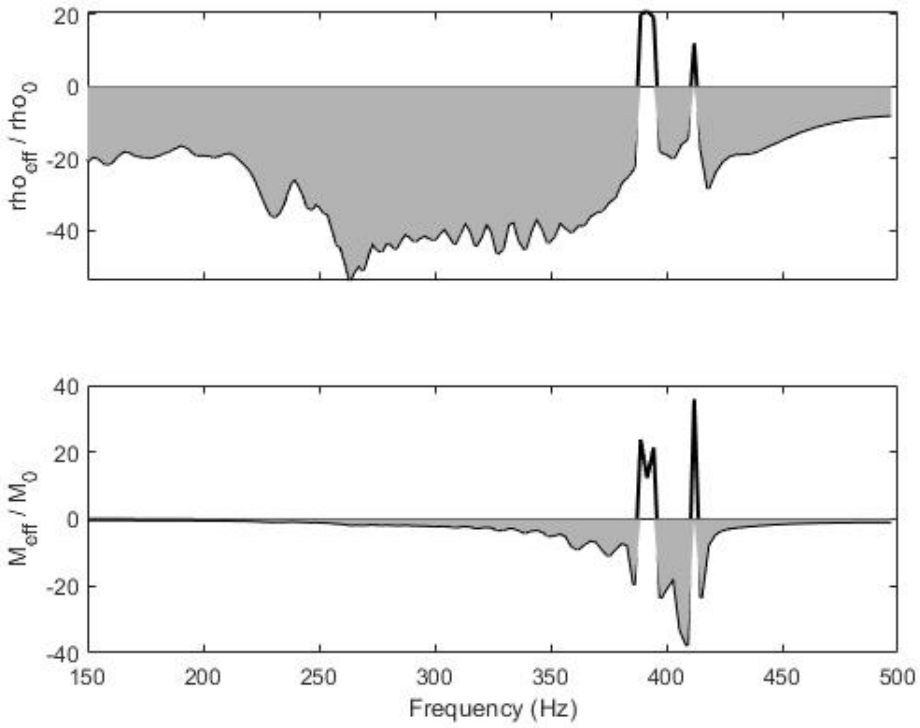

Figure 3.12: Effective density $\rho_{eff}/\rho_0$and effective modulus M_{eff}/M_0 derived from experimental results of LE shield. Negative values of effective density and modulus are shaded for guidance.

Inspecting the impedance responses of the imaginary part, the inductivity dominates most of the frequency range, as illustrated by the Imag(Z_{eff}/Z_0) in Fig. 3.10. Thus, it is concluded that that the overall impedance exhibits a high level of inductance.

As demonstrated in Fig. 3.11, the real component of the calculated refractive index, N, exhibits negativity beside a band adjacent to the structural resonance. Positive values coincide with ω_n. Concurrently, the imaginary component is negative across the whole testing band, and the imaginary magnitude is approximately one order of magnitude larger than the corresponding real magnitudes. This is adequate to result in a net negative value of N, which indicates a strong exponential loss in energy of plane wave propagation [81].

It can easily be observed that negative values of effective density, ρ_{eff}/ρ_0, occupy most of the testing band. A narrow positive band is caused by a strong oscillation of the wave field induced by structural resonance and leads to a Bragg gap on the boundary of the LE shield

[80, 82]. The consequent reflections impair the acoustic energy dissipation originated from the thermoviscous absorption at the inner walls of the LE shield; collectively with the tunneling effect, this can explain the high transmission.

The effective modulus, M_{eff}/M_0, up to 200 Hz is near 0. A trough of negative values covers the rest of the frequency band with the exception of two positive spikes, as depicted in Fig. 3.12. These highly nonlinear spikes coincidently occur near f_n. It has been shown that this considerable perturbation indicates the self-phase modulation, which enhances the resonant transmission to a certain extent [19, 72].

3.3 Experimental Method and Setup

The acoustical properties testing was conducted in a precisely fabricated impedance tube which complies with ASTM E2611-17. An amplifier (LDS PA 500L) and a loudspeaker (Dayton ND65-4) generated the plane wave from one end of the waveguide. The sample was mounted in the center of the waveguide with enough distance from the sound source, in order to ensure the plane wave propagation over the testing frequency band. An anechoic end with absorbing foam was mounted on the other end of the waveguide to eliminate the reflection. Four $1/4$" calibrated condenser microphones (Beyer Dynamic MM-1) were flush mounted at designated positions. The data acquisition unit (NI 9205) is applied to communicate the signals between the computer with the loudspeaker/microphones. The swept-sine signal was produced by a computer covering from 150 to 500 Hz.

The Finite Element Method simulation results were conducted through the software COMSOL Multiphysics. The model is fully conducted with the thermoacoustic study. Two PML layers were applied on both ends of the model to mimic the far-field of ambient air to eliminate the sound reflection from background. The symmetrical boundary was added to the cross-sectional surface.

The vibration results were obtained using a testing system which consists of a LDS V408 shaker, two Polytec OFV-353 laser vibrometers, and an HP 35665A dynamic signal analyzer. A detailed depiction of the experimental setup is shown in Fig. 3.13. A laser reflecting pad was

applied at the center of the testing sample. Another reflecting pad was attached on the rigid 3-D printed fixture which is firmly secured on the shaker head.

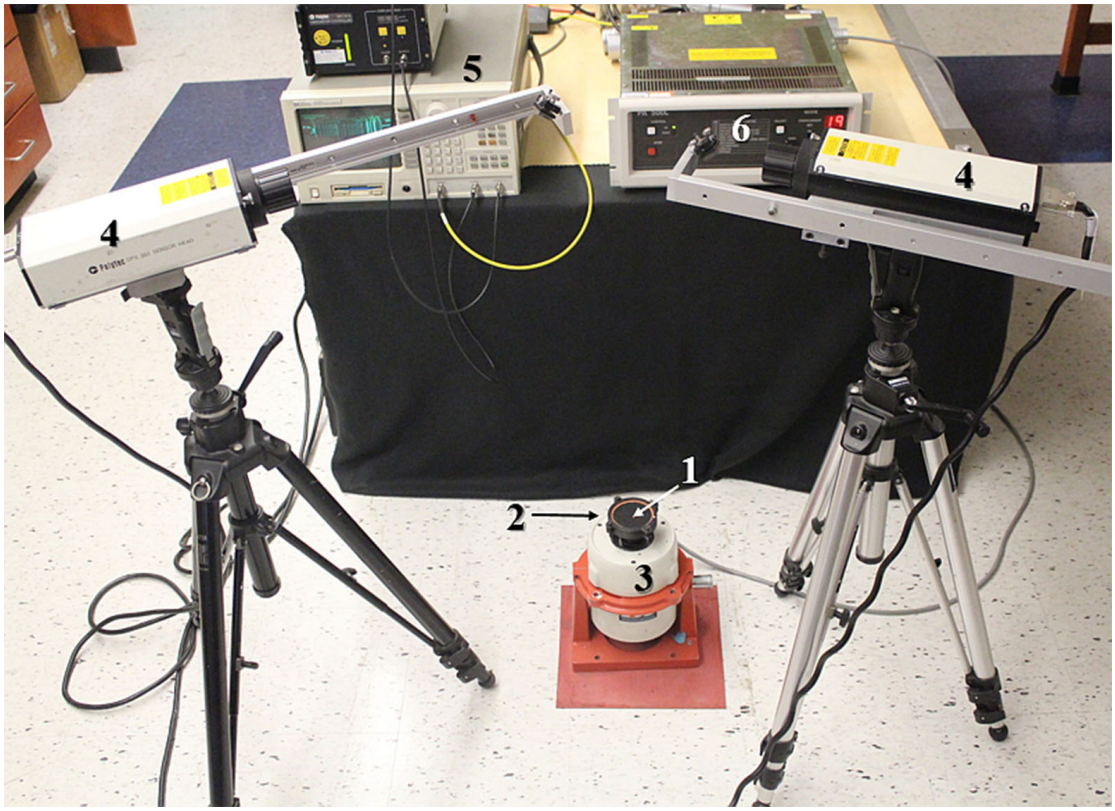

Figure 3.13: The experimental setup exhibiting the vibration testing. The HP analyzer and amplifier generating random noise signal to excite the shaker, and two laser vibrometers measuring the out-off-plane displacement of the sample and fixture.

3.4 Summary

This chapter presents a novel metamaterial design that employs labyrinth elements and is capable of nearly unity sound attenuation from 223 to 327 Hz, with the added benefit of low mass and compact size. Experiments achieved good absorption and low sound transmission. The open path of air in the deep-subwavelength scale essentially contributes to the thermoviscous effect and acoustical resonance due to sophisticated geometry. It provides a means for air permeability to balance the air pressure on both sides of the shield. By utilizing these advantages, this metamaterial may be a useful tool to mitigate acoustic noise for special needs in harsh environments.

Chapter 4

Acoustic Fresnel lenses for directional sound beam projection

4.1 Introduction

A flat Fresnel acoustic lens is demonstrated with the outstanding directional transmission over a long distance. The consecutive channels are spaced with designated distances to ensure the directional transmission over a wide frequency band. This approach was evaluated with numerical simulations and experimental tests. The experiments, conducted in a 90 x 70 cm2 anechoic area, produced a noticeable diffraction-limited sound beam. The sound beam was a concentrated sound pressure pattern along the central axial direction, in a frequency range from 8120 to 8270 Hz. The sound beam can reach as far as 65 cm at 8219 Hz, and the width of the beam is focused within 15 cm. This 3-D printed lens with curved internal channels is an attractive candidate for directional sound projection.

Unlike light, long-distance, directional projection of sound transmission poses great challenges, especially for broadband transduction. To achieve a laser-like sound beam, the proper refractive index of the lens material and tailored manipulation of the impedance mismatching with the host medium are still difficult tasks. Alternative solutions have been proposed in recent decades, such as modulating audible sounds to the ultrasonic range or acoustic metamaterial lenses. The parametric acoustic array (PAA) creates a lower frequency sound beam as a result of combining multiple ultrasonic signals at their difference frequency [83]. By benefiting from this nonlinear phenomenon, the audible sound beam can be actively generated by multiple ultrasonic loudspeakers [97, 85]. Recent advances of acoustic metamaterials (AMs) propose

some novel lens designs, with extraordinary functionality, as alternatives to PAA. AMs are particularly attractive due to their ease of implementation, smaller size, and lower cost.

By manipulating the phase of the propagating sound wave, acoustic metamaterials have been shown to produce some artificial properties not found in nature, such as a negative refractive index and a negative effective density [1, 2, 86]. The acoustic field performance can be controlled by engineered phase interactions with multiple AM units, whose rationale is based on the Huygens-Fresnel principle and Fabry-Perot resonance [67, 87, 88, 89, 90]. Motivated by these phenomena, AM lenses consisting of space-coiling units create the gradient phase of sound that focuses acoustic pressure at the desired position for selected frequencies [43, 47, 48, 91]. The perforated slits with designated width and space result in strong focal performance, due to coupled sub-diffractions and scatterings [92]. More recently, developments of circular perforated ring lenses utilizing the Fresnel Zone can produce adequate transmission efficiency with limited diffraction and generate a sharp focal point at certain frequencies [41, 42, 44, 93, 94, 95, 96]. Inspired by the efforts above, a novel design for an acoustic Fresnel lens is proposed and tested. This lens design exhibits an improved long-distance, directional sound transmission, rather than a single focal point in the near field. Within a wide range of audible frequencies, the transmission is considerably concentrated along the central line, while the sound pressure in the neighboring area is lessened. For this reason, the proposed lens an attractive candidate for a range of applications for which this phenomenon could be useful, including medical, pharmaceutical, and sensor/actuator design.

4.2 Results and Discussion

The lens consists of perforated circular channels, which have straight and U-shaped cross-sections. The geometry of the lens is depicted in Fig. 4.1. The U-shaped channels steer the sound with a longer path than the straight channels for the purpose of tuning the phase. All channels are aperiodically placed in the radial direction in order that the Fabry-Perot resonance can achieve concentrated transmission. Moreover, the diffractive sounds in the downstream are controlled to be in-phase within a limited radius, which relies on the Huygens-Fresnel principle.

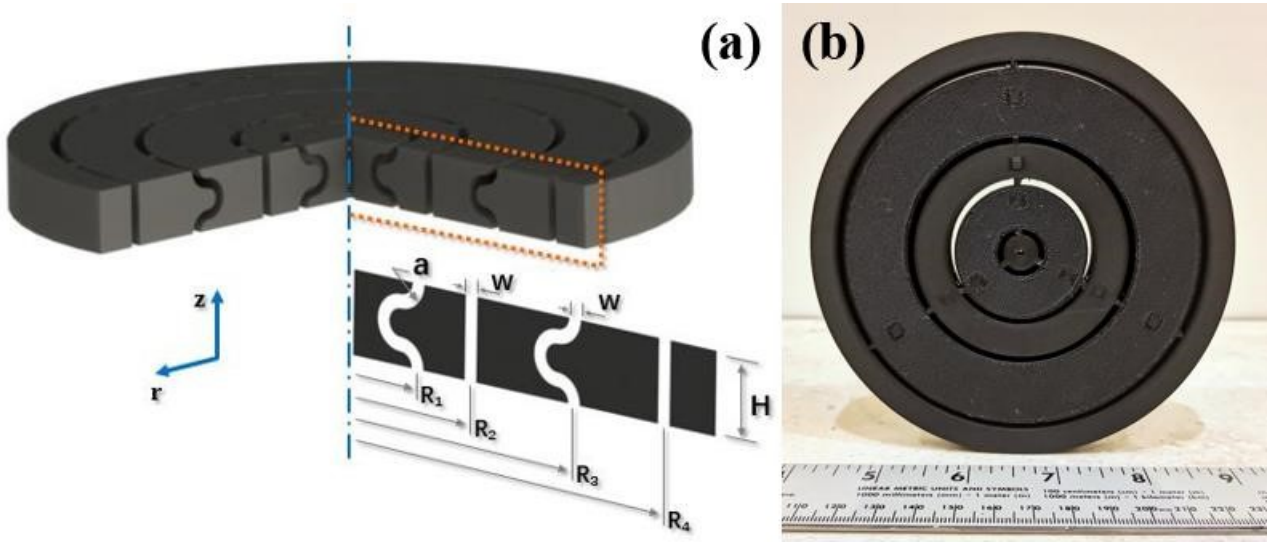

Figure 4.1: (a). Schematic diagram of the lens. H, w, a, and R_i refer to the axial thickness, the width of the channel, the radius of the curved edge, and the central radius of each channel, respectively. For this specific design, $H = 12$ mm, $w = 2$ mm, $a = 4$ mm, $R_1 = 12.2$ mm, $R_2 = 21.4$ mm, $R_3 = 39.4$ mm, and $R_4 = 55$ mm. (b). Photograph of the 3-D printed experimental sample.

To create constructive interference along the axial direction (Z-direction), the frequency f, phase $\Phi(R_i)$, focal distance L_c, and central radii of channels in the i_{th} order R_i, are selected to satisfy the following expressions [42, 44]:

$$\frac{nc}{2f} = \sqrt{R_{i-1}^2 + L_c^2}, \tag{4.1}$$

$$\Phi(R_i) = \pm 2n\pi + \Phi_0 - \frac{\pi}{f}(\sqrt{R_i^2 + L_c^2} - L_c). \tag{4.2}$$

Φ_0 is the reference phase of the central channel, which can be set to Φ_0=0. The subscript i is the order of the channel, and n is an arbitrary integer. These equations indicate that a series of discrete constructive points can be created at the designated frequencies by means of multiple combinations of n and R_i. Meanwhile, the phase shift of the transmitted sound varies with

different axial (Z-direction) and radial (R-direction) locations. Later observations in the simulations and experiments prove that the distributions of the constructive nodes can be achieved within a certain frequency range, producing sound beams over consecutive frequencies.

To obtain the preliminary form of this design, the acoustic pressure performances of transmitted sound were analyzedwith a finite element model by using COMSOL Multiphysics. The viscothermal domain was included in modelling of the perforated channels for the loss effect, due to the small size of the channels. The monitored area was set to be 70 cm wide in the R-direction and 90 cm long in the Z-direction. Perfectly matched layers (PMLs) were applied to the outer boundaries of upstream and downstream to mimic the anechoic far-field. The incident plane wave was positioned at the center of the R-direction, and a frequency sweep was performed along the positive Z-direction from 8070 to 8270 Hz with 1 Hz increments.

Fig. 4.2 shows a schematic diagram of the experimental setup. A 2.5 in loudspeaker (ND65-4) was placed inside a soundproof case behind the lens to avoid sound leakage in the transverse direction. A 0.25 in microphone (Beyer Dynamic MM1) scanned the sound pressure over the downstream area. Anechoic foam walls enclosed the testing area to avoid reverberations. The room temperature was 24 ^{o}C.

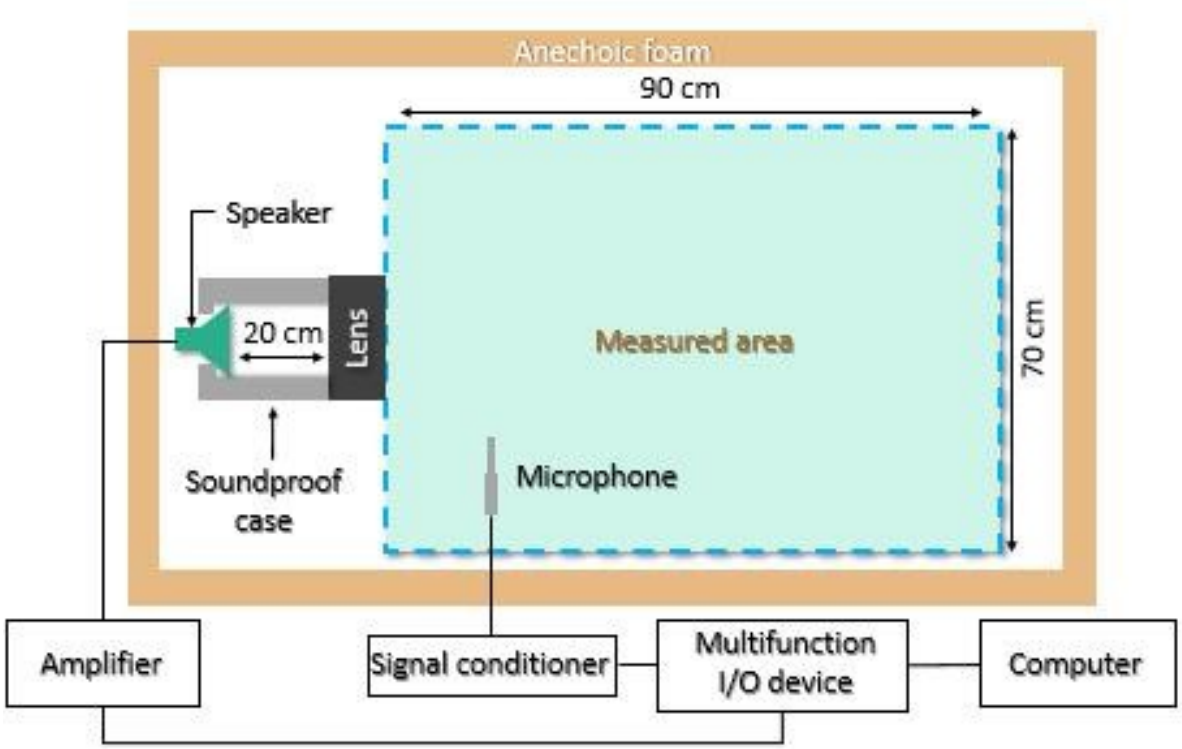

Figure 4.2: Schematic of the experimental setup

Figs. 4.3 to 4.5 show the selected simulated and experimental results of normalized sound pressure. In Figs. 4.3 and 4.4, the simulation and experiment with the lens are shown, respectively. In Fig. 4.5, an experiment without the lens is shown as a control case. To distinguish the pressure distribution, the normalized values bigger than 0.8 are considered to be concentrations. Values smaller than 0.8 are considered as diffractions. At 8120 Hz, a concentrated beam is observed in both the simulated and experimental results. A sharp focal point is measured at approximately 5 cm in the Z-direction. A thin constructive beam following this focal point phenomena has a length of approximately 2λ, making the total length of the concentration area achieved to be approximately 5.92λ. At 8170 Hz, the total concentration length increases to approximately 9.55λ. In particular, the most noticeable sound beam occurs at 8219 Hz, whose experimental result illustrates a nearly perfect beam shape with a length of 15.58λ, with a width limited to 3.59λ. As the frequency is further increased, the concentration strength weakens, and the beam length decrease to 6.03λ at 8270 Hz. Inspecting Eq. 4.1 with respect to concentration

lengths with respect to the radii R_3 and R_4, this equation yields $n = 24$ for 8120 Hz, $n = 40$ for 8170 Hz, $n = 62$ for 8219 Hz, and $n = 25$ for 8270 Hz.

For the lens, the destructive lobes are observed in the transverse direction and diffractions are effectively limited beside the axial beam. Comparison of the corresponding simulated predictions are in good agreement with the corresponding observations of the experimental measurements. Some minor discrepancies are observed due to the difference between the ideal numerical models and physical setups [41, 92]. In comparison, for the control case without a lens, constructive sidelobes along the transverse directions can be seen for all frequencies. Additionally, no sound pressure concentration was observed in the axial direction over the testing band. This effectively verifies the ability of the acoustic lens design with U-shaped channels to create a long-distance, directional projection of a sound wave.

In order to obtain a better understanding of the pressure manipulation, the phase distribution was also investigated. For the experimental cases with and without the lens, the phase profiles for a frequency of 8219 Hz are shown in Fig. 4.6. In Fig. 4.6(a), the in-phase (phase matching) interference in the central region may be seen for the case with the lens. The results are out-of-phase on the two flanks corresponding to the pressure resonance and anti-resonance for the lens. For the areas in between, local phase gradients make the evanescent waves undergo destructive interference. In other words, the phase mismatching equivalently increases the local impedance to prohibit the energy from scattering into free space [89]. Inspecting Eq. 4.2 with n for 8219 Hz and $\Phi(R_4) = -157.08^o$, the result agrees well with the measured phase of the beam front in Fig 4.6(a).

For the control case of 8219 Hz in Fig 4.6(b), the constructive lobes are in a "V" pattern for the control group, and the open angle is approximately 52^o. The open angles at 8120, 8170, and 8270 Hz are approximately 54^o, 50^o, and 42^o, respectively.

Fig. 4.7(a) depicts the measured beam lengths versus the scanning frequencies. The focal length at the starting frequency of 8070 Hz is approximately 10 cm, which is a rather short focal point. Interestingly, this shows a close similarity to observations from other work [41]. Sweeping upwards in frequency, the beam length increases to 65 cm at 8219 Hz. This is followed by decreasing beam lengths, culminating at 25 cm at 8270 Hz. The measured pressure

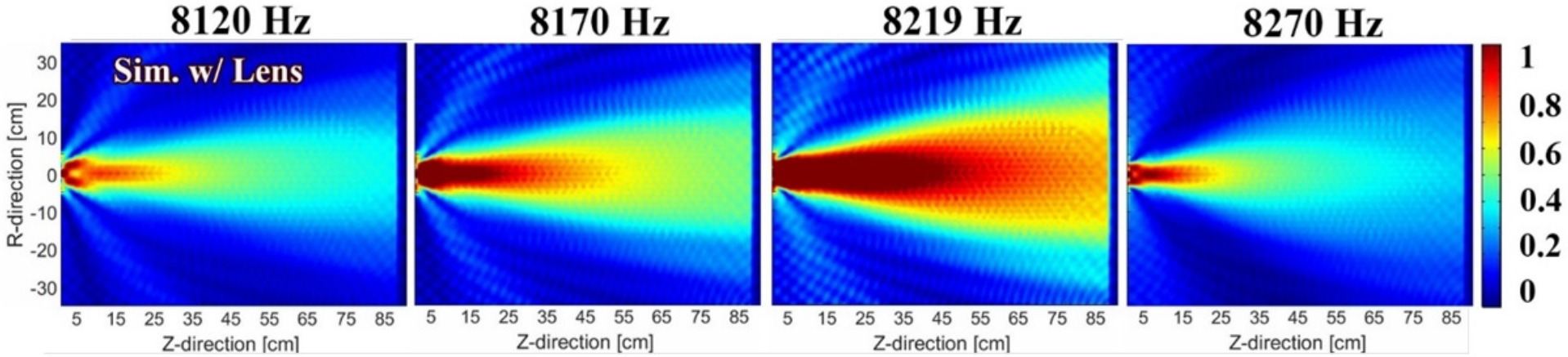

Figure 4.3: The normalized sound pressure distributions of the downstream area for selected frequencies. Simulated results of the acoustic Fresnel lens.

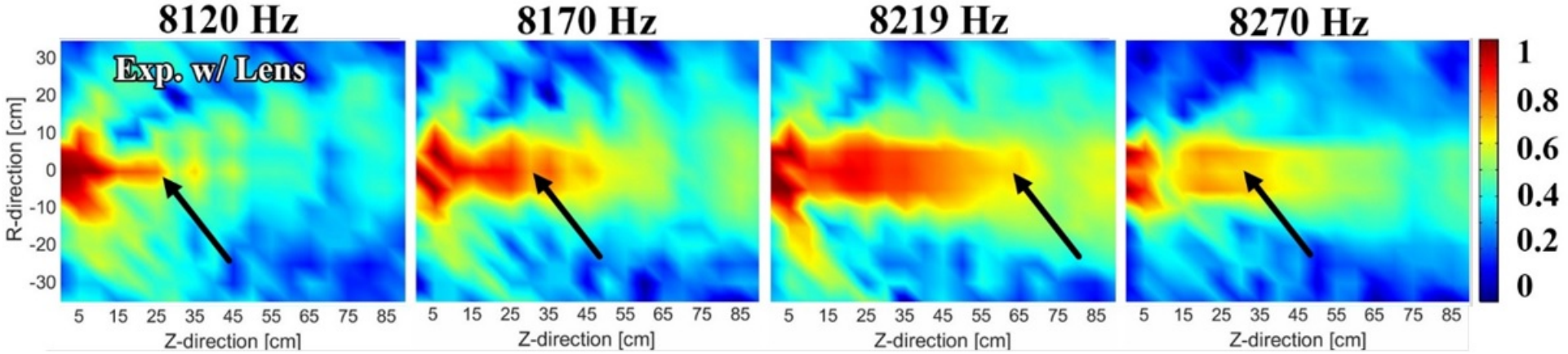

Figure 4.4: The normalized sound pressure distributions of the downstream area for selected frequencies. Experimental results of the acoustic Fresnel lens.

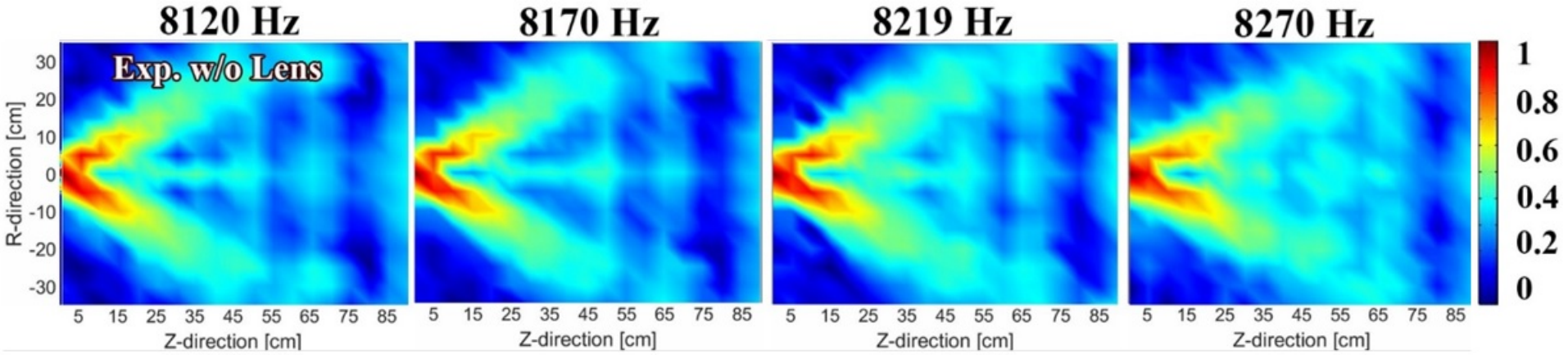

Figure 4.5: The normalized sound pressure distributions of the downstream area for selected frequencies. Black arrows identify the beam fronts at each frequency.

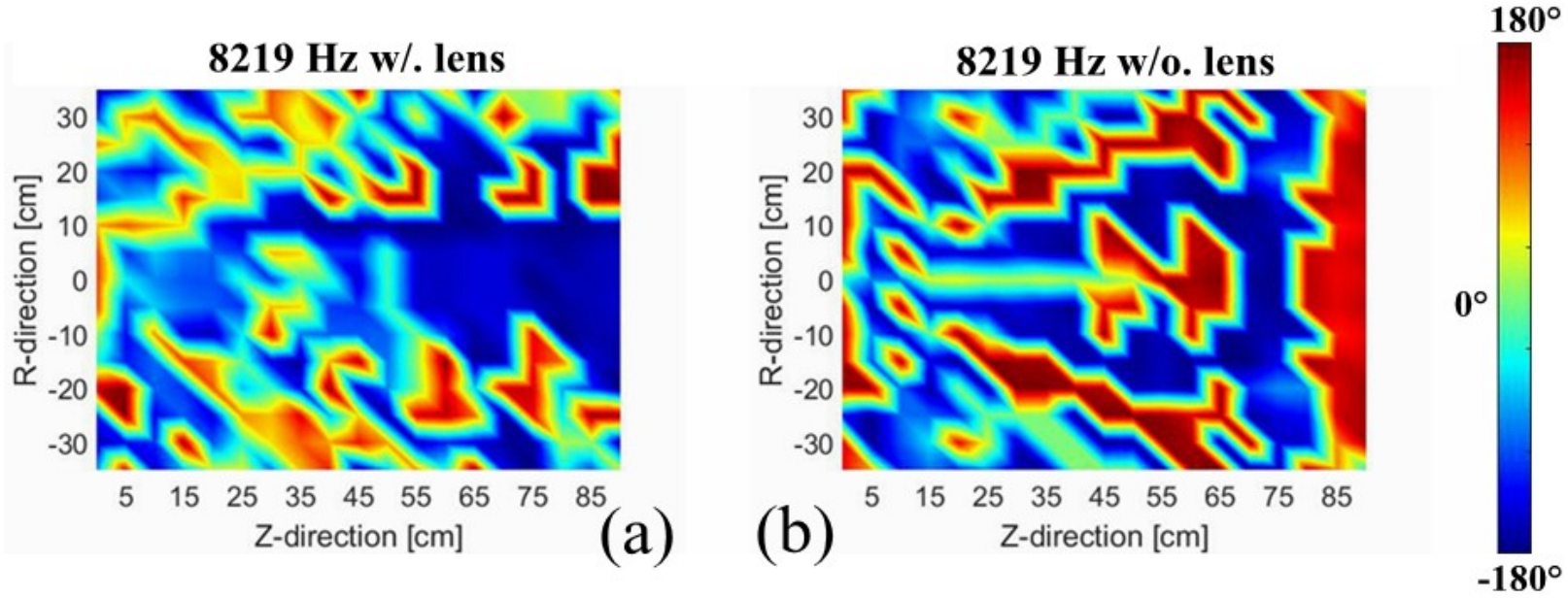

Figure 4.6: Experimental phase distributions of downstream area at 8219 Hz. (a) Case with acoustic Fresnel lens; (b) Control case without lens.

distributions of the beam front in the R-direction are detailed in Fig. 4.7(b) to (e). For the control case without the lens, the sound pressures exhibit the pattern of a flattened "M", which produces a relatively even sound pressure across the transverse direction. After the lens is included, the pressure distributions are changed significantly. At 8120 Hz, the pressure is similar to the control case when $R \leq 5$ cm, but a dramatic 45.6% pressure drop happens in the range of $5 < R < 30$ cm. With increasing frequencies, not only does the pressure decrease in far radial positions, but the center pressures are also constructive. Comparing the pressure between the center of "w/. lens" and "w/o. lens", the difference are 39.8%, 21.1%, and 28.6% at 8217 Hz, 8219 Hz and 8270 Hz respectively. Furthermore, according to Fig. 4.7(b) to (e) the diffraction at the beam head is limited to within approximately 0.24λ, 0.47λ, 0.72λ, and 0.48λ, respectively. According to Figs. 4.3 to 4.5, higher differences and wider diffraction limitations would be more obvious inside the beam zones (for shorter Z-distances). The resolutions may not be as effective as lenses for short-distance focusing [42], but this novel lens clearly produces a central, concentrated sound beam for longer distances.

4.3 Summary

In summary, the design of a flat Fresnel lens with enhanced directional transmission capable of sustaining a sound beam over a long distance and over a wide frequency band, was proposed and studied. Numerical simulations and experimental results are presented, which are in good agreement. This lens produced a noticeable diffraction-limited sound beam along the central axial direction in the range from 8120 to 8270 Hz. The sound beam can reach up to 15.58λ long at 8219 Hz, and the width of the beam is limited within 3.59λ. The conceptual and experimental work shown in this paper demonstrates that this lens design as a promising candidate for several real-world applications. In future research, the size of the lens will be modified to test the scalability of this design for a broader working frequencies and a longer beam distance.

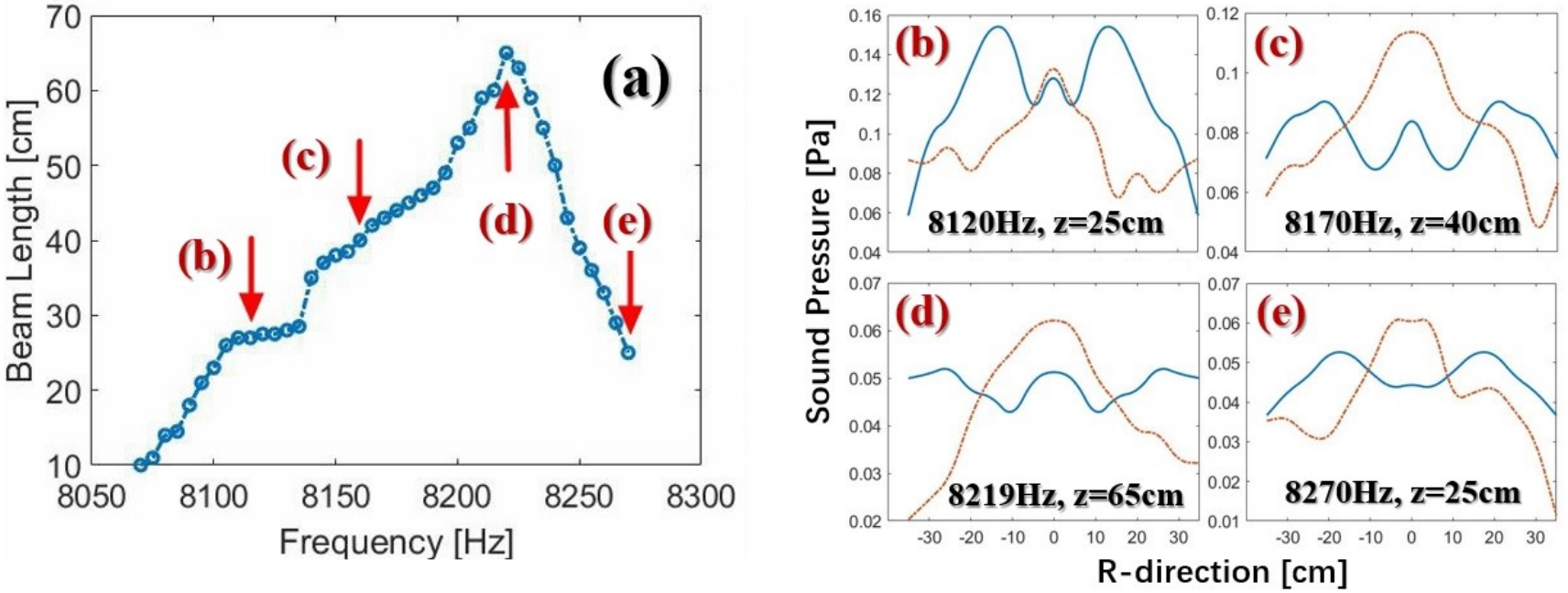

Figure 4.7: Experimental phase distributions of downstream area at 8219 Hz. (a) Case with acoustic Fresnel lens; (b) Control case without lens.

Chapter 5

Compact Acoustic Metalens with Sinusoidal Sub-channels for Directional Far-field Sound Beams

5.1 Introduction

A metasurface lens (i.e., metalens), composed of perforated sinusoidal channels evenly arrayed with sub-wavelength distances, is explored in this chapter. Enhanced directional far-field sound transmission over a large frequency range was realized through using this compact metalens. Numerical simulations and experimental tests demonstrated a pronounced diffraction-limited sound beam from 7390 to 7600 Hz, which reached as far as 57.6 cm at 7551 Hz with a width of 9 cm. This metalens is a feasible candidate for directional sound projection and sound energy harvesting.

For decades, research has been undertaken to manipulate sound propagation for designated performance, especially for long-distance, directional acoustic projection. This process is similar to focusing light with a lens. It is still a challenging task to conduct sophisticated manipulation of the impedance mismatching with the host medium by controlling the phase of audible sound waves, rather than modulating ultrasonic waves, such as parametric acoustic arrays (PPAs) [83, 85, 97, 98]. With advances of acoustic metasurfaces (AMs), innovative, extraordinary functionalities make passive lenses an attractive substitute for PAAs due to ease of implementation and lower cost [1, 2, 35, 36, 41, 42, 43, 44, 45, 46, 47, 48, 67, 86, 88, 89, 90, 91, 92, 93, 94, 95, 96, 99, 100].

Unlike conventional materials, acoustic metasurfaces modify sound waves with some artificial characteristics not found in nature. Enhanced acoustic performance can be accomplished by engineered phase interactions, which is based on the Huygens-Fresnel principle and by

means of elaborately spaced sub-structures of AMs [36, 45, 46, 47, 67, 88, 89, 90, 91]. More recently, adequate sound transmission for near-field point-focusing with limited diffraction has demonstrated the efficiencies at some designated frequencies [41, 42, 44, 47, 48, 86, 91, 92, 93, 94, 95, 96]. Inspired by the efforts above, an innovative metalens is proposed and tested, in which the sound wave must pass through subwavelength-spaced perforated sinusoidal channels. Observations of long-distance, concentrated sound beams at a wide frequency band distinguish this approach from previous designs for a single focal point in the near field. The considerably concentrated transmission with lessened sound pressure in the neighboring area makes the proposed metalens a feasible candidate for diverse applications, including directional sound projection, non-contact sonic picking, acoustic wave steering, and acoustic energy harvesting. In the next section, the observed beams are reported over a feasible frequency range, and the focal characteristics on the influences of structural parameters were investigated.

5.2 Metalens Design, Experiment, and FEM

The acoustic metalens was constructed on a thin plate perforated with equally-spaced channels composed of shifted sinusoids in a symmetric pattern, as illustrated in Fig. 5.1. Each channel is bordered by two solid walls. In Fig. 5.1(b), the pattern for the lens is depicted, which is symmetric about Channel 1. For each channel, one sinusoidal wall is simply a translation, while the other sinusoidal wall is shifted following the expression $2\sin(\frac{\pi s}{10}+n\theta)$, where s is the lens thickness, the shifting angle is $\theta = \pi/4$, and n is the channel number ($n = 1$ denotes the curvatures of Channel 1). For instance, the left wall of Channel 1 and the left wall of Channel 2_{right} are the same; whereas, the right wall of Channel 2_{right} is shifted. To be clear, all of the walls that separate the channels are fixed to the top and bottom portion of the lens, as seen in Fig. 5.1(a). The channel periodicity, $H = 1.65$ cm, and lens thickness, $s = 4$ cm, are on the subwavelength scale. By employing these shifting walls, the width of channels' exits and their effective length are deliberately controlled for creating constructive interference along the Z-direction [44, 92, 96].

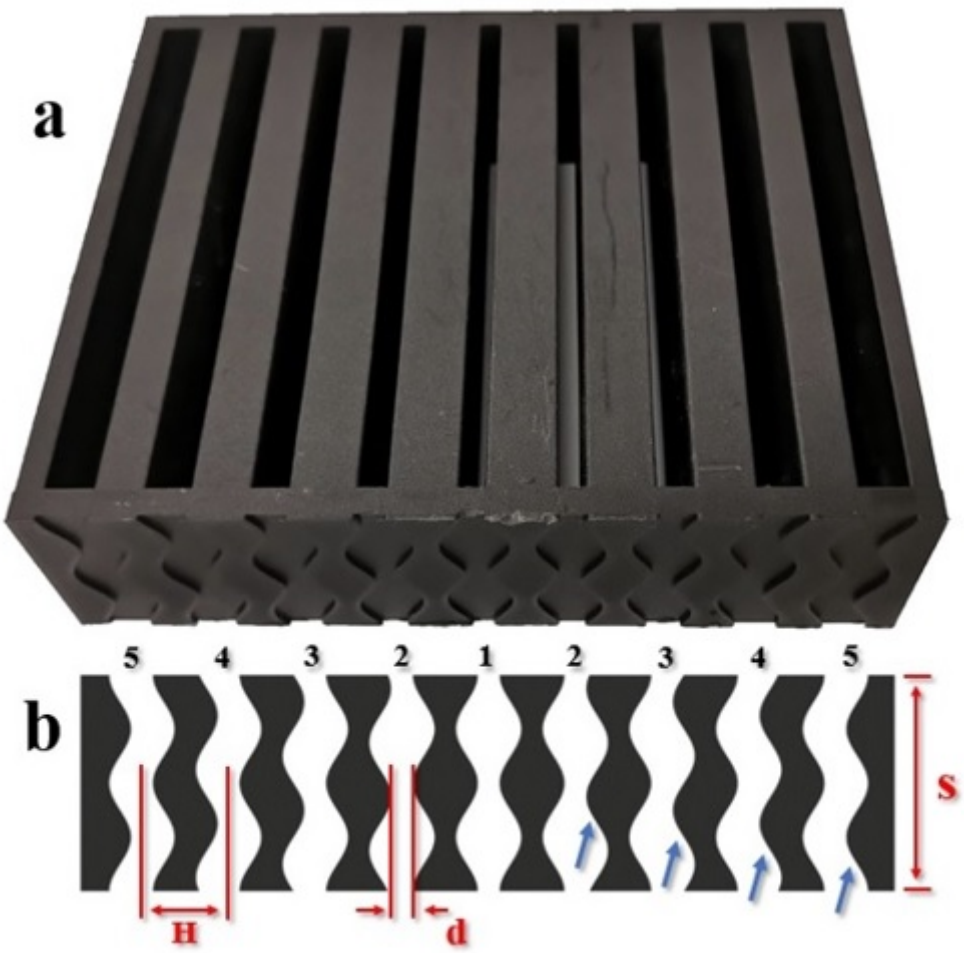

Figure 5.1: (a) Photograph of the experimental metalens, which was 3-D printed using a Markforged Mark Two. Imprints on the base depict the shape of the inner channels. (b) Schematic diagram of the lens. $H = 1.65$ cm, $d = 0.4$ cm, and $s = 4$ cm refer to the periodicity, the minimum width of each channel, and the thickness of the lens, respectively. Blue arrows denote the shifting walls of each channel.

In Fig. 5.2, the experimental setup is depicted. A microphone was used to scan the downstream area to measure the efficacy of the metalens. To design the metalens, a battery of simulations was performed to ascertain the constraints of the experimental setup. In these simulations, a plane wave was implemented upstream to the lens. The experiment was designed to have a sound source that was consistent with this, by using a single 2.5" loudspeaker with a tight fit case, as depicted in Fig. 5.2. A Markforged Mark Two printer was chosen to use the proprietary "Onyx" material, which is a chopped carbon fiber thermoplastic composite that is

much stiffer than conventional print filament. Additionally, this printer produces a fine surface finish to minimize the effects of the surface on the acoustic phenomena. The build platform for this printer is $32.0 \times 13.2 \times 15.4$ cm. The metalens has a height of 15.0 cm, a thickness of 4.0 cm, and a width of 12.5 cm to be within these constraints.

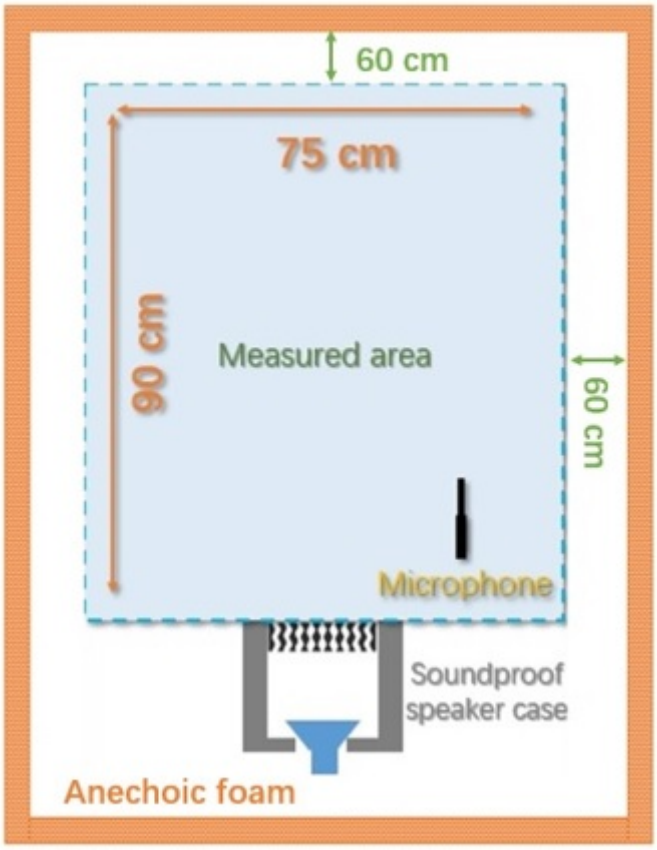

Figure 5.2: Schematic diagram of the experimental setup. A loudspeaker was placed inside a soundproof case behind the lens. A microphone was used to scan the sound performance over a 90×75 cm^2 area. Anechoic foam walls were applied to avoid reverberations.

The metalens, which was 3-D printed for the experiment, was also modeled using an FEM solver (COMSOL Multiphysics) in order to evaluate the transmitted sound field. The viscothermal effect was included in the model for the channels, due to their small size [86]. Plane wave signals were positioned along the positive Z-direction from 7380 to 7610 Hz at $20°$C. For the experiment, pyramid-shaped sound insulation foam was placed 60 cm from the downstream testing area as depicted in Fig. 5.2. This foam has a low reflectivity. But in addition, according to the inverse square law ($p^2 \approx \frac{1}{(r_1/r_0)^2}$), the sound pressure at the nearest foam wall is 54 times

less than the pressure near the metalens. For the simulation, Perfectly Matched Layers were implemented to mimic the non-reflecting far-field conditions of the experiment.

Selected simulated and experimental results of normalized sound pressure are illustrated in Figs. 5.3 to 5.5. The top two rows show the FEM simulation and experiment with the lens, respectively. The experimental results without the lens are shown in the third row as a control case. To distinguish the pressure distribution, 70% of the normalized pressure is considered to be the threshold of concentration. In the following discussion, the length of the beam is considered to be the furthest distance from the metalens that has a pressure of at least 70% of the normalized pressure. If this threshold was reduced, the absolute length of the beam in the Z-direction in Fig. 5.4 would increase.

At 7380 Hz, a concentrated region appears in both the simulated and experimental results. The concentration length is measured to be approximately $Z = 29.6$ cm, equivalent to 6.4λ. At 7486 Hz, a nearly perfect concentrated beam is observed with a total concentration length increasing to approximately 9.8λ (44.8 cm) and with a width limited to 1.9λ. The diffraction in the transverse direction are effectively limited beside the axial beam. In particular, the most noticeable sound beam occurs at 7551 Hz, where the experimental results show the longest beam with a length of 12.3λ (55.9 cm) and two sidelobes, as predicted by the simulations. As the frequency is further increased to 7610 Hz, diffraction occurs instead of a centrally concentrated beam, and the sound field pattern exhibits a "palm" shape with sidelobes as expected. For 7551 Hz and 7610 Hz, some destructive areas are observed between the sidelobes and the central beam. For detailed experimental pressure distribution from 7390 to 7610 Hz. Despite the minor discrepancies due to differences between the ideal numerical models and physical experiments, the FEM predictions agree well with the corresponding experimental measurements [41, 92].

As a comparison, for the control case without a lens, the sound pressure spreads in a 46° "opened V" pattern at the exit of the speaker case for all frequencies with the highest amplitude. Then, it disperses through the testing area in a gradually fading manner, with the amplitude roughly from 30% to 50% of the normalized pressure. No obvious axial concentrations are

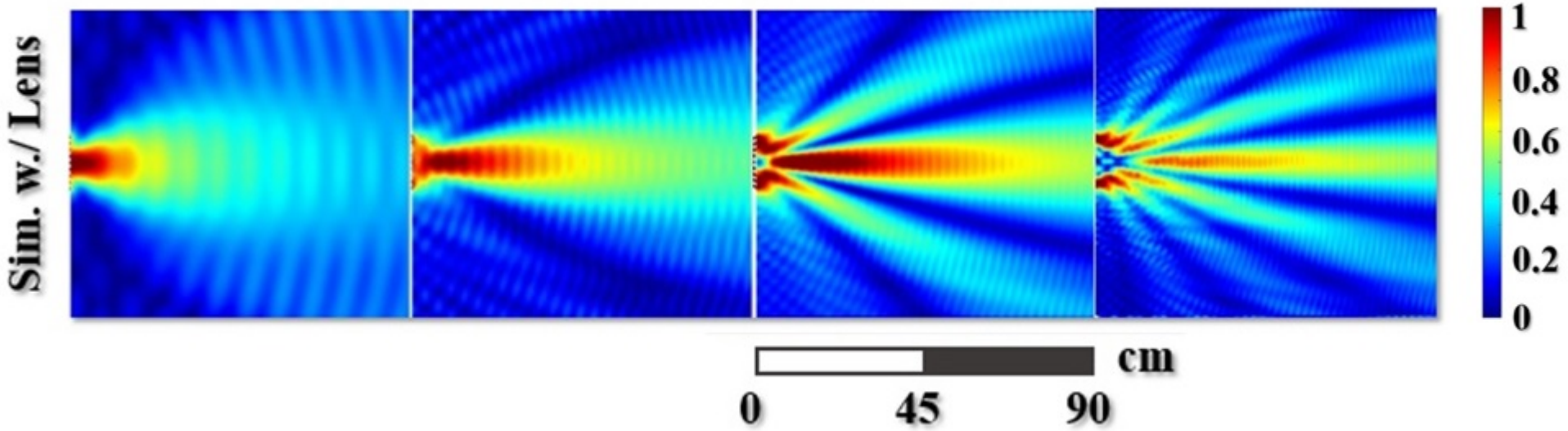

Figure 5.3: The normalized sound pressure distributions for selected frequencies. Simulated results of the acoustic metalens.

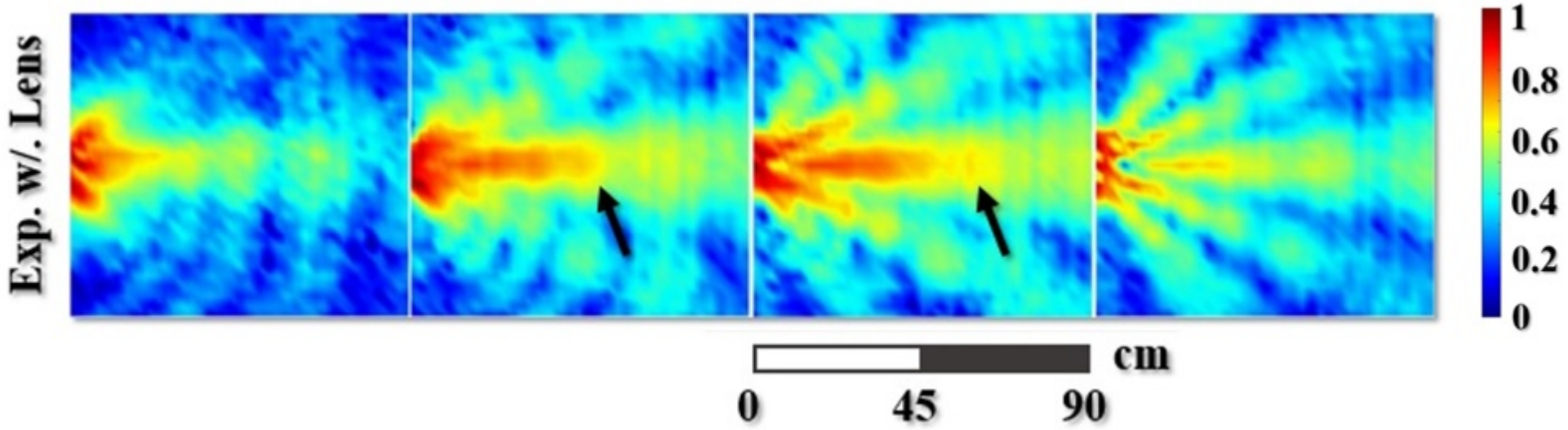

Figure 5.4: The normalized sound pressure distributions for selected frequencies. Experimental results of the acoustic metalens. Black arrows indicate the positions of beam front.

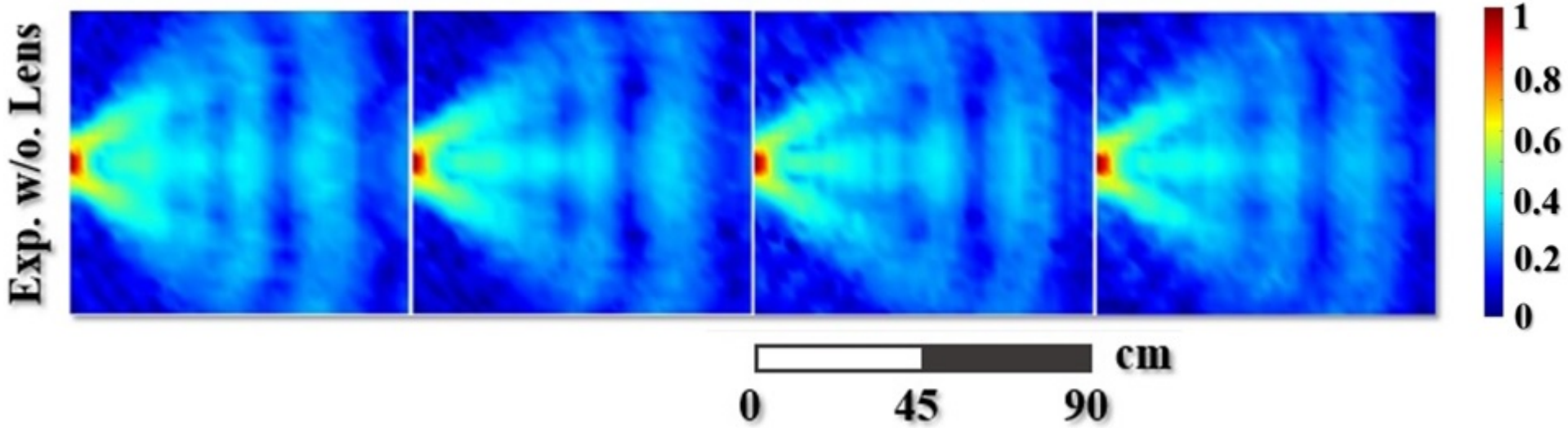

Figure 5.5: The normalized sound pressure distributions for selected frequencies. Experimental results without the acoustic metalens, as a control case. As expected, the sound quickly dissipates.

observed. Thus, this experiment effectively verifies the ability of the acoustic metalens to concentrate a narrow sound beam over a long distance.

In order to obtain a better understanding of the pressure distribution, a further investigation of specific details was performed. Fig. 5.6(a) depicts the measured beam lengths versus the scanning frequencies. At the starting frequency of 7380 Hz, the focal length is approximately 11.0 cm, which generates a similar focal point to that observed in other work [41, 42, 44, 47, 94, 95, 96]. Sweeping upwards in frequency, the beam length increases, before reaching 55.9 cm at 7551 Hz. After this frequency, the beam lengths decrease, culminating at 31.8 cm at 7610 Hz. At the Z-position of each beam front, the measured pressure distributions of both the lens and the control case in the R-direction are detailed in Fig. 5.6(b-e). For the control case, the sound pressures exhibit a "flattened W" pattern, which indicates a relatively even sound pressure distribution across the transverse direction. After the lens is included, a significant change of pressure distributions was observed. At 7380 Hz, nearly identical distributions with the control case appear when $R \leq 5$ cm, but a dramatic 47% pressure difference $(\frac{P_{Lens}-P_{ctrl}}{P_{ctrl}} \times 100\%)$ happens at $R = 0$ cm. With increasing frequencies, the sound pressures along the central line are changed considerably, but also the pressures in the far transverse positions increase due to constructive interference. Comparing the pressure between the center of the "w/. lens" and "w/o. lens" cases, the differences are 96.7%, 73.9%, and 54.8% at 7486 Hz, 7551 Hz, and 7610 Hz, respectively. Though the longest beam occurs at 7551 Hz, the most effective concentration happens at 7486 Hz. According to these observations, the beam frequency range can be considered from 7390 to 7600 Hz with rather even pressure distributions inside the sound beams. The effectiveness of the concentration may not be as high as lenses for short-distance focusing, but this innovative metalens clearly produces a central, concentrated sound beam for longer distances over a wide frequency band.

In Fig. 5.6(g), the in-phase interference is limited within 34° in the central region with the lens at 7551 Hz. The out-of-phase portion on the two flanks corresponds to the anti-resonance. For the areas in between, local phase gradients make the evanescent waves undergo destructive interference [88]. This phase distribution corresponds to its sound pressure distribution in Fig. 5.4. For the control case in Fig. 5.6(f), the in-phase interference is in a "double V" pattern

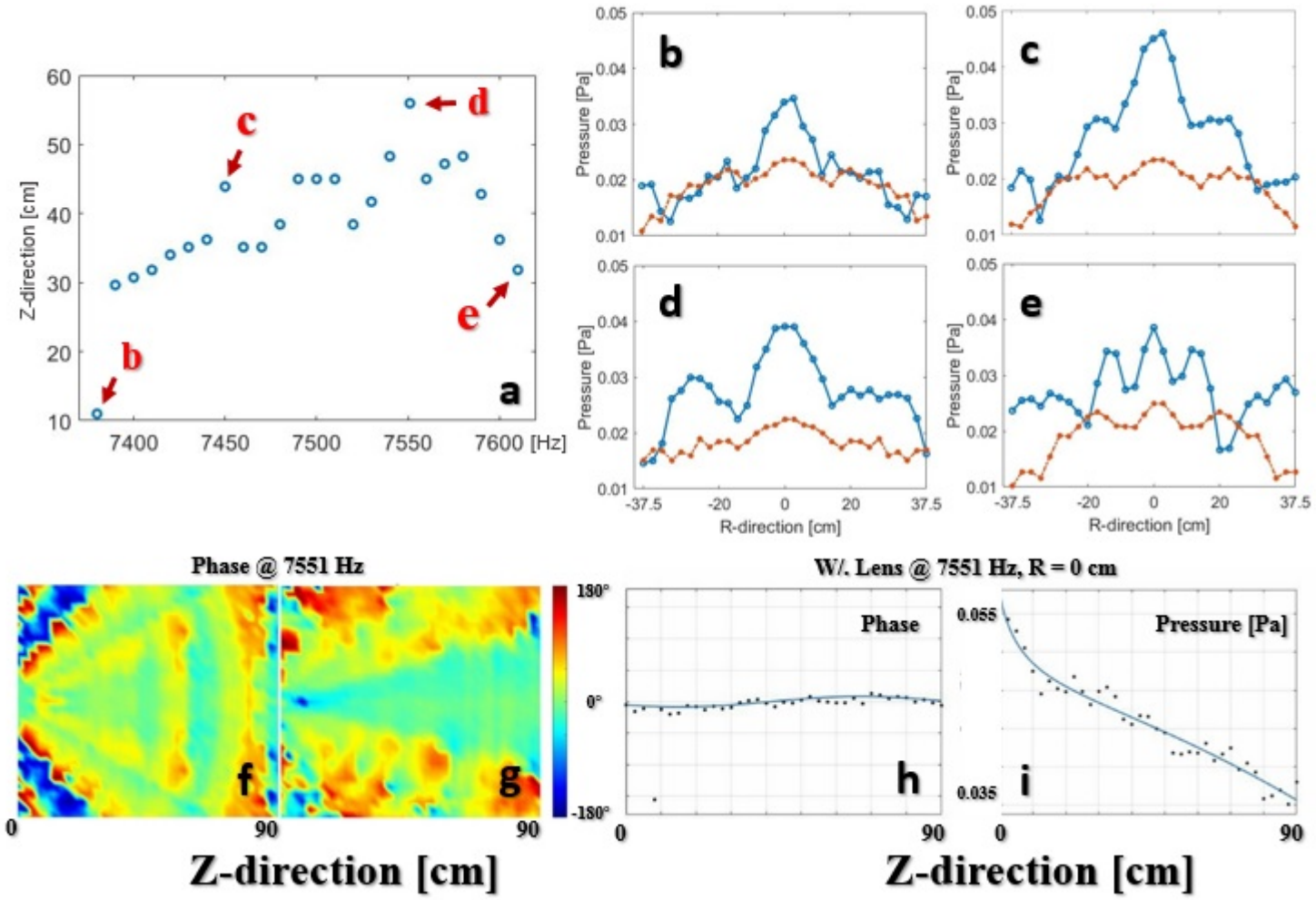

Figure 5.6: (a) Beam length vs. frequency. (b-e) At beam front positions ($Z = 11.0$ cm, $Z = 44.8$ cm, $Z = 55.9$ cm, and $Z = 31.8$ cm), the sound pressure distribution in the R-direction at 7380 Hz, 7486 Hz, 7551 Hz, and 7610 Hz. Blue and red lines refer to "w/. lens" and "w/o. lens", respectively. (f-g) The phase distribution at 7551 Hz with the lens and without the lens, respectively. (h-i) The measured data points (black) and fitted curves (blue) with the lens at 7551 Hz and $R = 0$ cm.

with open angles of 45° and 91°, approximately, which occupies most of the measured area and corresponds to the wide sound pressure distribution for the control case at 7551 Hz.

5.3 Empirical Model

To facilitate a better understanding for coupling the geometric parameters and sound distribution characteristics, functions relating the phase and sound pressure are proposed. These are geometry dependent at 7551 Hz and $R = 0$ cm. By applying the least-mean-square method similar to the estimation for β and ϕ for a cylindrical wave interacting with a variable width grate [92], the following equations are obtained:

$$\phi = 2\sin(\frac{Ze^f}{sHn^2 - \frac{n}{2}})\sin(0.2f - 2n^2s + d) \tag{5.1}$$

$$P = \frac{1}{Z + nsH\cos(\frac{\theta f}{2n\pi^2}) - W\sin(\frac{\theta f}{2n\pi^2})} \tag{5.2}$$

, where Z is the position in the Z-direction in cm, $f = 7551$ Hz, and $n = 5$. Fig. 5.6(h-i) depict the fitted expression and the measured data, illustrating the good agreement.

5.4 Summary

An innovative design for an acoustic metalens is proposed and studied, which exhibits a narrow sound beam over a long distance and a wide frequency band. It was demonstrated that simulation results are in good agreement with the experimental observations. This metalens produced a noticeable diffraction-limited sound beam along the central axial direction from 7390 to 7600 Hz. The sound beam can extend to a length of 12.3λ at 7551 Hz, and the width of the most effective beam is limited within 1.9λ at 7468 Hz. The conceptual and experimental work for this lens shows the potential ability for several real-world applications, including directional sound projection and acoustic energy harvesting.

Chapter 6

Conclusion

In this dissertation, four kinds of acoustic metamaterials in two categories (super sound attenuation metamaterials and directional acoustic beamforming metalens) are demonstrated in detail and discussed.

The first sound attenuator, a micro scale open-through dual expansion chamber (ODEC) package, achieves high and continuous attenuation from 2000 to 8200 Hz. Corresponding experiments with 18 configurations of the ODECs and related control group samples (non-ODEC) were conducted to validate the theoretical predictions with respect to transmission loss (TL). The geometric effect of the TL is also investigated with respect to chamber length and radius. The ODECs perform in the manner of low-pass filters and their corresponding highest transmissions range from 28.87 to 44.51 dB at 8100 Hz.

The second sound attenuator, an air permeable labyrinth element (LE) acoustic metamaterial, provides low sound transmissions under 500 Hz, which is air permeable and insusceptible to circumambient changes. Low transmission, low reflection, and high absorption are theoretically expected from the complex open through structure at deep sub-wavelength scale. Experimental results and simulations meet the expectations of high absorption, a substantial near unity absorption from 223 to 327 Hz, and experimentally exhibit impedance matching in this broad low-frequency range.

The first metalens, a flat Fresnel lens, demonstrated outstanding sound beams from 8120 to 8270 Hz. The longest beam can reach as far as 65 cm at 8219 Hz with 15 cm width of the beam.

The second metalens, a perforated sinusoidal channel array with sub-wavelength distances, exhibited enhanced directional far-field sound transmission over a large frequency range. Numerical simulations and experimental tests demonstrated a pronounced diffraction-limited sound beam from 7390 to 7600 Hz, which reached as far as 57.6 cm at 7551 Hz with a width of 9 cm.

The conceptual and experimental work of these four compact air permeable acoustic metamaterials demonstrate the outstanding performance of sound absorption and transmissive sound focusing with wide frequency bands. This show the potential abilities for sound manipulations in industry, aerospace, medicine, pharmacy, ocean applications, and etc.

References

[1] M. R. Haberman and M. D. Guild, "Acoustic metamaterials," Physics Today, vol. 69, no. 6, pp. 42–48, Jun. 2016.

[2] B. Assouar, B. Liang, Y. Wu, Y. Li, J.-C. Cheng, and Y. Jing, "Acoustic metasurfaces," Nature Reviews Materials, vol. 3, no. 12, pp. 460–472, Oct. 2018.

[3] V. G. Veselago, "The Eelectrodynamics of Substances with Simultaneously Negative Values of ϵ and μ," Soviet Physics Uspekhi, vol. 10, no. 4, pp. 509–514, Apr. 1968.

[4] J. B. Pendry, A. J. Holden, D. J. Robbins, and W. J. Stewart, "Magnetism from conductors and enhanced nonlinear phenomena," IEEE Transactions on Microwave Theory and Techniques, vol. 47, no. 11, pp. 2075–2084, 1999.

[5] R. A. Shelby, "Experimental Verification of a Negative Index of Refraction," Science, vol. 292, no. 5514, pp. 77–79, Apr. 2001.

[6] H.-T. Chen, A. J. Taylor, and N. Yu, "A review of metasurfaces: physics and applications," Reports on Progress in Physics, vol. 79, no. 7, p. 076401, Jun. 2016.

[7] F. Capolino, "Theory and Phenomena of Metamaterials," Oct. 2009.

[8] F. Ding, A. Pors, and S. I. Bozhevolnyi, "Gradient metasurfaces: a review of fundamentals and applications," Reports on Progress in Physics, vol. 81, no. 2, p. 026401, Dec. 2017.

[9] A. Pors, F. Ding, Y. Chen, I. P. Radko, and S. I. Bozhevolnyi, "Random-phase metasurfaces at optical wavelengths," Scientific Reports, vol. 6, no. 1, Jun. 2016.

[10] H.-H. Hsiao, C. H. Chu, and D. P. Tsai, "Metasurfaces: Fundamentals and Applications of Metasurfaces (Small Methods 4/2017)," Small Methods, vol. 1, no. 4, Apr. 2017.

[11] M. L. Munjal, "Advances in the acoustics of flow ducts and mufflers," Sadhana, vol. 15, no. 2, pp. 57–72, Sep. 1990.

[12] P. Leclaire, "Fundamentals of Physical Acoustics," Applied Acoustics, vol. 63, no. 5, pp. 579–581, May 2002.

[13] I. L. Vr and L. L. Beranek, Eds., "Noise and Vibration Control Engineering," Oct. 2005.

[14] J. Mei, G. Ma, M. Yang, Z. Yang, W. Wen, and P. Sheng, "Dark acoustic metamaterials as super absorbers for low-frequency sound," Nature Communications, vol. 3, no. 1, Jan. 2012.

[15] M. Yang, G. Ma, Z. Yang, and P. Sheng, "Coupled Membranes with Doubly Negative Mass Density and Bulk Modulus," Physical Review Letters, vol. 110, no. 13, Mar. 2013.

[16] P. Sheng, "Coupled membranes with doubly negative mass density and bulk modulus," The Journal of the Acoustical Society of America, vol. 134, no. 5, pp. 4026–4026, Nov. 2013.

[17] G. Ma, M. Yang, S. Xiao, Z. Yang, and P. Sheng, "Acoustic metasurface with hybrid resonances," Nature Materials, vol. 13, no. 9, pp. 873–878, Jun. 2014.

[18] Y.-F. Li, J. Lan, H.-Y. Yu, X.-Z. Liu, and J.-S. Zhang, "Membrane-based acoustic metamaterial with near-zero refractive index," Chinese Physics B, vol. 26, no. 1, p. 014302, Jan. 2017.

[19] J. Lan, Y. Li, H. Yu, B. Li, and X. Liu, "Nonlinear effects in acoustic metamaterial based on a cylindrical pipe with ordered Helmholtz resonators," Physics Letters A, vol. 381, no. 13, pp. 1111–1117, Apr. 2017.

[20] Y. Li and B. M. Assouar, "Acoustic metasurface-based perfect absorber with deep subwavelength thickness," Applied Physics Letters, vol. 108, no. 6, p. 063502, Feb. 2016.

[21] H. Chen, H. Zeng, C. Ding, C. Luo, and X. Zhao, "Double-negative acoustic metamaterial based on hollow steel tube meta-atom," Journal of Applied Physics, vol. 113, no. 10, p. 104902, Mar. 2013.

[22] H.-C. Zeng, C.-R. Luo, H.-J. Chen, S.-L. Zhai, C.-L. Ding, and X.-P. Zhao, "Flute-model acoustic metamaterials with simultaneously negative bulk modulus and mass density," Solid State Communications, vol. 173, pp. 14–18, Nov. 2013.

[23] W. N. Yunker, C. B. Stevens, G. T. Flowers, and R. N. Dean, "Sound attenuation using microelectromechanical systems fabricated acoustic metamaterials," Journal of Applied Physics, vol. 113, no. 2, p. 024906, Jan. 2013.

[24] J.-P. Groby, C. Lagarrigue, B. Brouard, O. Dazel, V. Tournat, and B. Nennig, "Enhancing the absorption properties of acoustic porous plates by periodically embedding Helmholtz resonators," The Journal of the Acoustical Society of America, vol. 137, no. 1, pp. 273–280, Jan. 2015.

[25] H. Ryoo and W. Jeon, "Dual-frequency sound-absorbing metasurface based on viscothermal effects with frequency dependence," Journal of Applied Physics, vol. 123, no. 11, p. 115110, Mar. 2018.

[26] P. Soobramaney, G. Flowers, and R. Dean, "Mitigation of the Effects of High Levels of High-Frequency Noise on MEMS Gyroscopes Using Microfibrous Cloth," Volume 4: 20th Design for Manufacturing and the Life Cycle Conference; 9th International Conference on Micro- and Nanosystems, Aug. 2015.

[27] R. N. Dean and G. T. Flowers, "A toolbox approach to reliably integrating MEMS gyroscopes into harsh acoustic and vibration environments," 2013 IEEE Conference on Reliability Science for Advanced Materials and Devices, Feb. 2013.

[28] R. N. Dean, G. T. Flowers, A. S. Hodel, G. Roth, S. Castro, R. Zhou, A. Moreira, A. Ahmed, R. Rifki, B. E. Grantham, D. Bittle, and J. Brunsch, "On the Degradation of

MEMS Gyroscope Performance in the Presence of High Power Acoustic Noise," 2007 IEEE International Symposium on Industrial Electronics, Jun. 2007.

[29] R. Dean, G. Flowers, N. Sanders, R. Horvath, M. Kranz, and M. Whitley, "Micromachined Vibration Isolation Filters to Enhance Packaging for Mechanically Harsh Environments," Journal of Microelectronics and Electronic Packaging, vol. 2, no. 4, pp. 223–231, Oct. 2005.

[30] J. Roberts, M. Motalab, S. Hussain, J. C. Suhling, R. C. Jaeger, and P. Lall, "Measurement of die stresses in microprocessor packaging due to thermal and power cycling," 2012 IEEE 62nd Electronic Components and Technology Conference, May 2012.

[31] Quang Nguyen, J. C. Roberts, J. C. Suhling, and R. C. Jaeger, "Characterization of moisture and thermally induced die stresses in flip chip on laminate assemblies," Fourteenth Intersociety Conference on Thermal and Thermomechanical Phenomena in Electronic Systems (ITherm), May 2014.

[32] J. Roberts, S. Hussain, M. K. Rahim, M. Motalab, J. C. Suhling, R. C. Jaeger, P. Lall, and R. Zhang, "Characterization of microprocessor chip stress distributions during component packaging and thermal cycling," 2010 Proceedings 60th Electronic Components and Technology Conference (ECTC), 2010.

[33] S. A. Cummer and D. Schurig, "One path to acoustic cloaking," New Journal of Physics, vol. 9, no. 3, pp. 45–45, Mar. 2007.

[34] S. Zhang, C. Xia, and N. Fang, "Broadband Acoustic Cloak for Ultrasound Waves," Physical Review Letters, vol. 106, no. 2, Jan. 2011.

[35] J. Li, L. Fok, X. Yin, G. Bartal, and X. Zhang, "Experimental demonstration of an acoustic magnifying hyperlens," Nature Materials, vol. 8, no. 12, pp. 931–934, Oct. 2009.

[36] R. Al Jahdali and Y. Wu, "High transmission acoustic focusing by impedance-matched acoustic meta-surfaces," Applied Physics Letters, vol. 108, no. 3, p. 031902, Jan. 2016.

[37] Y. Tian, Q. Wei, Y. Cheng, and X. Liu, "Acoustic holography based on composite metasurface with decoupled modulation of phase and amplitude," Applied Physics Letters, vol. 110, no. 19, p. 191901, May 2017.

[38] J. Li, C. Shen, A. Díaz-Rubio, S. A. Tretyakov, and S. A. Cummer, "Systematic design and experimental demonstration of bianisotropic metasurfaces for scattering-free manipulation of acoustic wavefronts," Nature Communications, vol. 9, no. 1, Apr. 2018.

[39] Y. Ding, E. C. Statharas, K. Yao, and M. Hong, "A broadband acoustic metamaterial with impedance matching layer of gradient index," Applied Physics Letters, vol. 110, no. 24, p. 241903, Jun. 2017.

[40] H. Ahmed, R. Ahmed, M. M. Indaleeb, and S. Banerjee, "Multifunction acoustic modulation by a multi-mode acoustic metamaterial architecture," Journal of Physics Communications, vol. 2, no. 11, p. 115001, Nov. 2018.

[41] M. Moleron, M. Serra-Garcia, and C. Daraio, "Acoustic Fresnel lenses with extraordinary transmission," Applied Physics Letters, vol. 105, no. 11, p. 114109, Sep. 2014.

[42] J.-P. Xia and H.-X. Sun, "Acoustic focusing by metal circular ring structure," Applied Physics Letters, vol. 106, no. 6, p. 063505, Feb. 2015.

[43] Y. Li, B. Liang, X. Tao, X. Zhu, X. Zou, and J. Cheng, "Acoustic focusing by coiling up space," Applied Physics Letters, vol. 101, no. 23, p. 233508, Dec. 2012.

[44] X. Xia, F. Cai, F. Li, L. Meng, T. Ma, H. Zhou, M. Ke, C. Qiu, Z. Liu, and H. Zheng, "Planar Ultrasonic Lenses Formed by Concentric Circular Sandwiched-Ring Arrays," Advanced Materials Technologies, p. 1800542, Dec. 2018.

[45] S. Qi, Y. Li, and B. Assouar, "Acoustic Focusing and Energy Confinement Based on Multilateral Metasurfaces," Physical Review Applied, vol. 7, no. 5, May 2017.

[46] X. Zhu, K. Li, P. Zhang, J. Zhu, J. Zhang, C. Tian, and S. Liu, "Implementation of dispersion-free slow acoustic wave propagation and phase engineering with helical-structured metamaterials," Nature Communications, vol. 7, no. 1, May 2016.

[47] Y. Li, B. Liang, X. Zou, and J. Cheng, "Extraordinary acoustic transmission through ultrathin acoustic metamaterials by coiling up space," Applied Physics Letters, vol. 103, no. 6, p. 063509, Aug. 2013.

[48] R. Ghaffarivardavagh, J. Nikolajczyk, R. Glynn Holt, S. Anderson, and X. Zhang, "Horn-like space-coiling metamaterials toward simultaneous phase and amplitude modulation," Nature Communications, vol. 9, no. 1, Apr. 2018.

[49] P. Soobramaney, G. Flowers, and R. Dean, "Mitigation of the Effects of High Levels of High-Frequency Noise on MEMS Gyroscopes Using Microfibrous Cloth," Volume 4: 20th Design for Manufacturing and the Life Cycle Conference; 9th International Conference on Micro- and Nanosystems, Aug. 2015.

[50] A. Selamet, Z. L. Ji, and P. M. Radavich, "Acoustic Attenuation Performance of Circular Expansion Chambers with Offset Inlet/outlet: II. Comparison with Experimental and Computational Studies," Journal of Sound and Vibration, vol. 213, no. 4, pp. 619–641, Jun. 1998.

[51] A. Selamet and Z. L. Ji, "Acoustic Attenuation Performance of Circular Expansion Chambers with Offset Inlet/outlet," Journal of Sound and Vibration, vol. 223, no. 2, pp. 197–212, Jun. 1999.

[52] A. Selamet, F. D. Denia, and A. J. Besa, "Acoustic behavior of circular dual-chamber mufflers," Journal of Sound and Vibration, vol. 265, no. 5, pp. 967–985, Aug. 2003.

[53] S. N. Y. Gerges, R. Jordan, F. A. Thieme, J. L. Bento Coelho, and J. P. Arenas, "Muffler modeling by transfer matrix method and experimental verification," Journal of the Brazilian Society of Mechanical Sciences and Engineering, vol. 27, no. 2, Jun. 2005.

[54] M. L. Munjal, "A simple numerical method for three-dimensional analysis of simple expansion chamber mufflers of rectangular as well as circular cross-section with a stationary medium," Journal of Sound and Vibration, vol. 116, no. 1, pp. 71–88, Jul. 1987.

[55] J. LI, K. ISHIHARA, and S. ZHAO, “1209 Transmission Loss Prediction of Perforated Panel Muffler by Boundary Element Analysis,” The Proceedings of Conference of Chugoku-Shikoku Branch, vol. 2012.50, no. 0, pp. 120901–120902, 2012.

[56] D. S. Antao and B. Farouk, “High amplitude nonlinear acoustic wave driven flow fields in cylindrical and conical resonators,” The Journal of the Acoustical Society of America, vol. 134, no. 2, pp. 917–932, Aug. 2013.

[57] J. Friend and L. Y. Yeo, “Microscale acoustofluidics: Microfluidics driven via acoustics and ultrasonics,” Reviews of Modern Physics, vol. 83, no. 2, pp. 647–704, Jun. 2011.

[58] J. T. Karlsen and H. Bruus, “Forces acting on a small particle in an acoustical field in a thermoviscous fluid,” Physical Review E, vol. 92, no. 4, Oct. 2015.

[59] Lord Rayleigh and N. H. Nachtrieb, “The Theory of Sound,” Physics Today, vol. 10, no. 1, pp. 32–34, Jan. 1957.

[60] M. L. Munjal, “Velocity ratio-cum-transfer matrix method for the evaluation of a muffler with mean flow,” Journal of Sound and Vibration, vol. 39, no. 1, pp. 105–119, Mar. 1975.

[61] A. Bejan, “Convection Heat Transfer,” Apr. 2013.

[62] Z. Liu, “Locally Resonant Sonic Materials,” Science, vol. 289, no. 5485, pp. 1734–1736, Sep. 2000.

[63] Y. Jing, J. Xu, and N. X. Fang, “Numerical study of a near-zero-index acoustic metamaterial,” Physics Letters A, vol. 376, no. 45, pp. 2834–2837, Oct. 2012.

[64] M. Badreddine Assouar, M. Senesi, M. Oudich, M. Ruzzene, and Z. Hou, “Broadband plate-type acoustic metamaterial for low-frequency sound attenuation,” Applied Physics Letters, vol. 101, no. 17, p. 173505, Oct. 2012.

[65] H.-C. Zeng, C.-R. Luo, H.-J. Chen, S.-L. Zhai, C.-L. Ding, and X.-P. Zhao, “Flute-model acoustic metamaterials with simultaneously negative bulk modulus and mass density,” Solid State Communications, vol. 173, pp. 14–18, Nov. 2013.

[66] J. M. Manimala and C. T. Sun, "Microstructural design studies for locally dissipative acoustic metamaterials," Journal of Applied Physics, vol. 115, no. 2, p. 023518, Jan. 2014.

[67] Y. Cheng, C. Zhou, B. G. Yuan, D. J. Wu, Q. Wei, and X. J. Liu, "Ultra-sparse metasurface for high reflection of low-frequency sound based on artificial Mie resonances," Nature Materials, vol. 14, no. 10, pp. 1013–1019, Aug. 2015.

[68] Y. Y. Chen, G. L. Huang, and C. T. Sun, "Band Gap Control in an Active Elastic Metamaterial With Negative Capacitance Piezoelectric Shunting," Journal of Vibration and Acoustics, vol. 136, no. 6, p. 061008, Sep. 2014.

[69] M. A. Nouh, O. J. Aldraihem, and A. Baz, "Periodic metamaterial plates with smart tunable local resonators," Journal of Intelligent Material Systems and Structures, vol. 27, no. 13, pp. 1829–1845, Jul. 2016.

[70] J. Cheer, S. Daley, and C. McCormick, "Feedforward control of sound transmission using an active acoustic metamaterial," Smart Materials and Structures, vol. 26, no. 2, p. 025032, Jan. 2017.

[71] M. Reynolds and S. Daley, "An active viscoelastic metamaterial for isolation applications," Smart Materials and Structures, vol. 23, no. 4, p. 045030, Mar. 2014.

[72] Y. Liao, Y. Chen, G. Huang, and X. Zhou, "Broadband low-frequency sound isolation by lightweight adaptive metamaterials," Journal of Applied Physics, vol. 123, no. 9, p. 091705, Mar. 2018.

[73] F. B. Daniels, "On the Propagation of Sound Waves in a Cylindrical Conduit," The Journal of the Acoustical Society of America, vol. 22, no. 5, pp. 563–564, Sep. 1950.

[74] B. Bauer, "Correction to 'Equivalent circuit analysis of mechano-acoustic structures,'" Transactions of the IRE Professional Group on Audio, vol. AU-3, no. 1, pp. 4–4, Jan. 1955.

[75] S. C. Thompson, T. B. Gabrielson, and D. M. Warren, “A thermoviscous tube propagation model suitable for time domain analysis,” 2013.

[76] J. Jeong and R. Nevels, “Time-Domain Analysis of a Lossy Nonuniform Transmission Line,” IEEE Transactions on Circuits and Systems II: Express Briefs, vol. 56, no. 2, pp. 157–161, Feb. 2009.

[77] S. C. Thompson, T. B. Gabrielson, and D. M. Warren, “Analog model for thermoviscous propagation in a cylindrical tube,” The Journal of the Acoustical Society of America, vol. 135, no. 2, pp. 585–590, Feb. 2014.

[78] S. Bilbao and R. Harrison, “Passive time-domain numerical models of viscothermal wave propagation in acoustic tubes of variable cross section,” The Journal of the Acoustical Society of America, vol. 140, no. 1, pp. 728–740, Jul. 2016.

[79] A. Liu, X. Zhou, G. Huang, and G. Hu, “Super-resolution imaging by resonant tunneling in anisotropic acoustic metamaterials,” The Journal of the Acoustical Society of America, vol. 132, no. 4, pp. 2800–2806, Oct. 2012.

[80] V. Fokin, M. Ambati, C. Sun, and X. Zhang, “Method for retrieving effective properties of locally resonant acoustic metamaterials,” Physical Review B, vol. 76, no. 14, Oct. 2007.

[81] Y. Xiao, B. R. Mace, J. Wen, and X. Wen, “Formation and coupling of band gaps in a locally resonant elastic system comprising a string with attached resonators,” Physics Letters A, vol. 375, no. 12, pp. 1485–1491, Mar. 2011.

[82] A. Liu, X. Zhou, G. Huang, and G. Hu, “Super-resolution imaging by resonant tunneling in anisotropic acoustic metamaterials,” The Journal of the Acoustical Society of America, vol. 132, no. 4, pp. 2800–2806, Oct. 2012.

[83] W.-S. Gan, J. Yang, and T. Kamakura, “A review of parametric acoustic array in air,” Applied Acoustics, vol. 73, no. 12, pp. 1211–1219, Dec. 2012.

[84] H. Nomura, C. M. Hedberg, and T. Kamakura, “Numerical simulation of length-limited parametric sound beam,” 2012.

[85] O. Guasch and P. Sánchez-Martín, "Far-field directivity of parametric loudspeaker arrays set on curved surfaces," Applied Mathematical Modelling, vol. 60, pp. 721–738, Aug. 2018.

[86] M. Moleron, M. Serra-Garcia, and C. Daraio, "Visco-thermal effects in acoustic metamaterials: from total transmission to total reflection and high absorption," New Journal of Physics, vol. 18, no. 3, p. 033003, Mar. 2016.

[87] Y. Li, B. Liang, Z. Gu, X. Zou, and J. Cheng, "Reflected wavefront manipulation based on ultrathin planar acoustic metasurfaces," Scientific Reports, vol. 3, no. 1, Aug. 2013.

[88] G. Memoli, M. Caleap, M. Asakawa, D. R. Sahoo, B. W. Drinkwater, and S. Subramanian, "Metamaterial bricks and quantization of meta-surfaces," Nature Communications, vol. 8, no. 1, Feb. 2017.

[89] B. Liu, J. Zhao, X. Xu, W. Zhao, and Y. Jiang, "All-angle Negative Reflection with An Ultrathin Acoustic Gradient Metasurface: Floquet-Bloch Modes Perspective and Experimental Verification," Scientific Reports, vol. 7, no. 1, Oct. 2017.

[90] Y. Fu, J. Li, Y. Xie, C. Shen, Y. Xu, H. Chen, and S. A. Cummer, "Compact acoustic retroreflector based on a mirrored Luneburg lens," Physical Review Materials, vol. 2, no. 10, Oct. 2018.

[91] Z. Liang and J. Li, "Extreme Acoustic Metamaterial by Coiling Up Space," Physical Review Letters, vol. 108, no. 11, Mar. 2012.

[92] J. Chen, J. Xiao, D. Lisevych, A. Shakouri, and Z. Fan, "Deep-subwavelength control of acoustic waves in an ultra-compact metasurface lens," Nature Communications, vol. 9, no. 1, Nov. 2018.

[93] P. Wei, F. Liu, Z. Liang, Y. Xu, S. T. Chu, and J. Li, "An acoustic beam shifter with enhanced transmission using perforated metamaterials," EPL (Europhysics Letters), vol. 109, no. 1, p. 14004, Jan. 2015.

[94] C. Rubio, J. Fuster, S. Castiñeira-Ibáñez, A. Uris, F. Belmar, and P. Candelas, "Pinhole Zone Plate Lens for Ultrasound Focusing," Sensors, vol. 17, no. 7, p. 1690, Jul. 2017.

[95] X. Chen, Z. Diao, S. He, G. Zheng, and Q. Yu, "Amplification Characteristics of Fresnel Zone Plate Acoustic Lens," STEM Fellowship Journal, vol. 3, no. 1, pp. 15–22, Feb. 2017.

[96] D. C. Calvo, A. L. Thangawng, M. Nicholas, and C. N. Layman, "Thin Fresnel zone plate lenses for focusing underwater sound," Applied Physics Letters, vol. 107, no. 1, p. 014103, Jul. 2015.

[97] H. Nomura, C. M. Hedberg, and T. Kamakura, "Numerical simulation of parametric sound generation and its application to length-limited sound beam," Applied Acoustics, vol. 73, no. 12, pp. 1231–1238, Dec. 2012.

[98] E. Skinner, M. Groves, and M. K. Hinders, "Demonstration of a length limited parametric array," Applied Acoustics, vol. 148, pp. 423–433, May 2019.

[99] L. Liu, X. Zhang, M. Kenney, X. Su, N. Xu, C. Ouyang, Y. Shi, J. Han, W. Zhang, and S. Zhang, "Broadband Metasurfaces with Simultaneous Control of Phase and Amplitude," Advanced Materials, vol. 26, no. 29, pp. 5031–5036, May 2014.

[100] Y. Zhou, M.-H. Lu, L. Feng, X. Ni, Y.-F. Chen, Y.-Y. Zhu, S.-N. Zhu, and N.-B. Ming, "Acoustic Surface Evanescent Wave and its Dominant Contribution to Extraordinary Acoustic Transmission and Collimation of Sound," Physical Review Letters, vol. 104, no. 16, Apr. 2010.

Appendices

Appendix A

Derivation of Items of Transfer Matrix $[M]$

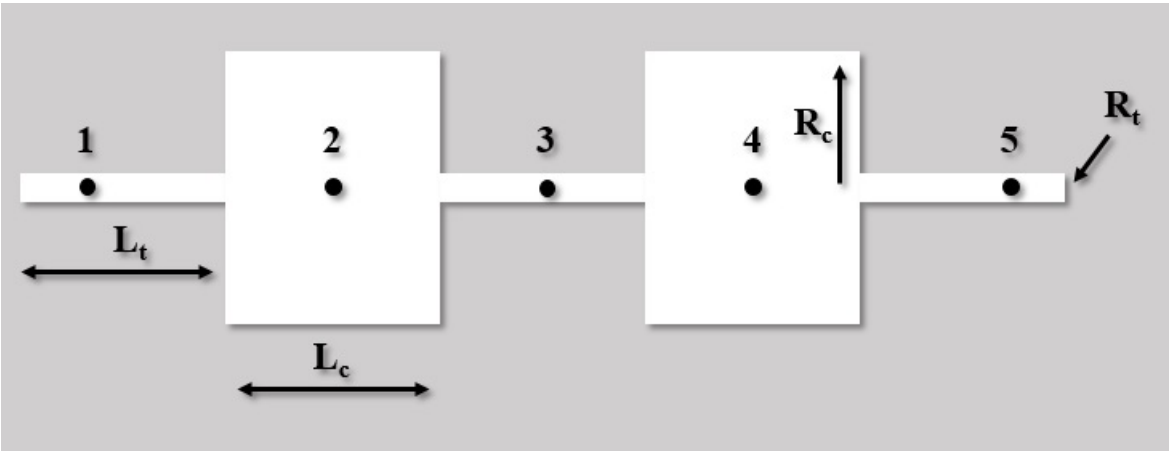

Figure A.1: Schemetic of ODEC with labled sections.

This section demonstrates the detailed deriviation of transfer items T_{mn} of $[M]$ that are listed in Eq. 2.6. Tubes 1, 3, and 5 share the same length $L_{t1} = L_{t3} = L_{t5} = L_t$, and as well as the chamber length $L_{c2} = L_{c4} = L_c$. With the tube end correction inside the ODEC, the equivalent tube length can be express as $\widetilde{L}_{t1} = \widetilde{L}_{t3} = \widetilde{L}_{t5} = L_t + 2\Delta L_t = L_t + \frac{16R_t}{3\pi}$.

The impedance of tubes and chambers are listed below respectively:

$$Y_t = \frac{p_i}{v_i} = \pm\frac{v_i}{\pi R_t^2}[1 - \frac{1}{R_t}(\frac{\mu_e}{2\rho\omega})^{\frac{1}{2}} + \frac{j}{R_t}(\frac{\mu_e}{2\rho\omega})^{\frac{1}{2}}] \tag{A.1}$$

$$Y_c = \frac{p_i}{v_i} = \pm\frac{v_i}{\pi R_c^2}[1 - \frac{1}{R_c}(\frac{\mu_e}{2\rho\omega})^{\frac{1}{2}} + \frac{j}{R_c}(\frac{\mu_e}{2\rho\omega})^{\frac{1}{2}}] \tag{A.2}$$

With the convenience for calculation, we make the abbreviations as follows:

$$\sin(k\widetilde{L}_{t1}) = \sin(k\widetilde{L}_{t3}) = \sin(k\widetilde{L}_{t5}) = \sin[\frac{2\pi f}{c}(L_t + \frac{8R_t}{3\pi})] = S_t \tag{A.3}$$

$$\cos(k\widetilde{L}_{t1}) = \cos(k\widetilde{L}_{t3}) = \cos(k\widetilde{L}_{t5}) = \cos[\frac{2\pi f}{c}(L_t + \frac{8R_t}{3\pi})] = C_t \tag{A.4}$$

$$\sin(k\widetilde{L}_{c1}) = \sin(k\widetilde{L}_{c3}) = \sin(k\widetilde{L}_{c5}) = \sin[\frac{2\pi f}{c}(L_c + \frac{8R_c}{3\pi})] = S_c \tag{A.5}$$

$$\cos(k\widetilde{L}_{c1}) = \cos(k\widetilde{L}_{c3}) = \cos(k\widetilde{L}_{c5}) = \cos[\frac{2\pi f}{c}(L_c + \frac{8R_c}{3\pi})] = C_c \tag{A.6}$$

where $c = 343$ m/s is the sound speed, and f is the frequency. Thus,

$$T_{11} = C_t^3(C_c^2 - S_c^2) + (\frac{Y_c}{Y_t} + \frac{Y_t}{Y_c})S_t^3 S_c C_c + (1 + \frac{Y_t^2}{Y_c^2} + \frac{Y_c^2}{Y_t^2})S_t^2 S_c^2 C_t - 3S_t^2 C_c^2 C_t - 3(\frac{Y_c}{Y_t} + \frac{Y_t}{Y_c})C_t^2 S_t S_c C_c \tag{A.7}$$

$$T_{12} = j[(\frac{Y_t^3}{Y_c^2}S_c^2 - Y_t C_c^2)S_t^3 + 2Y_c C_t^3 C_c S_C + 3Y_t C_t^2 C_c^2 S_t - (2Y_t + \frac{Y_c^2}{Y_t})C_t^2 S_c^2 S_t - (2Y_c + 4\frac{Y_t^2}{Y_c})S_t^2 S_c C_c C_t] \tag{A.8}$$

$$T_{21} = j[(\frac{Y_c^2}{Y_t^3}S_c^2 - \frac{1}{Y_t}C_c^2)S_t^3 + \frac{2}{Y_c}C_t^3 C_c S_C + \frac{3}{Y_t}C_t^2 C_c^2 S_t - (\frac{2}{Y_t} + \frac{Y_t}{Y_c^2})C_t^2 S_c^2 S_t - (\frac{2}{Y_c} + 4\frac{Y_c}{Y_t^2})S_t^2 S_c C_c C_t] \tag{A.9}$$

$$T_{22} = C_t^3(C_c^2 - S_c^2) + (\frac{Y_c}{Y_t} + \frac{Y_t}{Y_c})S_t^3 S_c C_c + (1 + \frac{Y_t^2}{Y_c^2} + \frac{Y_c^2}{Y_t^2})S_t^2 S_c^2 C_t - 3S_t^2 C_c^2 C_t - 3(\frac{Y_c}{Y_t} + \frac{Y_t}{Y_c})C_t^2 S_t S_c C_c \tag{A.10}$$

Appendix B

The Pseudocode for Calculating the Analytical Transfer Matrix, $[M]$, and Transmission Loss

```
clear all
close all

syms lt lc rt rc f rho rho0 vk u ue Pr a real

%rho0 = density of air @ STP 20C sea level

a = 340.29; % the sound speed [m/s]
w = 2*pi*f; % angular frequency [rad/s]
k = w/a; % the wave number

ldt = 8*rt/(3*pi);

Ct = cos(k*(lt+ldt)); % assuming the end is flanged-end
   tube case
St = sin(k*(lt+ldt));

Ctm = cos(k*(lt+2*ldt));
Stm = sin(k*(lt+2*ldt));

Cc = cos(k*lc);
Sc = sin(k*lc);


%% Characteristic impedance Y

u = vk*rho;
ue = u*(1+(1.4^0.5-1.4^(-0.5))*Pr)^2;
Yt = -(a/(pi*rt^2))*(1-(1/rt)*(0.5*ue/(rho0*w))^0.5+1i
   *((1/rt)*(0.5*ue/(rho0*w))^0.5));
Yc = -(a/(pi*rc^2))*(1-(1/rc)*(0.5*ue/(rho0*w))^0.5+1i
   *((1/rc)*(0.5*ue/(rho0*w))^0.5));
```

```
30
31 % Four-pole matrix
32
33 % Tube matrix:
34 M9 = [Ct 1i*Yt*St; 1i*St/Yt Ct];
35 M5 = [Ct 1i*Yt*Stm; 1i*Stm/Yt Ctm];
36 M1 = [Ct 1i*Yt*St; 1i*St/Yt Ct];
37
38 % Chamber matrix:
39 M7 = [Cc 1i*Yc*Sc; 1i*Sc/Yc Cc];
40 M3 = [Cc 1i*Yc*Sc; 1i*Sc/Yc Cc];
41
42 % Connection matrix:
43 M8=eye(2);
44 M6=eye(2);
45 M4=eye(2);
46 M2=eye(2);
47
48 T = M9*M8*M7*M6*M5*M4*M3*M2;
49 T11 = T(1,1);
50 T12 = T(1,2);
51 T21 = T(2,1);
52 T22 = T(2,2);
53
54 P = Yt/Yt*abs((T11+T12/Yt+T21*Yt+Yt/Yt*T22)/2);
55
56 %[f1] = f_low:f_incr:f_high;
57 % data = { lt, lc, rt, rc, vk, rho, rho0, Pr};
58 % datn = { TubeLength, ChamberLength, TubeRadius,
      ChamberLength, Density, ReferenceDensity, PrandtlNumber
      }; % insert parameters
59 % PP = subs(P, data, datn);
60 % PP_final = subs(PP, f, f1);
61
62 [TL] = 20*log10(PP_final); % transmission loss
```

Appendix C

The Pseudocode for Calculating Reflection, Transmission, Absorption, Effective Density, Effective Modulus, Effective Impedance, and Refractive Index

```
% This is the script to load SPL data from text files

clear all;
close all;
format long

prompt1 = 'Enter file name of Microphone 1: ';
prompt2 = 'Enter file name of Microphone 2: ';
prompt3 = 'Enter file name of Microphone 3: ';
prompt4 = 'Enter file name of Microphone 4: ';

fileName1 = input(prompt1,'s');
fileName2 = input(prompt2,'s');
fileName3 = input(prompt3,'s');
fileName4 = input(prompt4,'s');

FileName1 = [fileName1,'.txt'];
FileName2 = [fileName2,'.txt'];
FileName3 = [fileName3,'.txt'];
FileName4 = [fileName4,'.txt'];

X1 = load(FileName1);
X2 = load(FileName2);
TransIn = load(FileName3);
TransOut = load(FileName4);

X1fq = X1(:,1);
X1spl = X1(:,2);
X1pha = X1(:,3);
X2fq = X2(:,1);
X2spl = X2(:,2);
```

```
X2pha = X2(:,3);

Transfq = TransIn(:,1);
TransInspl = TransIn(:,2);
TransIna = TransIn(:,3);

TransOutfq = TransIn(:,1);
TransOutspl = TransOut(:,2);
TransOuta = TransOut(:,3);
% TransOutspl1 = [TransOutspl TransOuta];


%% Reflection coefficient

zero1 = 0;
X1p = 20e-6.*exp(X1spl./20); % SPL to Pressure
X2p = 20e-6.*exp(X2spl./20);
H21 = X2p./X1p;
k = X1fq*2*pi/343;   % wavenumber k=w/c=f*2pi/c
rho0 = 1.204;     % kg/m^3 @ 20 degree C
x1 = 0.0091+0.000975; % position of Mic1 [m]
x2 = 0.0091;      % position of Mic2 [m]
s = x1-x2;        % distance between Mics [m]

r = 0.5*exp(2.*k.*x1.*1i).*(H21-exp(-k.*s.*1i))./(exp(k.*s
   .*1i)-H21); % Reflectivity
r_real = real(r);
r_abs = abs(r_real);
r_img = imag(r);


%% Transmission coefficient

TransInp = 20e-6.*exp(TransInspl./20); % SPL to Pressure
TransOutp = 20e-6.*exp(TransOutspl./20);
t = (TransOutp./TransInp).^2;       % Transmission
   coefficient: Power out/ Power in
t_a = TransOuta./TransIna;          %Transmission phase


%% Absorption coefficient

a = (1-r_abs.^2-t.^2);


%% Impedance, refractive index
```

```
76
77 c = 340.29;                                    % speed of sound
       m/s
78 d = 0.005;                                    % The sample
     thickness [m]
79 numerator = ((r.^2-t.^2-1).^2-4*t.^2).^0.5;
80 parameter = (1-r.^2+t.^2+numerator)./(2*t);
81
82 % Impedance:
83 Zeff = numerator./(1-2.*r+r.^2-t.^2);
84
85 N = -1i.*log10(parameter)./(d*k);
86
87 if abs(min(real(N)))>max(real(N)) % Normalize to [-1 1]
88    maxvalue1 = abs(min(real(N)));
89    minvalue1 = min(real(N));
90 else
91    maxvalue1 = max(real(N));
92    minvalue1 = -max(real(N));
93 end
94
95 % Refractive Index real part:
96 Nnr = 2.*real(N)./(maxvalue1-minvalue1);
97
98 if abs(min(imag(N)))>max(imag(N))
99    maxvalue2 = abs(min(imag(N)));
100   minvalue2 = min(imag(N));
101 else
102   maxvalue2 = max(imag(N));
103   minvalue2 = -max(imag(N));
104 end
105
106 % Refractive Index imaginary part:
107 Nni = 2.*imag(N)./(maxvalue2-minvalue2);
108
109 % Effective Density:
110 rho_eff0 = N.*Zeff;
111 if abs(min(rho_eff0))>max(rho_eff0) % Normalize to [-1 1]
112    maxvalue3 = abs(min(rho_eff0));
113    minvalue3 = min(rho_eff0);
114 else
115    maxvalue3 = max(rho_eff0);
116    minvalue3 = -max(rho_eff0);
117 end
118
119 rho_eff0n = 2.*real(rho_eff0)./(maxvalue3-minvalue3);
```

```
120
121 if abs(min(imag(rho_eff0)))>max(imag(rho_eff0))
122     maxvalue4 = abs(min(imag(rho_eff0)));
123     minvalue4 = min(imag(rho_eff0));
124  else
125     maxvalue4 = max(imag(rho_eff0));
126     minvalue4 = -max(imag(rho_eff0));
127  end
128
129 rho_eff0ni = 2.*imag(rho_eff0)./(maxvalue4-minvalue4);
130
131 % Effective Modulus:
132 modulus_eff0 = -Zeff./N;
```

Appendix D

The Pseudocode for Real-time Sound Generation by Speaker and Data Acquisition by Microphones

```
% This is the script to send and receive sound signal at
   the same time in time domain

close all
clear all

%% Sounding Method 1:

% Device setup:
   devInfo = audiodevinfo; %getting audio device status
      connected with the computer system
   n = size(devInfo.input,2); %getting especially the
      input device status
       %size(A,n): n==1 returns the dimension of row, n==2
          returns the dimension of column
   disp('Details␣Of␣Audio␣Recording␣device␣Connected:');

   for i = 0:n-1
      disp('Device␣Name:')
      disp(devInfo.input(1,i+1).Name) %display the audio
         input device name
      disp('Device␣id:')
      disp(i) %diaplay the device id
   end


%% Input/Output info

   devID1 = input('Enter␣the␣1st␣Mic␣ID␣from␣the␣above␣
      Device␣List␣to␣Start␣Recording:');
                                       %getting the device id
                                          for recording
```

```
26
27
28      devID2 = input('Enter the 2nd Mic ID, and press Enter
            if there is none:');
29
30      time = input('Enter the Duration of Recording(s):');
31                                          %getting the duration
                                              of recording


32      bit = input('Enter Bit Depth of Recording(e.g. 8bit):')
            ;                                          %getting the
            bit depth of recording
33      sampleFq = 40000;
34
35      amp = input('Enter the Uniform Amplitude of Swept-Sine
            (e.g. 1 or bigger):');
36
37  frq = [];
38  T = 1;
39  for i = 1:7;
40      tX = tXstart:1/Fs:tXstart+i;
41      f = frq(i);
42      SineZ{i} = sin(2*pi*f*tX);
43      soundsc(SineZ{i}, Fs);
44      pause(1);
45  end
46
47          SineZ_p = cell2mat(SineZ); % Concatenate Vectors
48
49          t_p = linspace(0, length(SineZ_p), length(SineZ_p));
                % Create Matching Time Vector
50
51  sound(SineZ_p, Fs)
52
53
54  %% Sounding Method 2:
55
56  tic
57
58  fs = 40000;
59  amp = 1;
60  freqs = 100:1:10000;
61  T = 1/fs;
62  dur = 0.1;
63  phi = 0;
```

```
l = length([0:T:dur-T]);
L = 0.05*l;

fade_in = linspace(0,1,L);
fade_out = linspace(1,0,L);

x1 = zeros(1,200);
x2 = zeros(1,3600);
x3 = zeros(1,200);
x = zeros(1,4000);
y = [];

for k = 1:size(freqs,2)
   x1 = fade_in.*amp.*sin(2*pi*freqs(k).*[0:T:L*T-T]+phi);
   x2 = amp*sin(2*pi*freqs(k)*[L*T:T:dur-L*T-T]+phi);
   x3 = fade_out.*amp.*sin(2*pi*freqs(k).*[dur-L*T:T:dur-T
      ]+phi);
   x = [x1,x2,x3];
   y = horzcat(y,x);
end

soundsc(y,fs)

toc

%%

Time = ; % time length for recording

aud1 = audiorecorder(sampleFq,bit,1,devID1);
recordblocking(aud1,Time);

myRecording1 = getaudiodata(aud1); %start audio recoding
   in time domain, the magnitude in double type, between
   -1 and 1.

SoundPressure1 = myRecording1*63.69*0.6;
%Converted sound pressure in [Pa] , see instructions of
   Microphone, Daq Device, Amplifier and Signal Generator.
```

Appendix E

The Pseudocode for Converting Time-domain Data to Frequency-domain Data

```
close all;
clear all;

Fs = ; % Sampling frequency
T_increament = 1/Fs; % Time increament
T_measure = ; % Time of measurement
L = T_measure/T_increament; % Length of the signal vector
time = 0:T_increament:T_measure; % Time vector

f1 = ; % Lower fq
f2 = ; % Upper fq

F = linspace(f1,f2,L);

phi = 2*pi*cumsum(F)/Fs;

y = sin(phi);

subplot(2,1,2)
plot(time(1:length(time)-1),y(:))
sound(y,Fs)


%% FFT

signal_fft = fft(y2,L)/L;

amplitude = 2*abs(signal_fft(1:L/2+1)); % Take half length
    of the fft results, because the second of half
   represents the negative frequencies.

Freq = Fs/2*linspace(0,1,L/2+1);
```

Appendix F

The Pseudocode for Sound Pressure Mapping Data Processing

```
clear all;
close all;

%% Read measurements, SPL to P, and re-organize the data
   matrices

for L = 31:-1:1 % Folder sequence (R-direction)

   for k = 37:-1:1 % File sequence in each folder (Z-
      direction), inverse to avoid "subscripted assignment
       between dissimilar structures"

      K = 25*(k-1); % Lines in half R-direction without R
         =0

% first half:
      fln1 = strcat('D:\DirectoryName\papers\2018-9\
         Testing\DoubleSide_Testing\BrTest\WoLens\r',
         num2str( 25*(L-1) ), '\r',num2str( 25*(L-1) ),'z'
         , num2str( K ),'.txt');

      nr(k) = importdata(fln1,' '); % Construct the matrix
          to store the data read from text file (Frq, SPL,
          Pha)

% second half:
      fln2 = strcat('D:\DirectoryName\papers\2018-9\
         Testing\DoubleSide_Testing\FullTest\pr', num2str(
          5*L, '%02d' ), 'f\', num2str( k-1, '%02d' ),'.
         txt');

```

```
20        pr(k) = importdata(fln2,'␣'); % Construct the matrix
              to store the data read from text file (Frq, SPL,
              Pha)
21
22  % R=0
23        fln3 = strcat('D:\DirectoryName\papers\2018-9\
              Testing\DoubleSide_Testing\FullTest\pr00f\',
              num2str( k-1, '%02d' ),'.txt');
24        pr0(k) = importdata(fln3,'␣');
25
26    end
27
28    for m = 37:-1:1
29
30        nrp = nr(m).data(:,2); % The SPL at each position
              for all frequencies
31        nrp = 20e-6.*exp(nrp./20); % SPL(dB) to Pressure(Pa)
32        nrP(:,m) = nrp; % Store the pressure in a new matrix
              (Frequency,Position)
33                  % Frq in rows, Z-Pos in columns
34
35        prp = pr(5*(m-1)+1).data(:,2); % The SPL at each
              position for all frequencies
36        prp = 20e-6.*exp(prp./20); % SPL(dB) to Pressure(Pa)
37        prP(:,m) = prp; % Store the pressure in a new matrix
              (Frequency,Position)
38
39        pr0p = pr0(5*(m-1)+1).data(:,2); % The SPL at each
              position for all frequencies
40        pr0p = 20e-6.*exp(pr0p./20); % SPL(dB) to Pressure(
              Pa)
41        pr0P(:,m) = pr0p; % Store the pressure in a new
              matrix (Frequency,Position)
42
43    end
44
45    f = nr(1).data(:,1); % Frequency of measurement
46    Len = length(f); % Length of the frequency array (how
          many frequencies)
47
48    for n = Len:-3:1 % Send the Z-pressure value of each
          Frq to respective matrix.
49
50        M{n}.data(:,L) = nrP(n,:)';    % R35 -> R05
51        O{n}.data = pr0P(n,:)';        % R00
52        N{n}.data(:,L) = prP(n,:)';  % R05 -> R35
```

```
53
54      end
55
56  end
57
58
59  %% Write to txt files
60
61  for a = Len:-3:1
62      PP{a}.data = [M1{a}.data];
63      exfln = strcat('D:\DirectoryName\papers\2019-1\
            SineChannelLens\WLens\Prs_Fq\',num2str(f(a)),'.txt')
            ;
64      dlmwrite(exfln, PP{a}.data,'precision','%.6f','
            delimiter','␣', 'newline', 'pc');
65
66  end
```

Appendix G

The Pseudocode for Sound Phase Mapping Data Processing

```
clear all;
close all;

%% Read measurements of phase, and re-organize the data
   matrices

for L = 31:-1:1 % Folder sequence (R-direction)

   for k = 37:-1:1 % File sequence in each folder (Z-
      direction), inverse to avoid "subscripted assignment
       between dissimilar structures"

      K = 25*(k-1);

      fln1 = strcat('D:\DirectoryName\papers\2019-1\
         SineChannelLens\WLens\r', num2str( 25*(L-1) ), '\
         r',num2str( 25*(L-1) ),'z', num2str( K ),'.txt');

      nr(k) = importdata(fln1,'␣'); % Construct the matrix
          to store the data read from text file (Frq, SPL,
          Pha)

      fln2 = strcat('D:\DirectoryName\papers\2018-9\
         Testing\DoubleSide_Testing\FullTest\pr', num2str(
          5*L, '%02d' ), 'f\', num2str( k-1, '%02d' ),'.
         txt');

      pr(k) = importdata(fln2,'␣'); % Construct the matrix
          to store the data read from text file (Frq, SPL,
          Pha)

```

```
20        fln3 = strcat('D:\DirectoryName\papers\2018-9\
            Testing\DoubleSide_Testing\FullTest\pr00f\',
            num2str( k-1, '%02d' ),'.txt');
21
22        pr0(k) = importdata(fln3,'␣');
23
24     end
25
26     for m = 37:-1:1
27        nra = nr(m).data(:,3); % The Phase at each position
            for all frequencies
28
29        nrA(:,m) = nra; % Store the Phase in a new matrix (
            Frequency,Position)
30                  % Frq in rows, Z-Pos in columns
31
32        pra = pr(5*(m-1)+1).data(:,3);
33        prA(:,m) = pra; % Store the pressure in a new matrix
              (Frequency,Position)
34
35        pr0a = pr0(5*(m-1)+1).data(:,3);
36        pr0A(:,m) = pr0a;
37
38     end
39
40     f = nr(1).data(:,1); % Frequency of measurement
41     Len = length(f); % Length of the frequency array (how
         many frequencies)
42
43     for n = Len:-3:1 % Send the Z-pressure value of each
         Frq to respective matrix.
44        M{n}.data(:,L) = nrA(n,:)';  % R35 -> R05
45        O{n}.data = pr0A(n,:)';       % R00
46        N{n}.data(:,L) = prA(n,:)';  % R05 -> R35
47
48     end
49
50  end
51
52
53  %% Write to txt files
54
55  for a = Len:-3:1
56
57     AA{a}.data = [M1{a}.data];
```

```
58      exfln = strcat('D:\DirectoryName\papers\2019-1\
          SineChannelLens\WLens\Pha_Fq\',num2str(f(a)),'.txt')
          ;
59      dlmwrite(exfln, AA{a}.data,'precision','%.6f','
          delimiter','␣', 'newline', 'pc');
60
61  end
```